NBP-88-12

Circulation Dynamics in Mt. Hope Bay &

the Lower Taunton River 143 pp

Spaulding, White, Heinmiller, Simoneau, Liang, & Choi (URI)

Narragansett Bay Estuary Program

CIRCULATION DYNAMICS IN MT. HOPE BAY AND THE LOWER TAUNTON RIVER

Malcolm L. Spaulding, Frank M. White,
Paul Heinmiller, Martha Marcy Simoneau,
Shin Jey Liang, and Jei Kook Choi

Department of Ocean Engineering
University of Rhode Island
Kingston, Rhode Island 02881

Sponsored by

University of Rhode Island Sea Grant Program
National Oceanic and Atmospheric Administration
U.S. Department of Commerce

REPORT # NBP-88-12

Narragansett Bay Project
Environmental Protection Agency

July 20, 1988

CIRCULATION DYNAMICS IN MT. HOPE BAY AND THE LOWER TAUNTON RIVER

Malcolm L. Spaulding, Frank M. White,
Paul Heinmiller, Martha Marcy Simoneau,
Shin Jey Liang, and Jei Kook Choi

Department of Ocean Engineering
University of Rhode Island
Kingston, Rhode Island 02881

Sponsored by

University of Rhode Island Sea Grant Program
National Oceanic and Atmospheric Administration
U.S. Department of Commerce

REPORT # NBP-88-12

Narragansett Bay Project
Environmental Protection Agency

July 20, 1988

FOREWORD

The United States Congress created the National Estuary Program in 1984, citing its concern for the "health and ecological integrity" of the nation's estuaries and estuarine resources. Narragansett Bay was selected for inclusion in the National Estuary Program in 1984 and designated an "estuary of national significance" in 1988. The Narragansett Bay Project (NBP) was established in 1985. Under the joint sponsorship of the U.S. Environmental Protection Agency and the Rhode Island Department of Environmental Management, the NBP's mandate is to direct a five-year program of research and planning focussed on managing Narragansett Bay and its resources for future generations. The NBP will develop a comprehensive management plan by December, 1990, which will recommend actions to improve and protect the Bay and its natural resources.

The NBP has established the following seven priority issues for Narragansett Bay:

* management of fisheries
* nutrients and potential for eutrophication
* impacts of toxic contaminants
* health and abundance of living resources
* health risk to consumers of contaminated seafood
* land-based impacts on water quality
* recreational uses

The NBP is taking an ecosystem approach to address these problems and has funded research that will help to improve our understanding of various aspects of these priority problems. The Project is also working to expand and coordinate existing programs among state agencies, governmental institutions, and academic researchers in order to apply research findings to the practical needs of managing the Bay and improving the environmental quality of its watershed.

This report represents the technical results of an investigation performed for the Narragansett Bay Project. The information in this document has been funded wholly or in part by the United States Environmental Protection Agency under assistance agreement #CX812768 to the Rhode Island Department of Environmental Management. It has been subject to the Agency's and the Narragansett Bay Project's peer and administrative review and has been accepted for publication by the Management Committee of the Narragansett Bay Project. The results and conclusions contained herein are those of the author(s), and do not necessarily represent the views or recommendations of the NBP. Final recommendations for management actions will be based upon the results of this and other investigations.

TABLE OF CONTENTS

ABSTRACT

A field study was conducted in Mt. Hope Bay and the lower Taunton River to describe the circulation in response to tide, wind and density induced forcing. Five current meter deployments were made from December 1985 to January 1987 with a typical duration of 60 days. Measurements were made at surface and bottom locations at three stations: Mt. Hope Bridge, Brightman St. Bridge and at the entrance to the Sakonnet River. Time series measurements of currents, conductivity and temperature were made at each of the stations. Tidal elevations were recorded at Mt. Hope Bridge, Steep Brook and Touisset. River flow data were obtained for the Taunton River from USGS and wind speed and direction from NOAA National Weather Station at Green Airport, Warwick, Rhode Island.

Analysis of the field data indicate that the sea surface elevation and currents are dominated by the semi-diurnal tide (80-80% current variance) in an approximate standing wave pattern. Tidal currents are a strong function of location and in narrow passages reach peak values of 25 cm/s, but have more typical maximums of 10 cm/s in the bay proper. Low frequency currents (30 hr filtered) show little wind induced forcing and are dominated by steady flows. For the lower portion of the Taunton River (Brightman St. Bridge) a classical stratified estuarine circulation pattern is observed. For the Sakonnet River and Mt. Hope Bridge sites the flow is consistently out of Mt. Hope Bay. The hydrography shows that the water column is well mixed throughout Mt. Hope Bay. As one approaches the lower end of the Taunton River the water column becomes stratified because of the river discharge of freshwater.

Hydrodynamic model simulations of the river and tidal flow in Mt. Hope Bay were performed using a two dimensional vertically averaged approach. Simulations were made using both finite element and boundary conforming finite difference solution methodologies. Simulations show that the Taunton River freshwater flow exits Mt. Hope Bay through the Mt. Hope Bridge and Sakonnet River transects with a distribution of 68% and 32%, respectively. These are in excellent agreement with earlier estimates. Model simulations of the semi-diurnal tide are generally in reasonable agreement with observations. The standing wave nature of the tide is predicted and the current speeds and directions are shown to be related to the geometry and bathymetry of the region. Model predictions are insensitive to bottom friction in agreement with standing wave theory.

LIST OF TABLES

LIST OF FIGURES

1. INTRODUCTION

Pollution in Mt. Hope Bay and the Taunton River (Figure 1.1) has long been recognized as a serious interstate water quality problem concerning both Massachusetts and Rhode Island. Seven municipal waste water treatment plants discharge into the Mr. Hope Bay watershed. All are located in Massachusetts. Two of the largest sources, Fall River and Taunton, have historically provided only primary treatment. The Fall River plant only recently (May 1984) went to secondary treatment. The Fall River treatment plant discharges 14.9 million gallons per day (MGD) directly to Mt. Hope Bay while the Taunton plant discharges 6.5 MGD. The other treatment facilities contribute less than 1 MGD each with the exception of the Brockton treatment facility (7.5 MGD) located on the Salisbury Plant River in the upper reaches of the watershed. The area receives additional pollutants from a series of pockets of industrial activity including tanning, textile and leather manufacturing, metal plating, and manufacturing of chemicals. Four municipalities in the watershed have combined sewer over flows. During periods of rainfall the sewers become overloaded discharging quantities of stormwater and untreated domestic and industrial waste water directly into Taunton River and Mt. Hope Bay. Of major concern is the Fall River combined sewer system which has at least fourteen by-pass outfalls. The problem is accentuated by Fall River's hillside location whose steep slopes cause the residence time of runoff in the sewers to be extremely short.

In addition to the municipal discharges there are six thermal electric generating stations which withdraw water from the basin for cooling purposes and return it at elevated temperatures. The Brayton Point Station

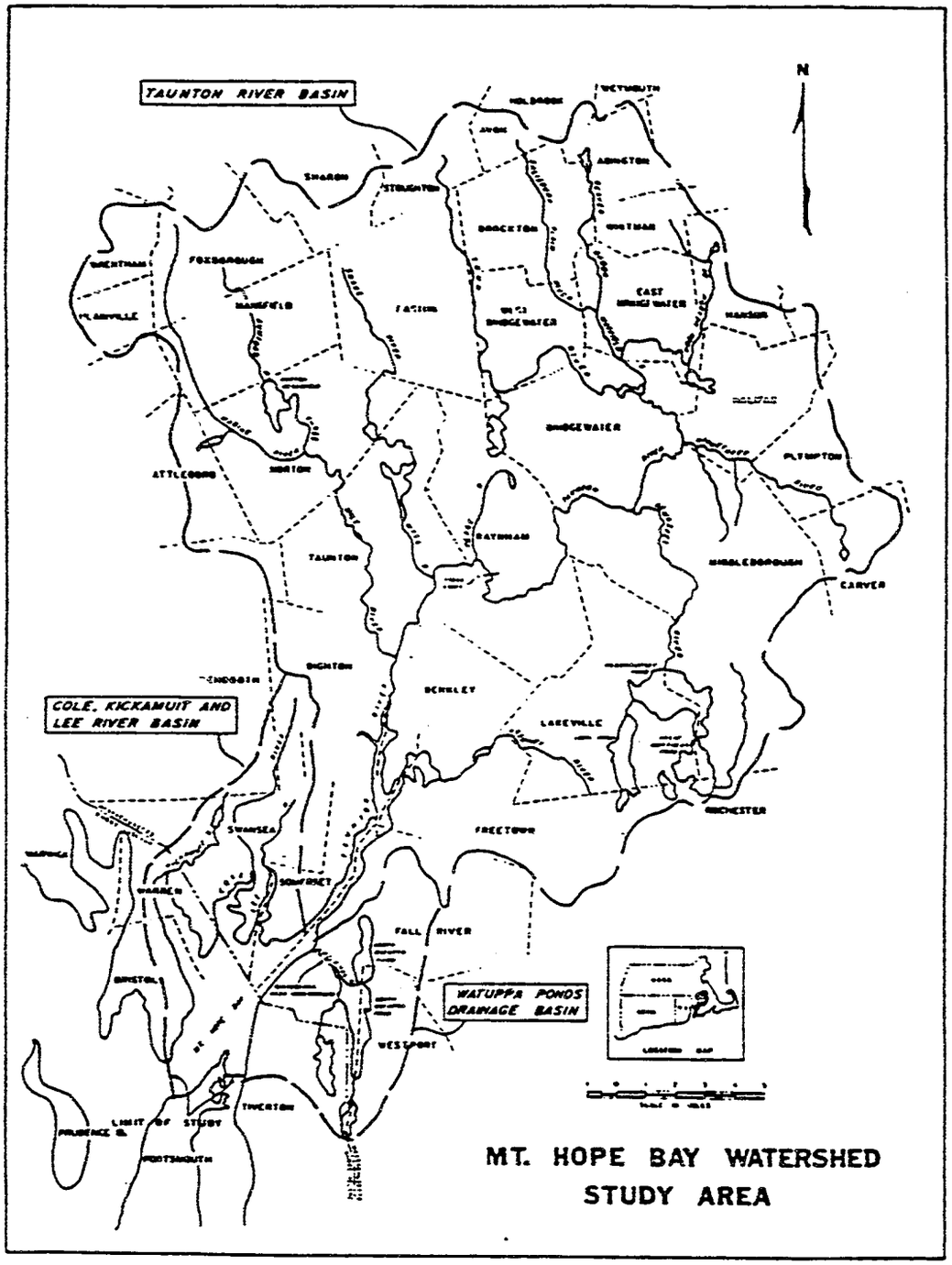

Figure 1.1 Mt. Hope Bay and Taunton River study area (EPA, 1971).

of the New England Power Company is the major source of heated effluent to Mt. Hope Bay contributing in excess of 1 million gpm at 8°C above ambient to the area. This is roughly 5 times the average flow rate of the Taunton River. To supplement this brief overview EPA (1971) provides a detailed summary of the principal pollutants entering the Mt. Hope Bay watershed. While over a decade old this report is the most recent summary of water quality in the area. (Personal communications; Phil Albert, Rhode Island Division of Water Resources and Paul Logan, Massachusetts Division of Water Pollution Control).

In summary Mt. Hope Bay, Taunton River, and its tributaries are heavily impacted by both domestic and industrial waste discharges. While the vast majority of these wastes are generated in Massachusetts they are ultimately transported into Rhode Island waters and provide a substantial source of contaminant input into Narragansett Bay. The entire area of Mt. Hope Bay is closed to shellfishing with conditional closure extending to portions of Narragansett Bay during heavy rainfall events.

Unfortunately little is known about how this material is transported through the bay or its ultimate flux into Narragansett Bay. Previous investigations of circulation in the region are extremely meager (see Bay Bib, Dunn et al., 1979). Haight (1936) describes a baywide (Narragansett and Mt. Hope Bay and Sakonnet River) program of current observations made mainly during a survey conducted in 1930 by the U.S. Coast and Geodetic Survey (now the NOAA National Ocean Service). The maximum observation period during the study was two days and a total of seven stations were monitored. The majority of the measurements were made by a weighted wooden pole.

In siting of the intake and thermal discharge structures for the Brayton Point power plant and its subsequent modifications Alden Research Laboratory (1970) performed a series of physical scale modeling studies of the circulation in the area immediately surrounding the plants. Model predictions were calibrated with an extremely limited series of short term observations. No data on circulation in the Taunton River could be found.

Numerical modeling of circulation and pollutant transport has been extremely active in Narragansett Bay proper over the last decade. For the vast majority of the modeling efforts however the Mt. Hope Bay region has not been addressed but treated only as a boundary condition for the Narragansett Bay models. The only exception is the two dimensional vertically averaged circulation model developed by Swanson and Spaulding (1974) and the three-dimensional wind-driven simulations of Gordon (1982). In the first study the Hess and White (1974) model was refined to a grid size of 400 m and extended to include Mt. Hope Bay and the Sakonnet River. A tidal height boundary condition was placed at Fall River to represent the connection of Mt. Hope Bay with the Taunton River. While the model grid size was adequate to describe the large scale circulation features of the area, the resolution was inadequate to describe the flows in the dredged channel system that dominates the south eastern side of Mt. Hope Bay and the lower reaches of the Taunton River (Figure 1.2). In addition the narrow passage (52 m wide) connecting Mt. Hope Bay to the Sakonnet River could not be accurately described with the grid system employed. The Swanson/Spaulding model was not verified for the area because of the lack of data.

Figure 1.2 Bathymetry of the Mt. Hope Bay area (NOAA/NOS).

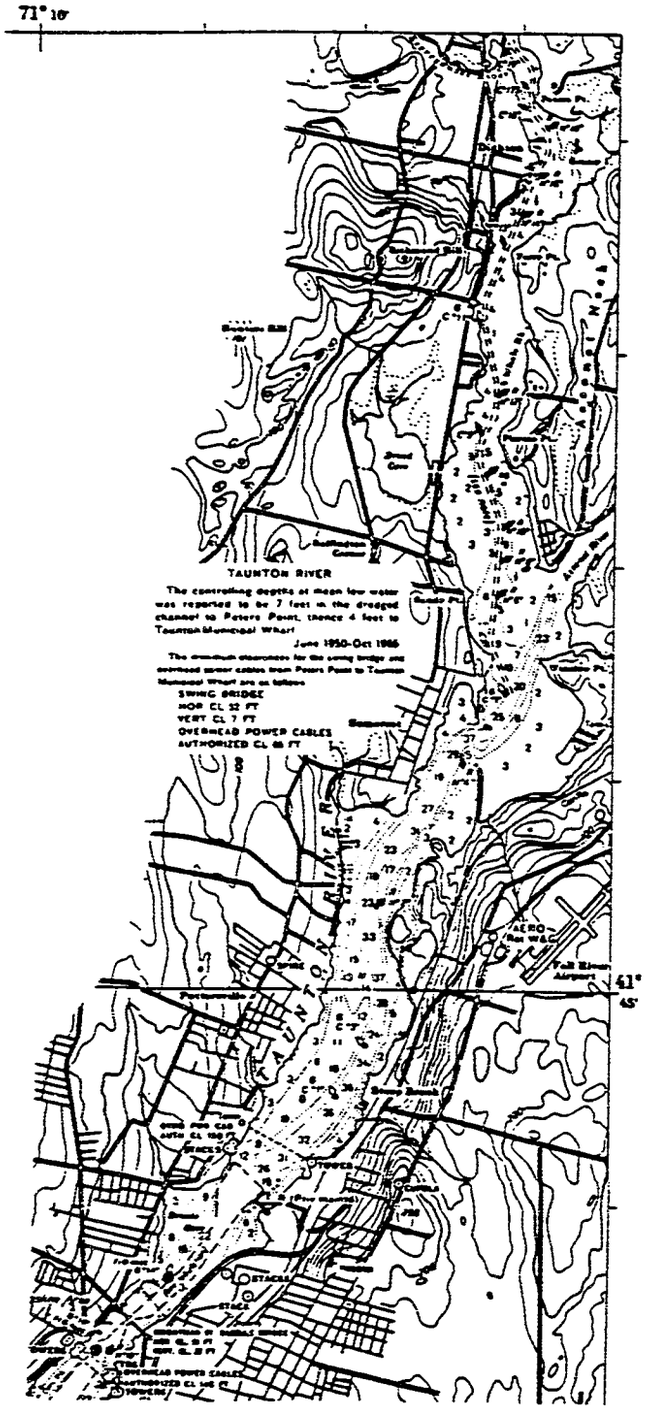

Figure 1.2 Continued.

The numerical model study performed by Gordon (1982) focused on the response of Narragansett Bay, including Mt. Hope Bay and the Sakonnet River, to wind forcing. Simulations were made using this three-dimensional model to study both local and non-local wind forcing on a 926 m square grid mesh. This choice of grid structure, based principally on computational time constraints, was inadequate to accurately represent Mt. Hope Bay and its connections to Narragansett Bay and the Sakonnet River.

No pollutant transport or water quality models have been developed for Mt. Hope Bay. The only pollutant modeling effort that seems to have been performed is the physical model studies of the thermal discharge from the Brayton Point power plant (ARL, 1970).

Pilson (1984) has recently performed extensive flushing estimates of Narragansett Bay, including Mt. Hope Bay. These simple calculations give useful gross scale estimates for the entire Bay system but do little to enhance our understanding of the controlling processes or the role of Mt. Hope Bay.

In conclusion, while the Mt. Hope Bay watershed (Taunton River and its tributaries, which represent 35% of the watershed for Narragansett Bay) contribute significant loads of pollutants to Mt. Hope Bay and acts as a source of contamination to the upper east passage of Narragansett Bay, we have neither data nor models to understand the circulation dynamics and pollutant transport and fate in the region. We also do not understand the partitioning of these pollutant fluxes between Narragansett Bay and the Sakonnet River.

The objective of the study is to describe the circulation dynamics in the Mt. Hope Bay-Taunton River system using a combination of field measurements and hydrodynamic models.

The specific goals of this investigation are:

1. Perform measurements of the current, surface elevation, salinity, and temperature to determine the transport of water and salt due to tidal, wind, and river flow forcing. Measurements will principally be made at three transects defining the boundaries of the study area and at selected stations within the bay proper.
2. Use the measurements to calibrate and verify a hydrodynamic model for the area. A two-dimensional vertically averaged hydrodynamic model will be used for Mt. Hope Bay.

A water quality model will be developed and applied to the area in a follow up study.

2. REVIEW OF PHYSICAL OCEANOGRAPHY OF STUDY AREA

The study area includes: Mt. Hope Bay and the Taunton River, extending to the head of the tide in Bridgewater, Massachusetts (Figure 1.1). The area is bounded on the west by Mt. Hope Bridge, on the south by the fixed bridge across the Sakonnet River at the Hummocks and by the former U.S. Geological Survey gauging station at the State Farm in Bridgewater, Massachusetts on the Taunton River. These boundaries are chosen mainly for the convenience of measurement locations.

Mt. Hope Bay is relatively shallow with 70% of the bay having a mean low water (MLW) depth of 6 m or less (Figure 1.2). Starting at Mt. Hope Bridge, a natural channel extends to a point between Mt. Hope and Common Fence Points. From this point a man-made channel 120 m wide with a MLW depth of 10.5 m extends to the north and up the Taunton River. A second channel with similar dimensions originates at Common Fence Point, extends easterly and then northerly toward Fall River. Finally a small channel, approximately 3 km south of the Taunton River mouth extends northwesterly from the central channel to the Brayton Point power plant.

Tidal fluctuations for Mt. Hope Bay, measured at Fall River, indicated a mean tidal range of 1.34 m, a maximum of 1.68 m for spring conditions and a minimum of 1.0 m at neap. The water column is generally well mixed throughout the year, although significant stratification may occur in salinity in the Taunton River during spring runoff (Hicks, 1959). Maximum tidal currents are typically 25 cm/s in the bay but can reach 2 m/s in the narrows connecting Mt. Hope Bay to the Sakonnet River.

Five rivers discharge into Mt. Hope Bay - the Taunton, Cole, Lee, Kickamuit and Quequechan. Together they represent 35% of the watershed for

Narragansett Bay (Pilson, 1984). The Taunton has the most significant input with an annual average discharge of 13.14 m^3/s over a 46 year period (1929-1976) measured at the State Farm gauge in Bridgewater, Massachusetts. Peak flows occur in the spring with values on the order of 20 m^3/s and minimum flows in the fall of 3 m^3/s. Combining this with the 4.8 m^3/s annually discharged by the Three Mile River gives a discharge of 17.94 m^3/s into Mt. Hope Bay. The Mill, Forge, and Assonet Rivers contribute significantly smaller amounts to fresh water in the tidal portion of the Taunton.

3. MEASUREMENT PROGRAM

3.1 Objectives

The primary purpose was to obtain a set of data to provide insight into how the movement of water and salt in the study area are influenced by meteorological, tidal and density forcing. The seasonal and spatial variation of these processes in the system is also of interest. The second purpose was to obtain data sets for the calibration and verification of hydrodynamic models of the area.

3.2 Data Acquisition

Six current meters were used in the study: five Endeco type 174 meters and one Marsh-McBirney model ARC-585 meter. The Endeco type 174 is a tethered, neutrally buoyant meter that measure in situ current speed and direction. On some meters measurement of temperature and conductivity is also possible. The meter moves on a tether to align with the local current field. Current speed is measured by a ducted propeller that is driven at a rate proportional to the magnitude of the local current. The propeller is connected to an encoded shaft through a reduction gear. The meter records the position of the encoded shaft at 5 minute intervals. The average current speed during each interval is determined by multiplying the shaft displacement during the interval by a conversion factor provided by the manufacturer (Endeco, 1979). The Endeco current meter swivels to align itself with the local current field and the direction of flow is measured by a compass in the meter. Ambient temperature is measured by a thermistor and conductivity by an electrodeless probe near the front of the instrument.

Recent calibration data for all meters was available from the manufacturer. Over the range of values anticipated for the study area expected instrument errors were small for current speed (<0.4 percent), temperature (<0.1 degrees Celsius) and conductivity (<1.0 micromho/cm).

The Marsh-McBirney meters employs Faraday's Law to sense current velocity and direction. Two pairs of electrodes protruding from the sensor sphere sense the magnitude of the electromagnetic field (EMF) generated by the conductive water moving past the sphere. The magnitude and polarity of the pair of EMF's is resolved by the meter into orthogonal velocities. The orientation of the electrodes is references to magnetic North-South and East-West velocities. These velocities are averaged over a two-minute period and mean values recorded every 10 minutes. Calibration data was not available for the Marsh-McBirney meters. The manufacturer's design specifications are included as Appendix A.1 of Turner (1984).

Wind and atmospheric data were obtained in hourly form from the National Weather Service Station at T.F. Green Airport, Warwick, Rhode Island, approximately 8 km west of Mt. Hope Bay. Weisberg (1974) found from an analysis of wind data at Green Airport and Quonset Point, 22 km distant, that the wind field was nearly uniform at periods greater than 12 hours. Winds were therefore assumed to be uniform in the Mt. Hope Bay - Green Airport area.

River flow data were obtained from the U.S. Geological Survey in Providence, Rhode Island for the Taunton River at the State Farm gauge at Bridgewater, Massachusetts. Daily average flow rates were obtained for the river during the study period. The data were spotty throughout the study period due to vandalism of the gauge.

Measurements of tidal height were made with tide gauges developed and constructed by the University of Rhode Island's Ocean Engineering Department. The tide gauge has a submerged transducer that senses hydrostatic pressure at a point in the water column. One side of the transducer membrane is subjected to ambient pressure at the measurement point while the other side is subjected to local atmospheric pressure, applied by a small plastic tube which extends from the transducer to a point above the water surface. The transducer membrane is thus subjected to a force which is proportional to strain in the membrane and hence to the water depth above the transducer. This output is amplified an recorded on solid state memory at five minute intervals.

Before deployment, the gauges were calibrated relating output voltage to water depth. The calibration was performed by immersing the pressure transducer known distances in a fresh water tank and recording the resulting voltage output from the gauge. The transducer was submerged over depth ranges similar to those anticipated during deployment. From the calibration data, a second-order least squares fit of the depth-voltage relation was obtained. The equation was later divided by a correction factor to account for mean temperature and salinity at the measurement point. Calibration data and curves for the tide gauge are shown in Appendix A.3 of Turner (1984).

The focus of the field measurement program was to determine the fluxes into and out of Mt. Hope Bay proper. Current measurements were made at the surface (15.9 m, referenced in the bottom), mid-depth (9.47 m), and bottom (3 m) at the Mt. Hope Bridge transect. At the Brightman Street transect measurements were made at the surface (6.86 m) and bottom (3 m). Only mid-

depth measurements (7.7 m) were made at the Sakonnet River at the Hummocks. Figure 3.1 shows the location of the observation stations. The vertical location of the meters were selected based on the depth of the water column, availability of instrumentation and the expected classical estuarine flow pattern (where saline water is transported landward near the bottom and fresher water is transported seaward at the surface). The latter factor was particularly important at the Brightman St. And Mt. Hope Bridge measurement points. Station locations were strongly influenced by a need to avoid damage from shipping traffic.

Four deployments were performed roughly corresponding to each of the four seasons. Figure 3.2 shows the times and lengths of the deployments for each station. The deployment number is given at the top of the figure. Dashed lines represent periods for which data were lost due to equipment failure or because the data quality was particularly poor. Recovery rates for tidal height data were extremely poor because of repeated instrument malfunctions. Noted above the line is the serial number for the current meter (011, 027, 029, 186, 229 - Endeco and 8338 - Marsh-McBirney) used at that location. All deployments were the same with exception of the fourth where the Sakonnet River meter was moved to a location in the middle of the bay at mid-depth (2.9 m). This change was made to gather data from the central part of Mt. Hope Bay, since the Sakonnet measurement station showed extremely small tidal currents.

A fifth deployment was made to gather additional flows through the Mt. Hope Bridge transect. We were specifically interested in more closely studying the lateral variability of the current through the transect. The long-term mean flow was of particular concern. The meter locations for

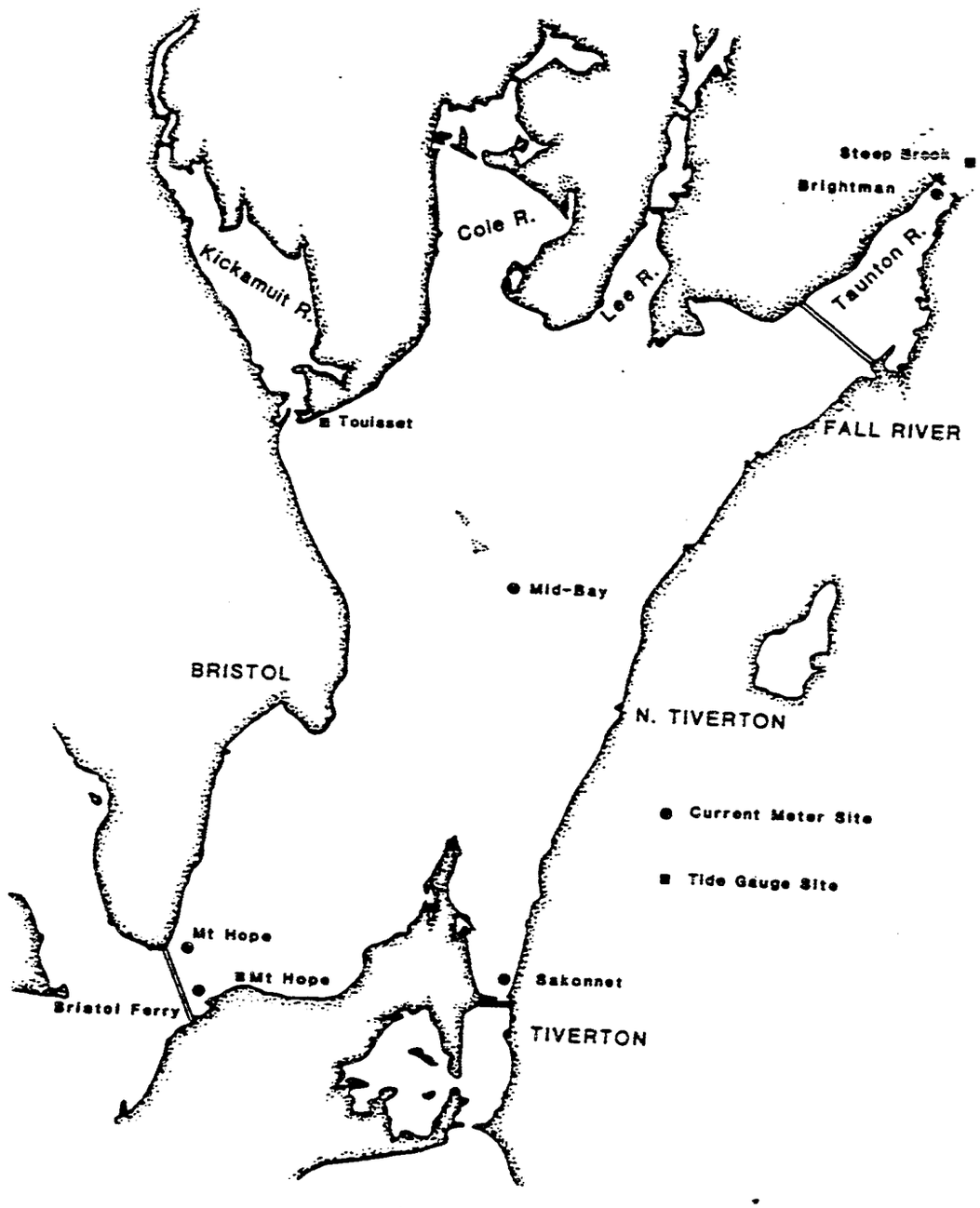

Figure 3.1 Location of current and sea elevation observation stations in Mt. Hope Bay and the lower Taunton River.

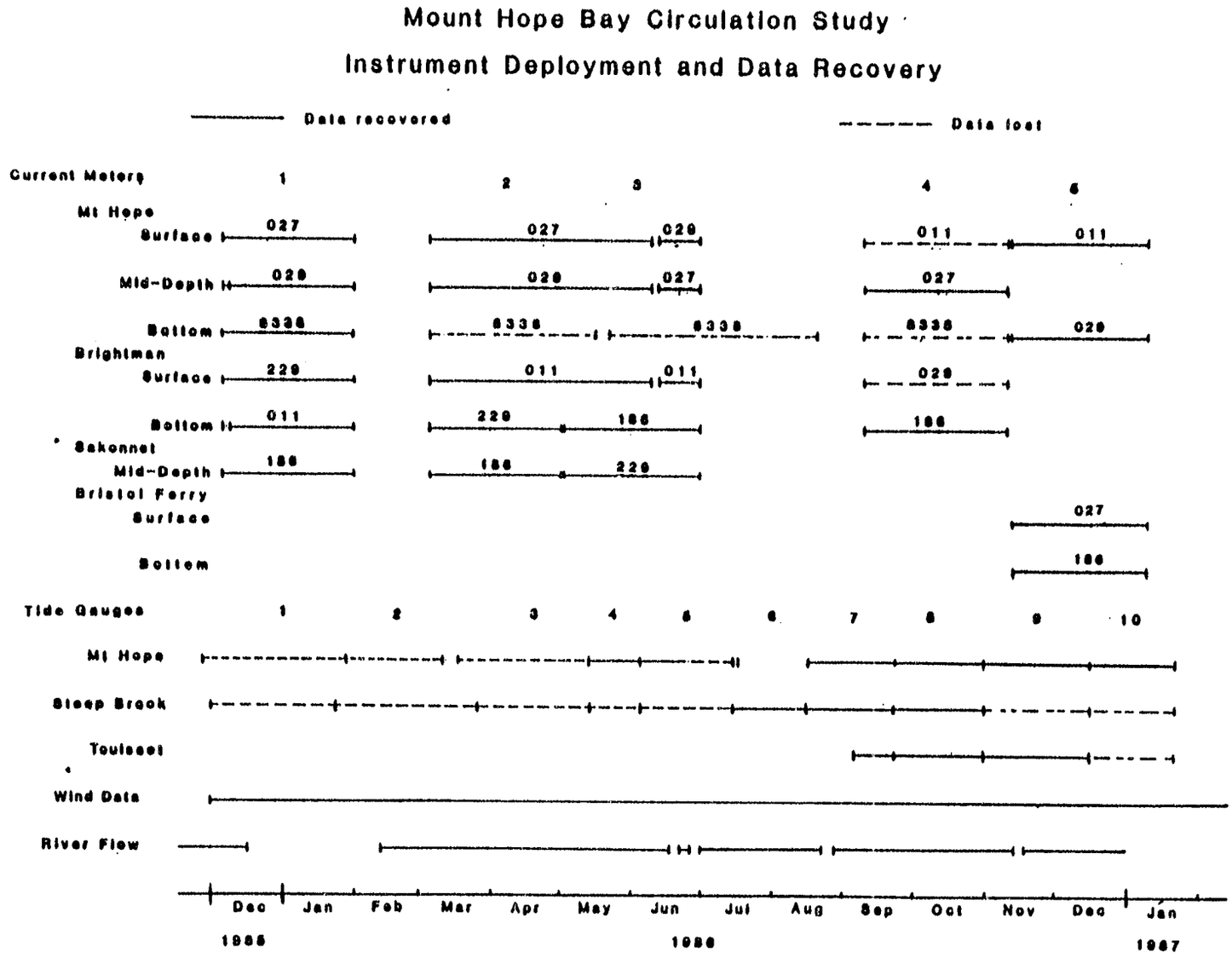

Figure 3.2 Time schedule for field measurement program.

this deployment are illustrated in Figure 3.3. While it was desirable to have meters in the center of the channel this was not possible due to shipping traffic that uses this central channel.

Tidal height measurements were made throughout the study period at Mt. Hope Bay entrance, Steep Brook in the Taunton River and at Touisset. The locations are shown in Figure 3.1. The data return from these gauges was very poor during the study due to mechanical/electronic failures and recording problems.

An intensive tidal cycle survey was performed on May 20, 1986. Measurements of temperature, salinity and currents were made at 10 stations throughout Mt. Hope Bay and the lower Taunton River. Measurements stations are shown in Figure 3.4. Temperature and salinity were recorded at 1 m depth intervals using a Beckmann RS5 salinometer and thermister. Current measurements were made using a single axis Marsh-McBirney electromagnetic current meter. Directional information could only be determined for the top measurement point since it required a visual estimate of meter orientation. The current data is questionable because of wind and wave induced motion of the small boat used as the measurement platform.

3.3 Data Analysis Procedures

3.3.1 Tidal Forcing Method

Analysis of the current meter data was focused on identifying the response to tidal, meteorological, and density induced forcing. Free surface and current field response to tidal forcing were determined using a modified version (Carrier et al, 1982) of the harmonic analysis method of Dennis and Long (1971). The harmonic method assumes that h(t), the height

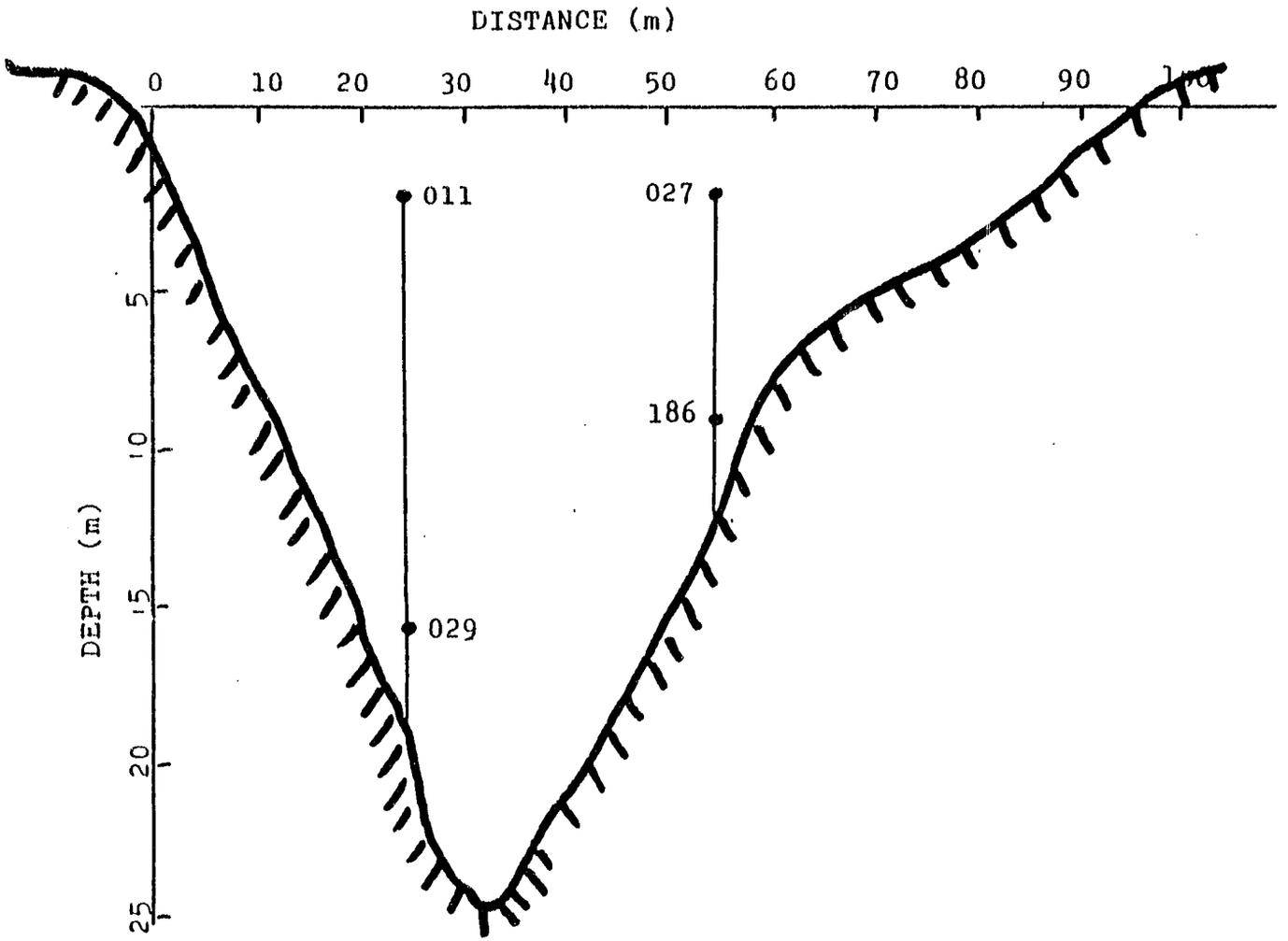

Figure 3.3 Location of current meters in the Mt. Hope Bridge transect for the fifth deployment (Figure 3.2).

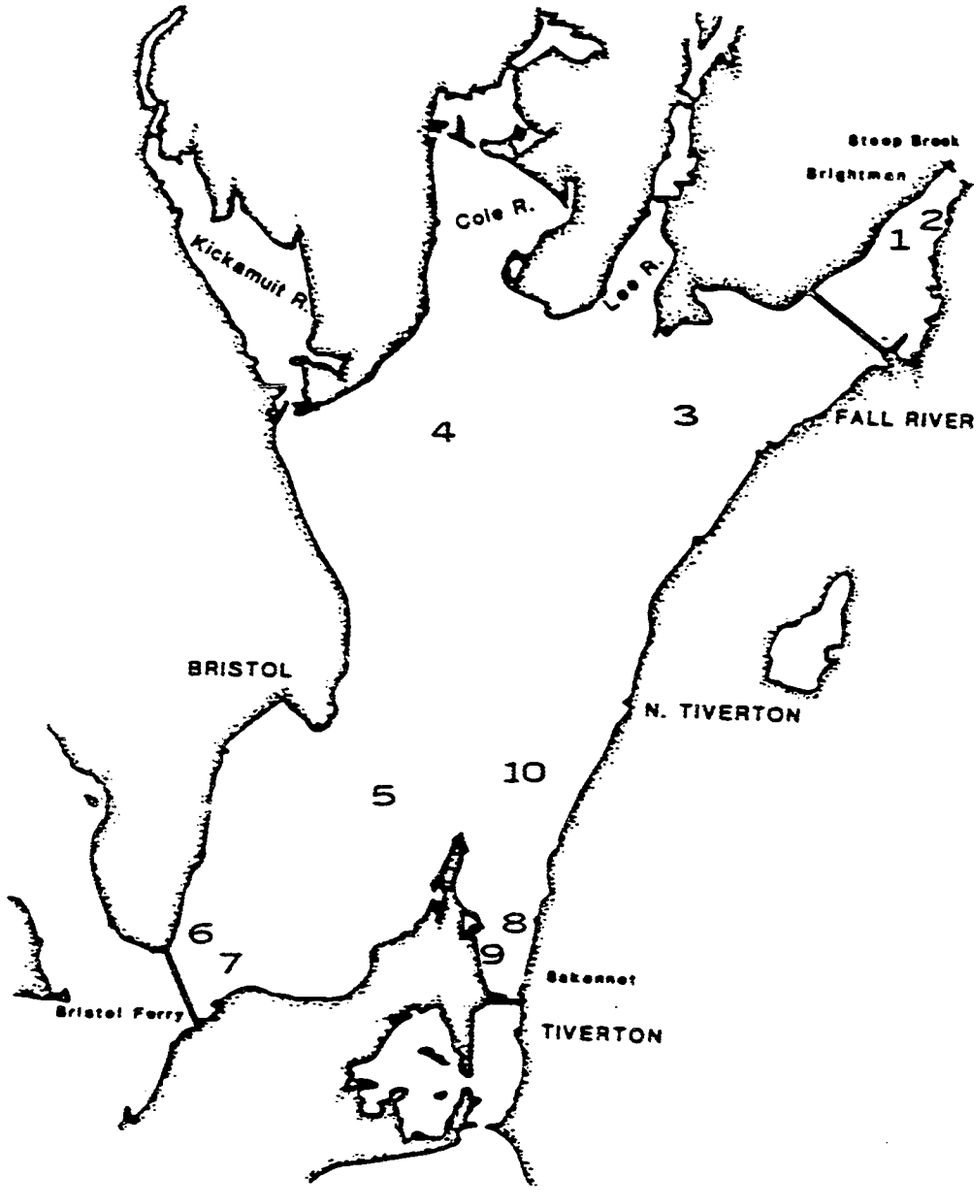

Figure 3.4 Location of intensive tidal cycle survey measurements on May 20, 1986.

of tide or current at some arbitrary time t, may be expressed as the sum of the Fourier series:

$$h(t) = h_o + \sum_{n=1}^{N} f_n h_n \cos \{\omega_n t - (K_n - [v_o + u]_n 0)\} \qquad (3.1)$$

for which:

h_o = mean tide or current level of the series

t = time relative to an arbitrary reference

h_n = the mean amplitude of the constituent

f_n = the node factor, a small amplitude correction to the mean amplitude which accounts for amplitude changes caused by the precession of the moon-earth plane about the ecliptic the phase speed of the constituent. (See Table 3.1.)

K_n = the local epoch, the phase difference between the local transit of the forcing constituent and the arrival of the peak of the constituent's tidal wave. K_n is a constant for a given location.

$[v_o + u]_n$ = The phase difference between the local transit of the forcing constituent and the start of the measured time series.

When given the frequencies ω_n of the constituents expected to be most significant at the measurement site, the analysis program first solves for the amplitudes and phases of a ten-constituent Fourier series (M_2, S_2 N_2, O_2, K_1, M_4, M_6, M_8, S_4 and S_6) that is the best least squares approximation of the input time series. The periods of these constituents are given in Table 3.1. The program then converts the phase of each constituent frequency to local epoch and Greenwich epoch format and corrects each constituent amplitude for the node factor f_n to obtain the

Table 3.1 Tidal constituent phase speeds and periods.

Constituent	Phase Speed (degress/solar hour)	Period (solar hours)
M_2	28.984	12.42
N_2	28.440	12.66
S_2	30.000	12.00
O_1	13.943	25.82
K_1	15.041	23.93
M_4	57.963	6.21
M_6	86.952	4.14
O_2	27.886	12.91
S_4	60.000	6.00
M_8	115.936	3.10

mean constituent amplitude. The program infers magnitudes and phases for minor constituents whose frequencies are close to those of the ten major constituents listed above. Finally, it adjusts the phases and magnitudes of the major constituents to correct for the disturbing influence of adjacent minor constituents. Detailed descriptions of the harmonic analysis process may be found in Schureman (1941), Dennis and Long (1971) and Turner (1984).

Tidal constituent phases for a location are typically expressed as either Greenwich epoch or modified epoch. Most tidal constituent data for Mt. Hope and Narragansett Bays have been reported in modified epoch notation. Tidal phase data will therefore be reported in that form.

3.3.2 Wind Forcing Method

Local surface winds were identified by Weisberg (1974, 1976) as the most important forcing mechanism for current at periods between the tidal band and the quasi-steady gravitational currents in the lower Providence River. In linking the low frequency current fluctuations with the local wind field, Weisberg examined the frequency domain relationship between the two-dimensional wind vector series and the one-dimensional axial current speed series by using a multiple-input linear analysis technique. With this method, the one-dimensional output series is expressed as the sum of the frequency domain filtering of the two input series (the North-South and East-West components of wind stress) by two transfer functions which are assumed to be time-invariant, at least for the duration of the measurements. The difference between this method and the more common one-input/one-output technique is that the two inputs are allowed to be

partially coherent with each other. When the transfer function between each input and the output is determined for the multiple input case, the effects of coherent inputs are removed. As a result, overestimation which may result from using ordinary transfer functions is avoided. The method is described in more detail in Weisberg (1974, 1976).

3.3.3 The Low Pass Filter

Low-pass filtering of the data was accomplished using a fourth order Butterworth filter (Stearns, 1975). The phase shift inherent in the Butterworth filter is eliminated by passing the data forward and then backward through the filter. The impulse response of the filter and a comparison of its cutoff characteristics with those of other low pass filters commonly used in the oceanographic community are given in Turner (1984). When compared with other filters, the Butterworth filter offers the advantages of easy implementation, minimal computer execution time, and good frequency response. The reader is referred to Turner (1984) for a detailed discussion of the exact procedure employed for filtering the data.

4. ANALYSIS OF FIELD MEASUREMENTS

An analysis of the data collected during the field program is described in the paragraphs to follow. In addition, data products for all field data are included in the appendices as summarized below:

Appendix A	Current Meter Time Series (Raw and Filtered)
Appendix B	Progressive Vector Diagrams for Current Meter Data (Raw and Filtered)
Appendix C	Power Spectra of Current Meter Data and Normalized Power Distribution
Appendix D	Harmonic Analysis of Sea Surface Elevation Data
Appendix E	Intensive Tidal Cycle Surveys
Appendix F	Charts of Coherence between Wind and Stress and Current
Appendix G	Current Meter Speed and Direction Histograms

4.1 Tidal Circulation

The harmonic method was used to extract tidal constituent amplitudes and phases from the sea surface elevation and current meter data obtained during the experiment. Current records are referenced to their location, duration, and start and end dates in Table 4.1. Similar information is given for selected surface elevations in Table 4.2.

TABLE 4.1 Location, duration, and start and end dates for current observations

Location*	Duration (days)	Start Date	End Date	Notes
MTHOPE 1.027	58	12/4/85	1/31/86	
MTHOPE 1.029	58	12/4/85	1/31/86	Last 4 days of record bad
BRIGHT 1.229	58	12/4/85	1/31/86	
BRIGHT 1.011	55	12/7/85	1/31/86	
SAKONN 1.186	58	12/4/85	1/31/86	
MTHOPE 1.8338	--	12/4/85	1/31/86	Data quality poor
MTHOPE 2.027	97	3/4/86	6/9/86	
MTHOPE 2.029	97	3/4/86	6/9/86	
BRIGHT 2.011	97	3/4/86	6/9/86	
BRIGHT 2.229	58	3/4/86	5/1/86	
SAKONN 2.186	57	3/4/86	5/1/86	
MTHOPE 3.029	18	6/12/86	6/30/86	
MTHOPE 3.027	18	6/12/86	6/30/86	
BRIGHT 3.011	18	6/12/86	6/30/86	
BRIGHT 3.186	59	5/2/86	6/30/86	
SAKONN 3.229	59	5/2/86	6/30/86	Only first 9 days retrievable. Meter fouled
MTHOPE 4.027	59	9/9/86	11/7/86	
BRIGHT 4.186	59	9/9/86	11/7/86	Data quality poor.
MTHOPE 5.011	78	11/25/86	2/11/87	
MTHOPE 5.029	78	11/25/86	2/11/87	
BRISTLF 5.027	78	11/25/86	2/11/87	
BRISTLF 5.186	78	11/25/86	2/11/87	

*Meter locations: MTHOPE - Mt. Hope Bridge; BRIGHT - Brightman St. Bridge; SAKONN - Sakonnet Bridge: BRISTLF - Bristol Ferry - Deployment Number. Current Meter Serial Number (e.g. 1.027 Deployment 1, Endeco 174 Serial #027). Serial Numbers - 027, 029, 186, and 229 Endeco Type 174 Current Meter; 8338 - March McBirney double axis electromagnetic

Table 4.2 Location, duration, and start and end dates for sea elevation observations.

Location	Duration (days)	Start Date	End Date
Mt. Hope Bridge	29	9/1/86	9/30/86
Steep Brook	29	9/1/86	9/30/86
Touisset	12	8/5/86	8/18/86

Note: Figure 3.2 indicates that there is more data available than noted here. Data for other time periods, however, was badly contaminated by instrument and data recording problems and hence has not been included here.

Tables 4.3 and 4.4 contain the results of the harmonic analysis (Section 3.3.1) of the tide height and current meter data, respectively. The first six characters of the current meter data sets in Tables 4.1 and 4.3 refer to the last three or four characters, after the decimal point, refer to the meter serial number. Hence, data set MTHOPE2.027 refers to the Mt. Hope Bridge data set, Endeco meter 027 for the second deployment. The 1977 NOS analysis (Turner, 1984) for Steep Brook and Anthony Point tide gauge records are reported as convenient references in Table 4.4.

The tide height records revealed that tidal forcing accounts for about 80 to 95 percent of the free surface fluctuations in Mt. Hope Bay. Tidal fluctuations are predictably dominated by the M_2 constituent with an amplitude of 57.6 cm at Mt. Hope Bay entrance and 56.7 cm at Steep Brook. The Touisset record shows an amplitude of only 49.5 cm but the record length is too shore to provide an accurate measure of even the M_2 tide. The M_2 constituent, which effectively represents the mean semi-diurnal

Table 4.3 Amplitudes and phases of the principal tidal constituents from analysis of current meter records.

	RECORD LENGTH (HR)	M(2) ORIEN (DEG T)	M(2) AMP (CM/S)	M(2) PHS (DEG)	N(2) AMP (CM/S)	N(2) PHS (DEG)	S(2) AMP (CM/S)	S(2) PHS (DEG)	O(1) AMP (CM/S)	O(1) PHS (DEG)	K(1) AMP (CM/S)	K(1) PHS (DEG)	M(4) AMP (CM/S)	M(4) PHS (DEG)	M(6) AMP (CM/S)	M(6) PHS (DEG)
Mount Hope Mooring																
Surface Meter																
MTHOPE1.027	1391	33.4	30.202	96.4	5.191	56.4	5.904	90.4	1.403	107.7	1.447	75.0	7.738	170.4	2.234	22.4
MTHOPE2.027	2327	27.7	22.190	94.1	5.432	72.0	6.110	120.5	1.015	126.9	1.658	80.0	6.420	177.2	2.767	51.9
MTHOPE3.029	433	26.2	26.288	90.7	4.679	87.4	5.978	55.2	0.308	82.5	1.438	115.4	6.243	166.5	5.373	33.0
MTHOPE5.011	1808	27.3	26.739	83.3	3.802	60.4	5.927	87.3	1.422	101.1	1.497	72.7	4.801	128.7	2.054	173.7
Mid-Depth Meter																
MTHOPE1.029	1319	29.3	27.458	89.3	5.583	62.0	5.121	97.1	0.991	103.8	1.109	88.7	8.209	176.7	1.963	22.3
MTHOPE2.029	2327	28.1	19.413	84.1	4.108	52.1	3.840	112.0	0.813	130.4	0.743	47.0	6.292	178.3	2.162	44.5
MTHOPE3.027	433	28.1	19.225	86.5	4.202	51.1	3.458	121.5	0.585	10.0	0.472	128.7	7.584	177.0	3.103	25.3
MTHOPE4.027	1417	26.0	17.948	78.4	4.153	46.7	3.234	108.4	0.681	66.6	0.711	38.5	6.308	9.2	3.483	19.1
Bottom Meter																
MTHOPE5.029	1868	21.9	13.523	55.6	2.684	41.3	3.020	105.3	0.546	50.6	0.174	49.4	3.524	152.1	1.350	167.7
Bristol Ferry Mooring																
Surface Meter																
BRISTF5.027	1867	54.2	35.336	102.0	6.917	78.2	8.329	114.5	2.363	109.8	2.449	81.1	13.042	147.1	2.634	94.0
Bottom Meter																
BRISTF5.186	1867	53.2	24.952	101.2	6.242	79.5	6.512	129.7	1.431	101.8	1.206	69.4	11.359	162.6	2.925	83.4
Brightman Street Mooring																
Surface Meter																
BRIGHT1.229	1392	41.3	34.568	112.0	7.736	97.1	7.227	129.5	1.557	136.8	1.992	112.2	10.156	175.4	5.658	100.6
BRIGHT2.011	2328	39.1	26.941	111.3	6.711	103.1	6.295	136.5	0.831	141.5	1.638	102.7	8.146	176.0	4.851	107.0
BRIGHT3.011	434	39.9	28.547	112.0	6.607	80.1	6.413	116.9	0.974	137.7	1.313	102.2	10.114	170.6	6.172	97.6
Bottom Meter																
BRIGHT1.011	1320	41.6	20.882	94.6	7.141	83.4	6.208	134.5	0.762	84.3	1.295	94.0	9.363	149.7	4.370	93.3
BRIGHT2.229	1390	43.0	15.218	93.8	4.849	90.1	4.146	133.3	0.205	100.0	1.294	57.6	8.191	147.1	3.850	94.6
BRIGHT3.186	1418	45.8	12.709	96.0	2.617	82.3	2.963	132.6	0.675	98.0	0.909	65.8	6.551	151.9	2.803	104.0
BRIGHT4.186	1414	45.7	11.801	102.9	3.342	79.6	2.802	129.0	0.583	101.5	1.075	83.7	5.460	162.3	2.875	106.8
Sakonnet River Mooring																
Mid-Depth Meter																
SAKON1.186	1300	6.3	4.884	40.2	0.263	55.5	0.922	180.9	0.743	57.6	0.467	60.1	3.318	69.5	0.644	163.8
SAKON2.186	1368	10.6	4.409	49.6	1.250	83.5	0.933	138.5	0.109	20.1	0.099	39.4	3.955	73.6	0.520	23.6
SAKON3.229	1418	6.3	0.522	45.9	0.350	97.5	0.402	175.0	0.082	12.7	0.029	1.7	0.389	105.6	0.100	139.9

TABLE 4.4 Amplitudes and phases of the principal tidal constituents from analysis of the sea surface elevation records.

Location	DURATION (days)	Constituent Amplitude (cm) and Phase (°G)													
		M_2		N_2		S_2		O_1		K_1		M_4		M_6	
MT HOPE BRIDGE	29	57.6	184	8.1	229	12.6	216	4.1	108	9.6	80	7.9	56	1.1	136
ANTHONY POINT (NOS,1977)	29	49.9	218	10.4	201.6	12.5	236	5.7	123.6	6.0	96.5	5.9	119.7	1.3	190.9
STEEPBROOK	29	57.2	180	9.1	207	10.1	220	5.8	123	1.6	71	10.5	55	2.8	151
STEEPBROOK (NOS,1977)	29	56.7	224.8	12.1	208.6	14.4	243.8	5.8	121.5	6.1	100	10.1	144.9	2.9	264.9
TOUISSET	12	49.5	228	10.9	345	7.9	202	15.3	132	15.1	140	8.5	169	3.2	303

NOTE: The 12 day record length at Touisset is inadequate to provide an accurate representation of the semi diurnal or diurnal tides.

tidal wave is modulated by the S_2 (17.6 cm) and N_2 (8.1 cm) constituents at periods of 14.8 and 27.6 days, respectively. The interaction of the three constituents causes the semi-diurnal wave amplitude to vary between 37 cm at extreme neap conditions to 78 cm at extreme spring conditions.

The amplitudes of the two significant diurnal constituents, O_1 (4.1 cm) and K_1 (9.6 cm), are about 7-16 percent that of the M_2 constituent. Their only significant contribution to the tidal character of the area is to create a diurnal inequality, or mismatch in the two high tides (and low tides) each day.

The M_2 overtide is the fourth largest constituent in the Taunton River, with an amplitude of approximately 10.1 cm. In spite of its relatively small amplitude, the M_4 constituent has a significant impact on the tidal nature of the area. The sum of the M_4 tide and the dominant semi-diurnal tide (M_2) produces tidal fluctuations with the duration of the flood portion which is longer than the ebb. The M_4 constituent also causes an inflection in the tidal height curve that is most apparent at neap conditions (Turner, 1984).

Tidal forcing also dominates the current variance. Tidal forcing accounted for 87 percent of the variance for the Mt. Hope Bridge records, and 93 to 58 percent of the Brightman Street and Sakonnet record variances, respectively.

Tidal currents in the bay are again dominated by the M_2 constituent, which have a vertically averaged mean amplitude of 20.3 cm/s, 22.6 cm/s, 30.1 cm/s and 4.6 cm/s at Mt. Hope Bridge, Brightman St. Bridge, Bristol Ferry, and Sakonnet, respectively. The near surface currents at Mt. Hope Bridge and Brightman St. Bridge are twice as high as the near bottom

currents but only 50% higher at Bristol Ferry. The N_2 and S_2 constituents have approximately one fifth the magnitude of the M_2 and interact with it to create the neap-spring variation in the semi-diurnal band. The magnitudes of the diurnal constituents (O_1 and K_1) are quite small, on the order of 1-2 cm/s, while the M_4 and M_6 overtides are quite significant, 7-10 and 3-5 cm/s, respectively for the Mt. Hope and Brightman St. Bridge stations. The ratio of M_2 /M_4 increases slightly from 0.28 at Mt. Hope Bridge to 0.37 at Brightman St. Bridge and indicates that tidal energy at the M_2 frequency is transferred to its harmonic (M_4) as the tide passes through the bay.

Haight (1936) suggests that the ratio of current velocity to tidal height amplitude is inversely proportional to the period of the constituent. Thus, the M_4 constituent, with approximately the same tidal height amplitude as the diurnal constituents at Mt. Hope Bridge, has a current amplitude approximately 4 times as great as that of the diurnal constituent. The M_4 and M_6 constituents combine with the semi-diurnal constituents to create a double peak in current velocity during the flood portion of the tidal cycle. This effect is shown graphically in Haight (1936) and Turner (1984). The double flood effect is most apparent in the neap tide condition, since the sum of the M_2, N_2, and S_2 constituents minimizes the magnitude of the semi-diurnal signal at that time.

Between the Mt. Hope Bridge and Steep Brook stations, the constituents based on surface elevation show very little change in phase and amplitude. The lunar semi-diurnal tide changes by 4 degrees in phase but by less than 1 percent in amplitude. The M_4 constituent phase changes by 1 degree and

its amplitude increases by 33 percent. The diurnal constituents are constant but relatively noisy.

The uncertainty in the tidal constituent amplitudes and phases which result form non-tidal fluctuations in the data (Turner, 1984) are probably equal to or greater than their variations in the study area. The tidal motion of the free surface may therefore be approximated as simultaneous throughout the bay. If the length of the river and bay are compared to the expected length of the tidal wave, the idea of simultaneous motion appears to be quite reasonable. The progressive component of the wave is therefore quite small, and is barely discernible through the background noise.

When the phase difference between the free surface elevation and tidal currents is examined, tidal motion in the bay resembles that seen in a standing wave. In a progressive wave, currents and free surface elevations are in phase. Maximum forward particle velocities in the wave are reached at the wave crest (high tide). Maximum velocities opposite to the direction of wave travel are reached at the wave through (low tide). In a standing wave, however, particle velocity phases precede free surface elevations by 90 degrees. Maximum flood and ebb currents therefore precede high and low tides by one quarter of the wave period. At Mt. Hope Bridge the averaged tidal surface current leads the tidal free surface elevation by about 89 degrees. Thus, the approximation of the tide in the bay as a standing wave appears to be appropriate.

The noise-related uncertainty associated with the constituents is also important in examining their variability at a point in the river. As seen in Turner (1984) changes in the constituents between data sets are comparable to the expected error associated with the data. The response to

tidal forcing at a point in the estuary therefore appear to be constant, which temporal variations in the estuary therefore appears to be constant, interference in the analysis response.

4.2 Wind-Driven Circulation

4.2.1 Characteristics of the Wind-Driven and Non-Tidal Currents

The results of Section 4.1 clearly show that tidal influences are the dominant contribution to the current patterns in Mt. Hope Bay. Section 4.3 will discuss the influence of density gradients. Here we examine the effects of the wind.

Narragansett Bay is a windy environment throughout the year. Figure 4.1 shows monthly-average wind speed and direction at Green Airport during 1986. Wind speeds averaged 5 m/s during the winter and spring and 4 m/s during summer and fall. The winds tended to approach from the north west in winter and spring and from the southwest in summer and fall. These results for the single year 1986 agree with the longterm trends plotted and discussed by Turner (1984).

Power spectra of the Green Airport winds have been computed by Turner (1984, Figs. 5.9A-E). These spectra show a peak wind energy at periods ranging from 3 to 10 days, corresponding to the passage of weather systems through the area. There is also a smaller peak in summer at a frequency of 0.042 cycles/hr corresponding to the diurnal sea-breeze. Integration of these wind spectra shows that approximately 75% of the wind energy is contained at frequencies less than 0.033 cycles/hr, or periods greater than 30 hours. One therefore expects these low-frequency wind events to have the greatest influence on Mt. Hope Bay currents.

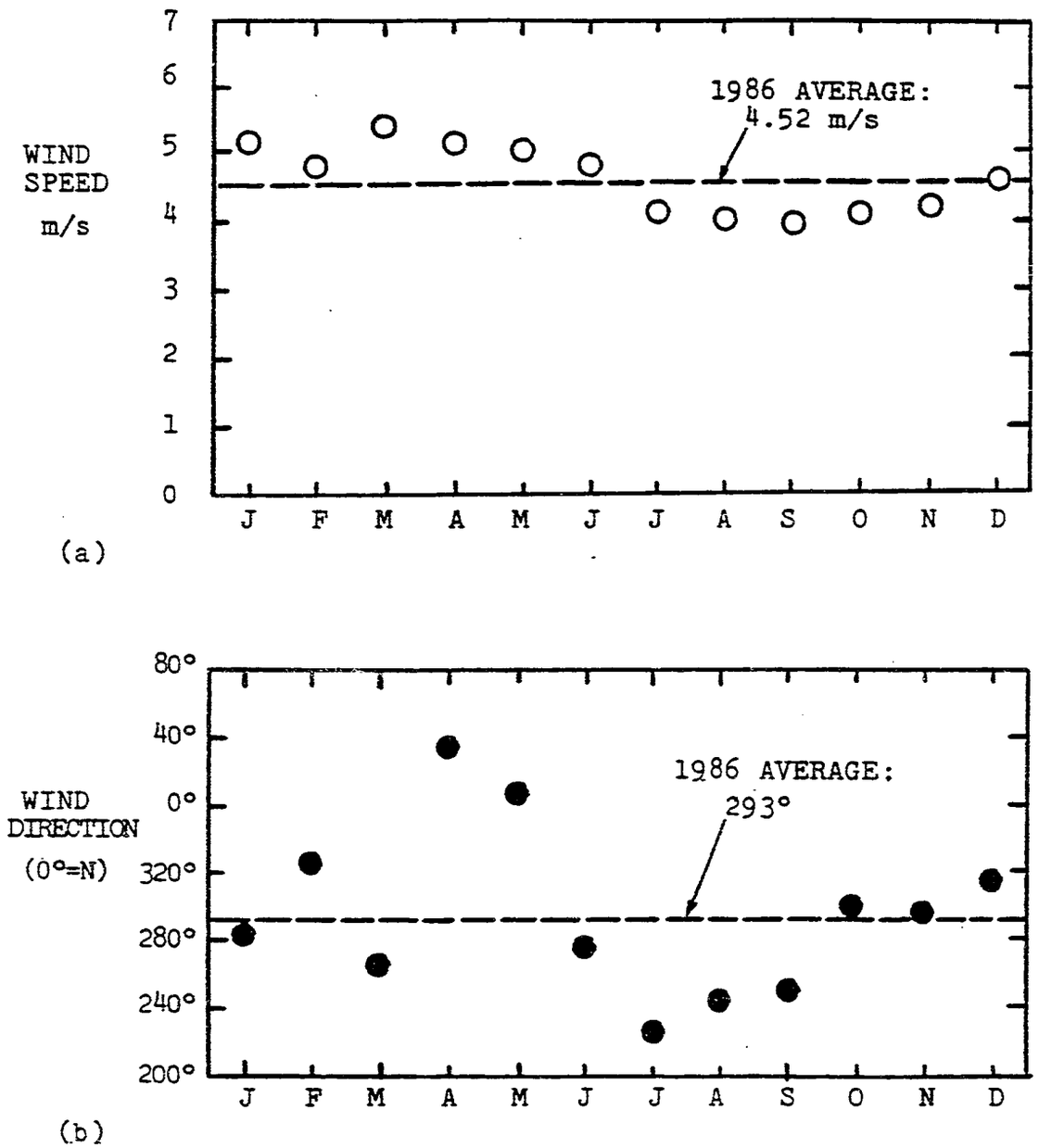

Figure 4.1 Monthly average winds during 1986 at Green Airport in Warwick, Rhode Island: (a) wind speed; (b) direction (from NOAA 1986 Local Climatological Data, Annual Summary, Providence, Rhode Island ISSN 0198-4594).

Let us examine a particular station in detail, Figure 4.2 shows winds, barometric pressure, and Taunton River freshwater flow combined in a stack-plot with the raw current meter, salinity, and temperature data during March 1986 at the surface at the Brightman station, deployment 2.011. The current speeds and salinity variations are dominated by tidal oscillations. Temperature is only moderately affected by the tides. The raw data does not illuminate any obvious wind effects, although there is probably a connection between the high river flow on March 17th and the sharp drop in river salinity two day later.

Figure 4.3 shows the same time series of Figure 4.2 but with the current, temperature, and salinity data processed though a low-pass filter which removes all energy at periods below 30 hours. Residual currents from 2 to 5 cm/s persist in the filtered record and vary with periods from 1 to 3 days. Axial residual currents are seen to be moderately correlated with either wind or river flow.

An indication of the overall effect of winds on the measured currents in Mt. Hope Bay can be found by examining the power spectra of the current data. Figure 4.4(a) shows the frequency spectrum of N/S and E/W currents from the Brightman deployment 2.011 whose raw data was shown earlier in Figure 4.2. We see a moderate amount of low-frequency energy, sharp peaks at the dominant tidal frequencies (O_1, K_1, N_2, M_2, M_4, M_6), and slight energy at high frequencies. The partitioning of energy over various frequencies is shown in Figure 4.4(b), which is the cumulative energy computed by integrating Figure 4.4(a) over frequency to a normalized total of 1.00 or 100%. Low and high frequencies in this figure are seen to contribute only a few percent of the total energy. The dominant

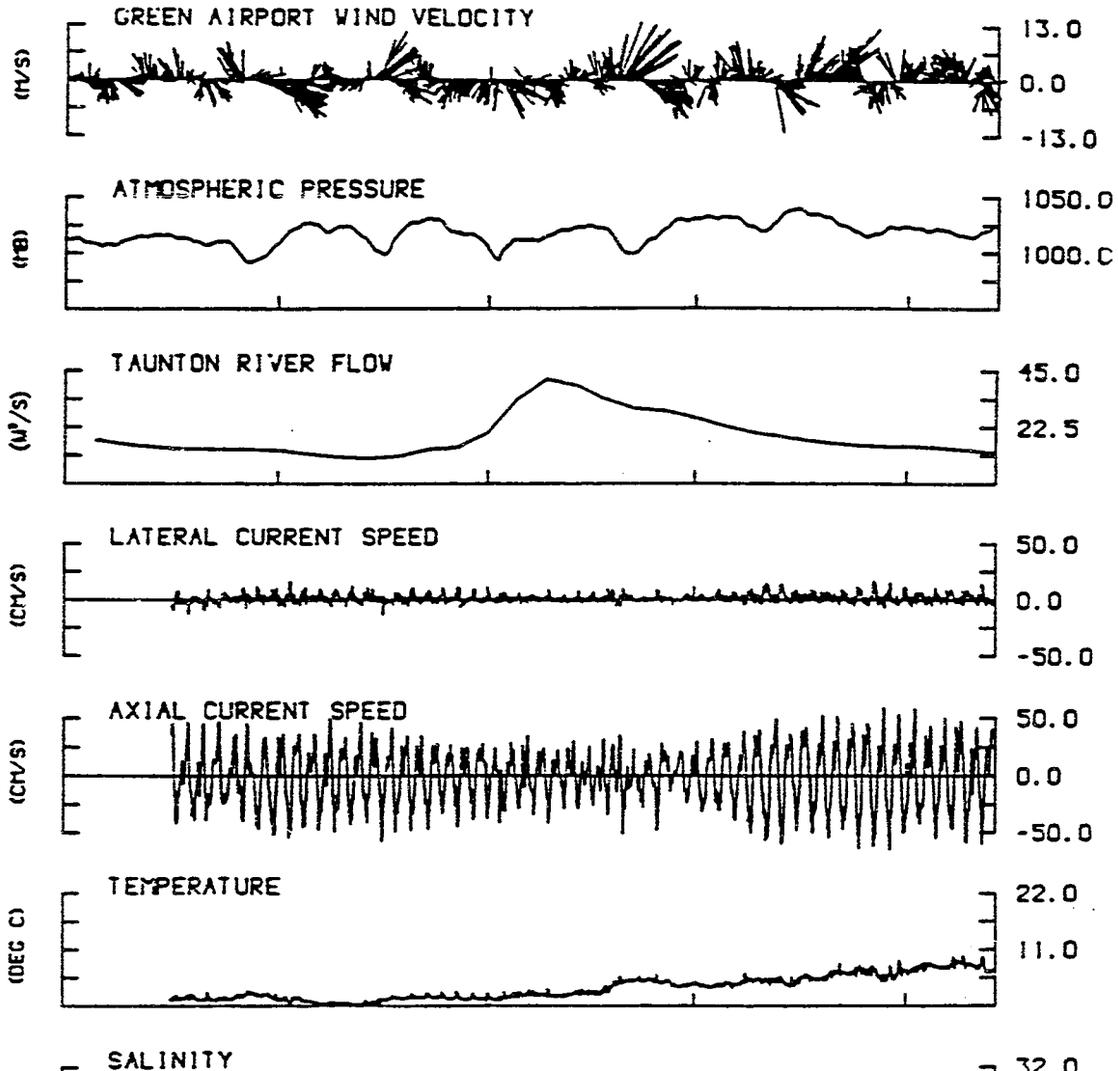

Figure 4.2 Wind, barometric pressure, and river-flow inputs compared with raw meter data at the surface at Brightman station for deployment 2.011 during March 1986.

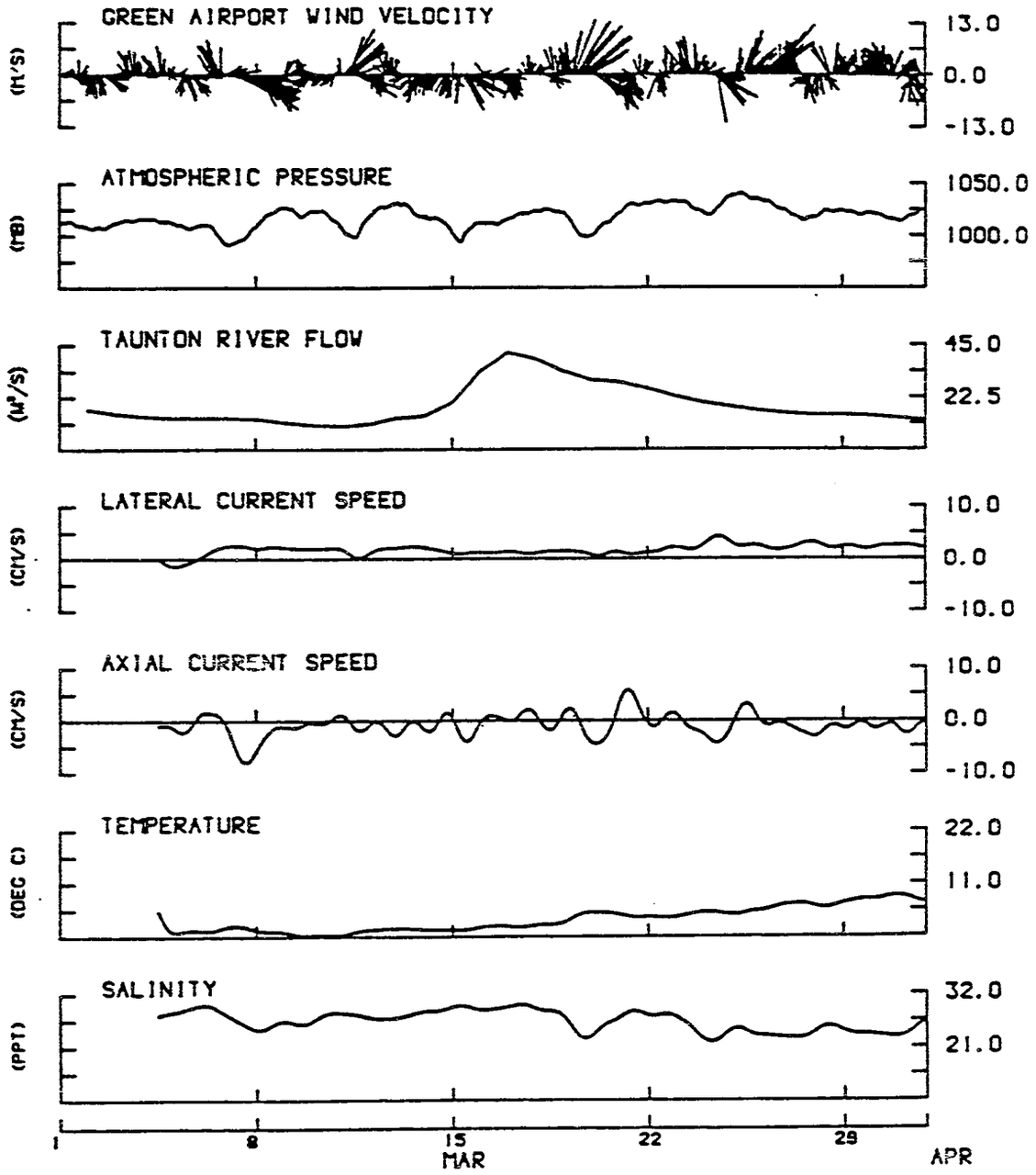

Figure 4.3 Low-passed (30 hour) filtered data for deployment 2.011 at Brightman station during March 1986. Compare with Figure 4.2.

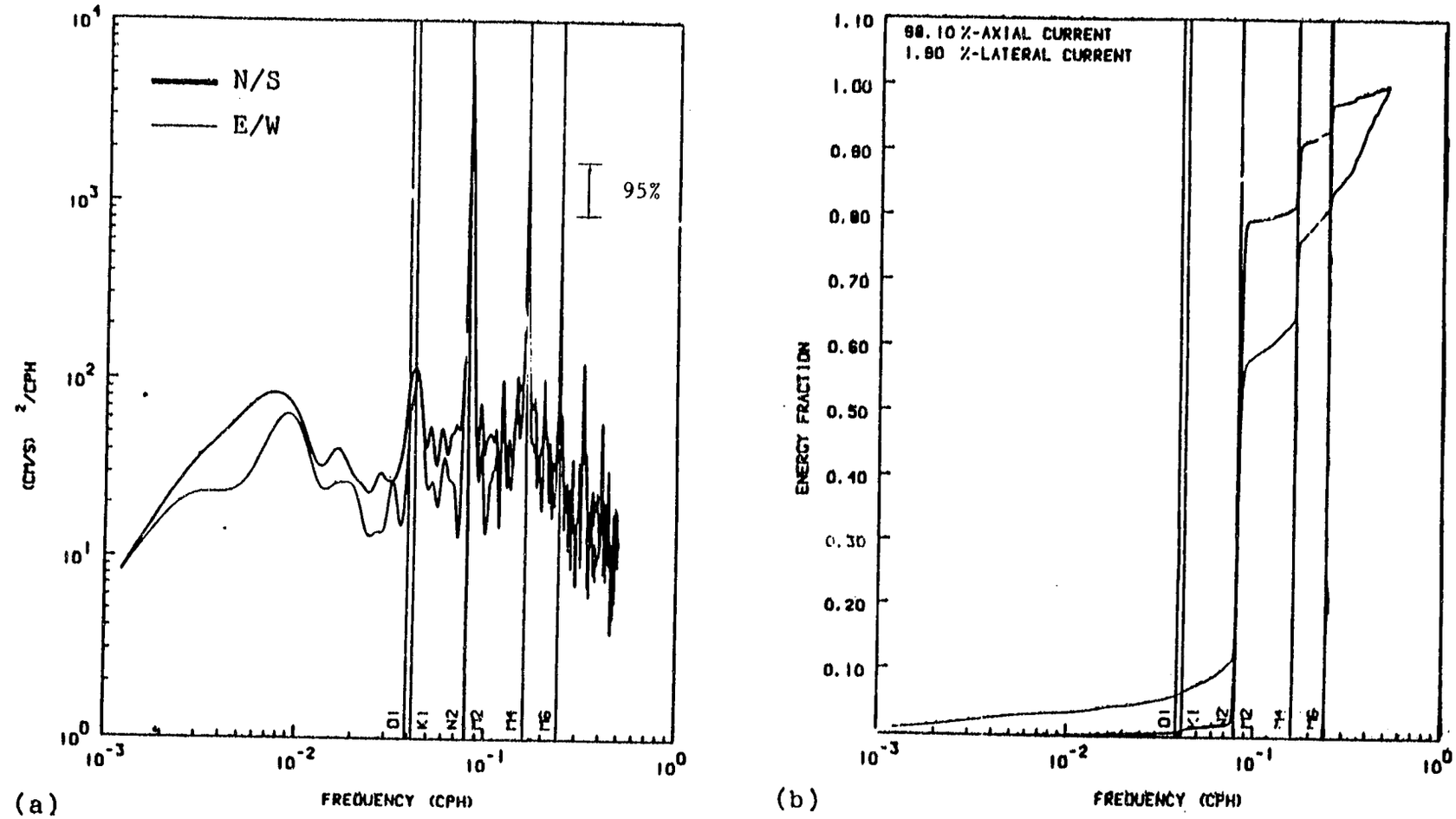

Figure 4.4 Power spectra of currents measured at the Brightman surface station during deployment 2.011: (a) energy at each frequency; (b) cumulative energy.

contribution comes from the tidal components, with the M_2 tide being responsible for about 70%. If we assume that all the low-frequency energy comes from the wind, this contribution is only two percent of the total.

Figure 4.4 may be compared with current spectra measured at other points in Narragansett Bay. Figure 4.5 shows similar current spectra for the Providence River and Gaspee Point from Turner (1984). As with the Brightman data, the M_2 tidal component accounts for about 75% of total energy, and only a few percent is due to the wind. Turner reports that low frequency events account for only 8 to 25 percent of total energy for his experiments.

Strikingly different are the current spectra in Figure 4.6, taken by Weisberg (1974) at a point in open water in upper Narragansett Bay near the mouth of the Providence River. Low frequencies contribute 45% of the total energy, which Weisberg attributes almost entirely to wind forcing. The effect of wind is so strong at this open-water location that Weisberg was able to develop a statistical transfer function to compute low-frequency currents with good accuracy from knowledge of local winds. Turner (1984) developed a similar transfer function for the Providence River data of Figure 4.5, but the accuracy was only fair for four of his six deployments and poor for the other two.

The partitioning of current energy among low, tidal, and high frequencies are listed in Table 4.5 for all of the 21 meter deployments of the present study. The average of these values may be summarized as follows:

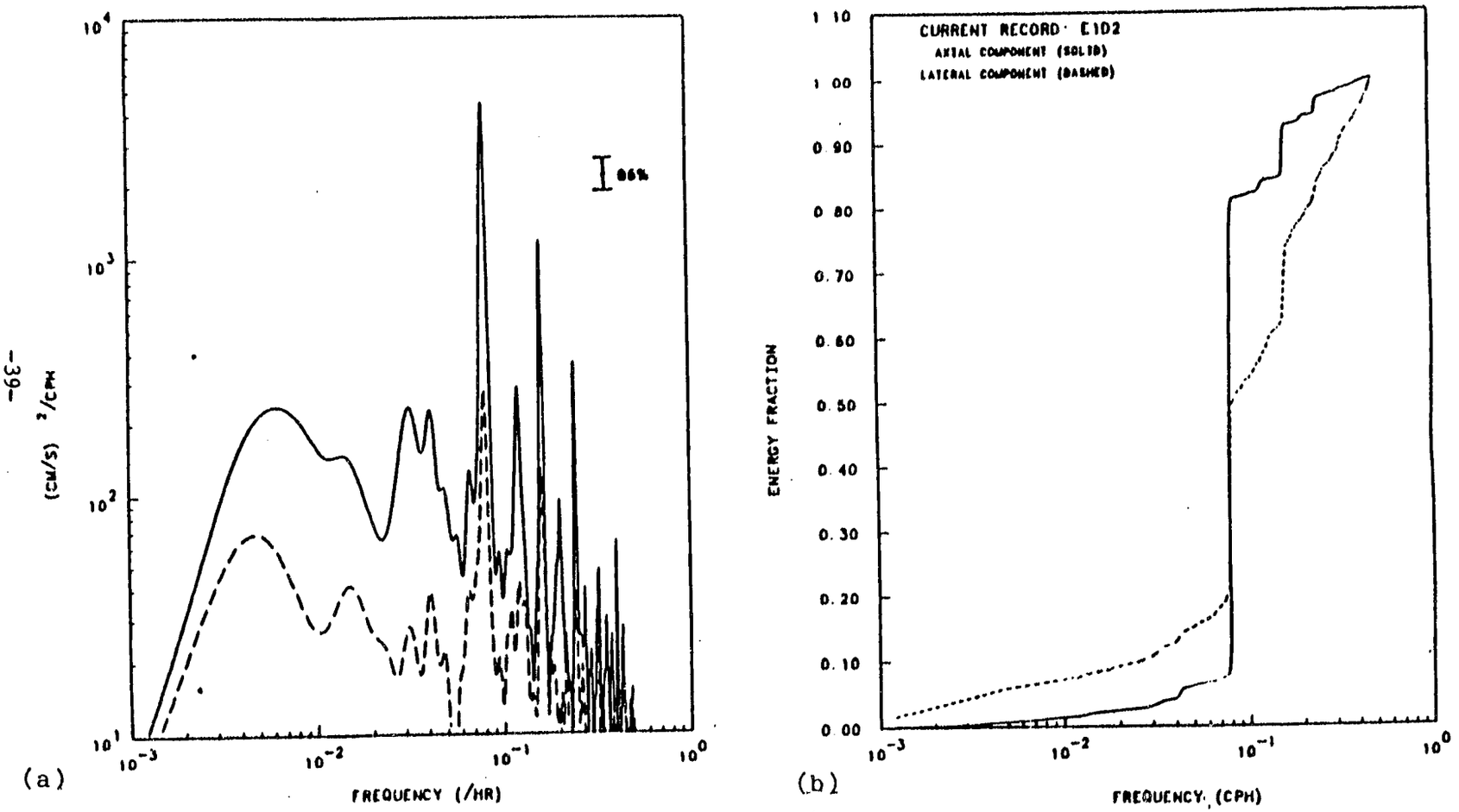

Figure 4.5 Intensive (a) and cumulative (b) spectra of currents in the Providence River measured by Turner (1984). Compare with Figure 4.4.

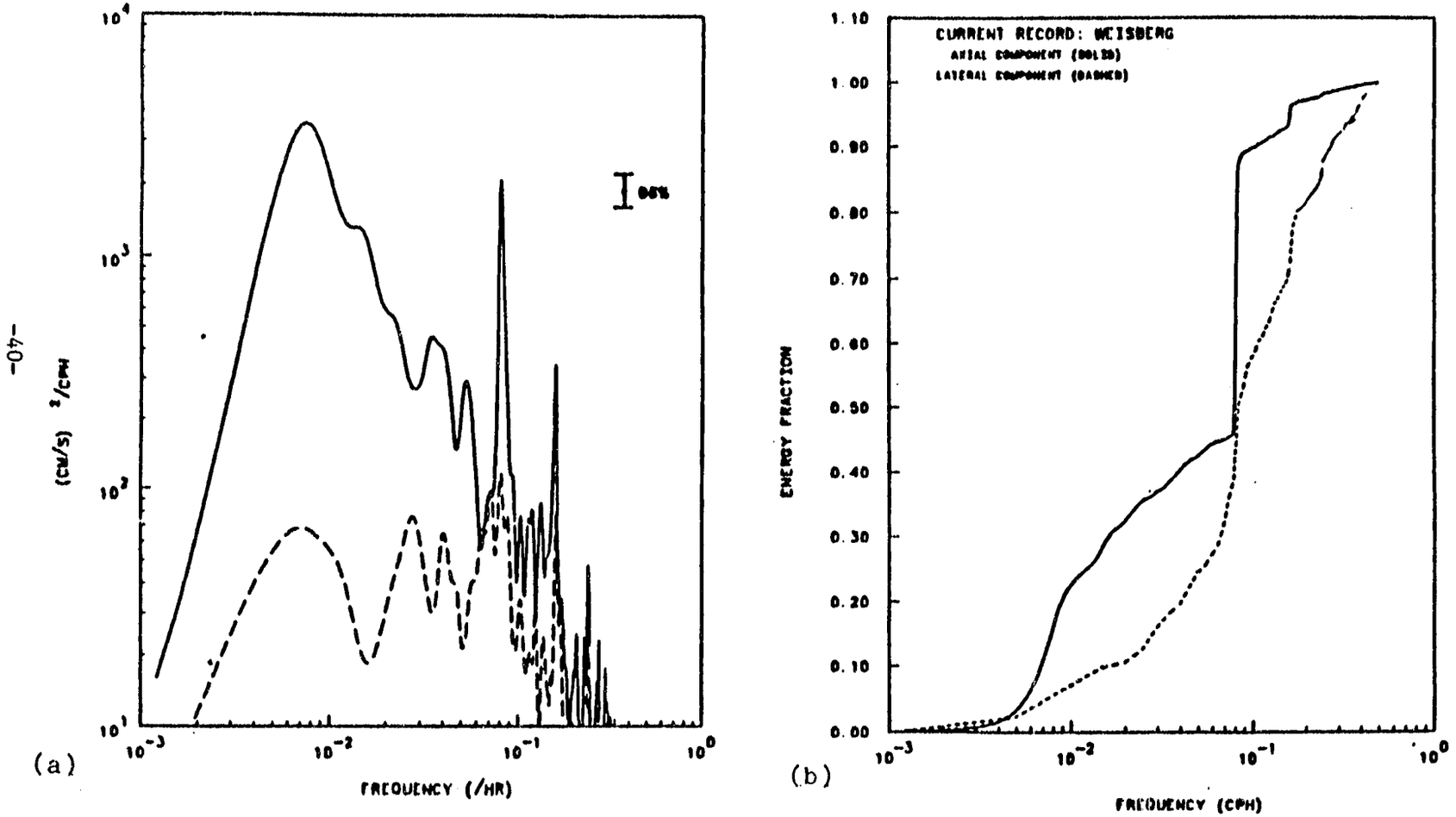

Figure 4.6 Intensive (a) and cumulative (b) spectra of currents at an open-water point in upper Narragansett Bay measured by Weisberg (1974).

Table 4.5

Partitioning of Current Meter Energies

Location and Deployment		Percent of Total Energy — Low Frequency	Tidal Frequency	High Frequency
Near Brightman:				
1.011	bottom	3 %	92 %	5 %
1.229	surface	2 %	96 %	2 %
2.011	surface	2 %	96 %	2 %
2.229	bottom	5 %	88 %	7 %
3.011	surface	2 %	96 %	2 %
3.186	bottom	5 %	87 %	8 %
4.186	bottom	2 %	93 %	5 %
Near Mt. Hope Bridge:				
1.027	surface	9 %	86 %	5 %
1.029	mid-depth	6 %	89 %	5 %
2.027	surface	7 %	89 %	4 %
2.029	mid-depth	8 %	87 %	5 %
3.027	mid-depth	3 %	92 %	5 %
3.029	surface	8 %	87 %	5 %
4.027	mid-depth	7 %	83 %	10 %
5.011	surface	6 %	89 %	5 %
5.029	bottom	7 %	77 %	16 %
5.027	surface	5 %	92 %	3 %
5.186	bottom	5 %	90 %	5 %
Near Sakonnet:				
1.186	mid-depth	19 %	60 %	21 %
2.186	mid-depth	27 %	54 %	19 %
3.229	mid-depth	24 %	59 %	17 %

Location	Frequencies: Low	Tidal	High
Brightman:	3%	93%	4%
Mt. Hope:	7%	87%	6%
Sakonnet:	23%	58%	19%

Clearly the tides are dominant at Brightman and Mt. Hope but less so at Sakonnet, as noted earlier in Section 4.1. Recall that tidal velocity magnitudes at Sakonnet are only one-quarter to one-third of the Brightman and Mt. Hope values. The lack of tidal activity at Sakonnet makes the low and high frequency currents appear more significant when they are really quite small in magnitude.

Appendix C shows the complete set of current power spectra charts developed for all deployments and meters used in this study.

4.2.2 Frequency Domain Analysis of Data

Following the examples of Weisberg (1974) and Turner (1984), we may attempt a statistical correlation between the winds and the present current meter data. Section 4.2.1 has discussed the individual power spectra of the winds and currents separately. To relate the two, we compute the multiple coherence function between wind and current. As a measure of wind input we take the wind stresses on the surface. If u and v denote orthogonal wind components, we assume that the wind stress in the u direction is proportional to $u(u^2+v^2)^{1/2}$, following Officer (1976). The

two orthogonal directions were selected to be axial and lateral to the main channel where the current meter was located.

The time series of wind stresses were computed and multiplied by the respective water current components at two hourly intervals and time-averaged to give multiple coherence functions. Continuing our use of deployment 2.011 as an example, Figure 4.7 shows the multiple coherences at the Brightman surface-meter station, computed from the data of Figure 4.2. Coherences are low everywhere, with a moderate peak at the diurnal frequency (0.042 cycles/hr) possibly attributable to the sea-breeze. The coherence scales range from zero to unity and represent the fraction of current energy which may be attributed to direct wind input at that frequency. The dashed line mark "95%" represents the level below which a 95% probability exists that there is zero coherence between the wind and the current.

Restricting ourselves in Figure 4.7 to the frequency range 0.002 to 0.03 cycles/hr where wind energy is strongest (Turner 1984), we see that this record shows very low coherence between wind and current. Recalling from Figure 4.4 that the current energy in this range is quite small, we conclude that the direct contribution of wind to the currents for this deployment is truly small.

Other current-meter records taken during this study show more coherence between wind and water velocity. Table 4.6 summarizes the peak coherences found in the wind-frequency ranges for the seven Brightman and eleven Mt. Hope meter records. There is considerable variability so that it is difficult even to conclude whether the surface or the bottom is more responsive to the wind.

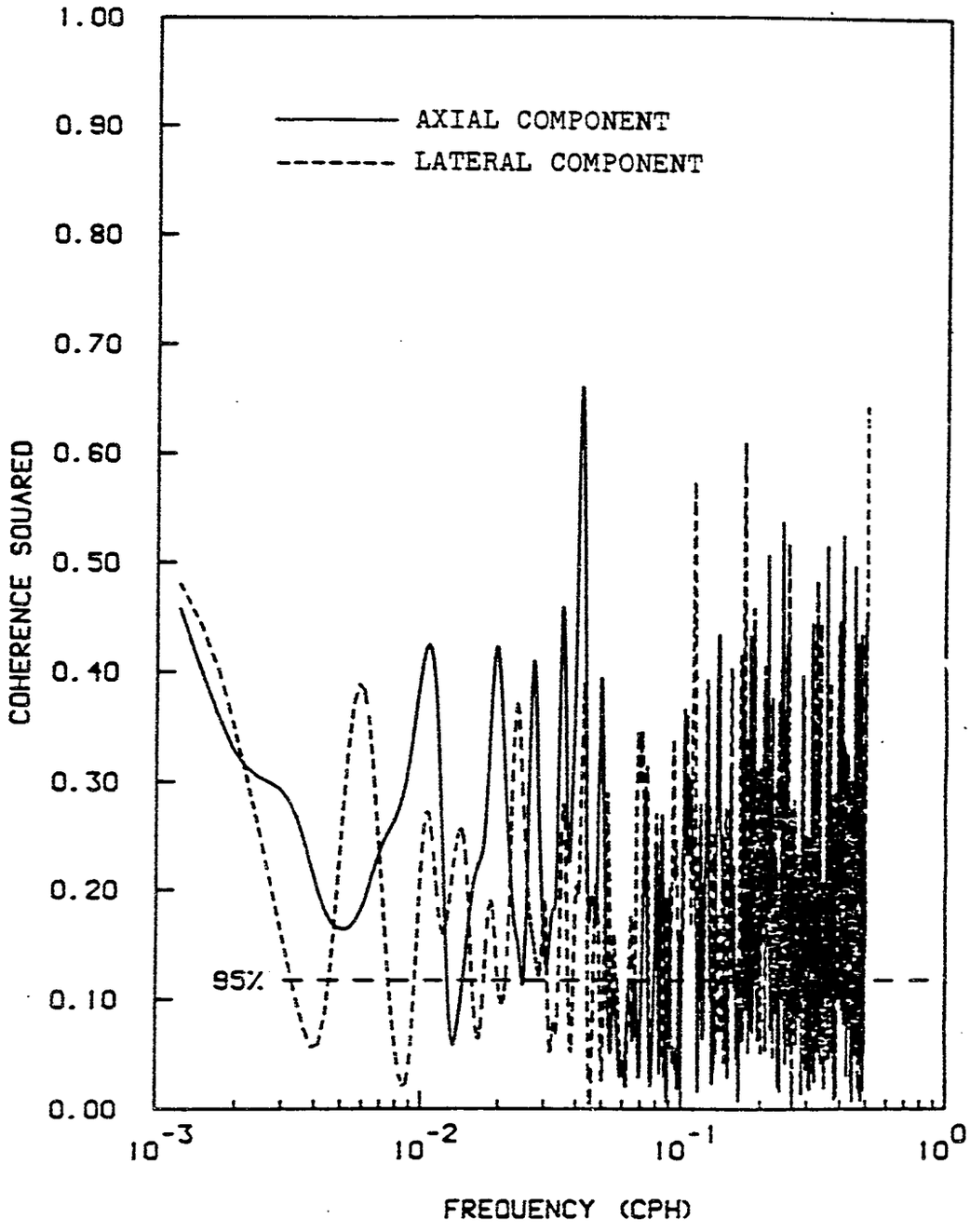

Figure 4.7 The computed multiple coherence between wind stress and current velocity components at the Brightman surface station during deployment 2.011.

Table 4.6 Peak Low-Frequency Coherence Between the Wind and Local Current Components

Location and Deployment		Peak Coherence	
		Axial	Lateral
Brightman:			
1.011	bottom	0.91	0.61
1.229	surface	0.77	0.72
2.011	surface	0.43	0.38
2.229	bottom	0.83	0.64
3.011	surface	0.66	0.51
3.186	bottom	0.65	0.48
4.186	bottom	0.33	0.45
	Averages:	0.65	0.54
Mt. Hope:			
1.027	surface	0.67	0.71
1.029	mid-depth	0.68	0.72
2.027	surface	0.60	0.66
2.029	mid-depth	0.68	0.47
3.027	mid-depth	0.76	0.80
3.029	surface	0.89	0.86
4.027	mid-depth	0.71	0.35
5.011	surface	0.60	0.75
5.029	bottom	0.36	0.45
5.027	surface	0.85	0.59
5.186	bottom	0.68	0.42
	Averages:	0.68	0.62

The peaks measured and tabulated in Table 4.6 average to about 60% coherence. this is low compared to the data of Turner (1984) in the Providence River, where peak coherences at low frequency were about 80%. Even higher coherences exceeding 90% were reported by Weisberg (1974) for upper Narragansett Bay. The low values of coherence and low-frequency current energy in Tables 4.5 and 4.6 lead to the conclusion that the overall effect of wind excitation on Mt. Hope Bay currents is very small. Therefore no wind/current statistical transfer function was attempted for the present Brightman and Mt. Hope data records of this study.

4.3 Density Induced Circulation

4.3.1 Observations of Residual Flow

The current meter records can be filtered over a time scale large compared to dominant tidal periods to yield the residual current at the given station. The cut-off period for the filter was chosen to be 30 hours.

As an example let us examine some current records from the Brightman station in the Taunton River, taken on the side of the ship channel where the water depth is 14 m. Figure 4.8 shows the filtered currents, temperature, and salinity 3 meters from the surface for the period March 4, 1986 to June 9, 1986. One sees considerable variability even at periods greater than 30 hours. The average east-west current is approximately zero, but there is clearly a non-zero southward average current of about 2 cm/s.

The filtered record for the same periods, at 3 meters from the bottom, is shown in Figure 4.9. Here we see an averaged near-zero north/south

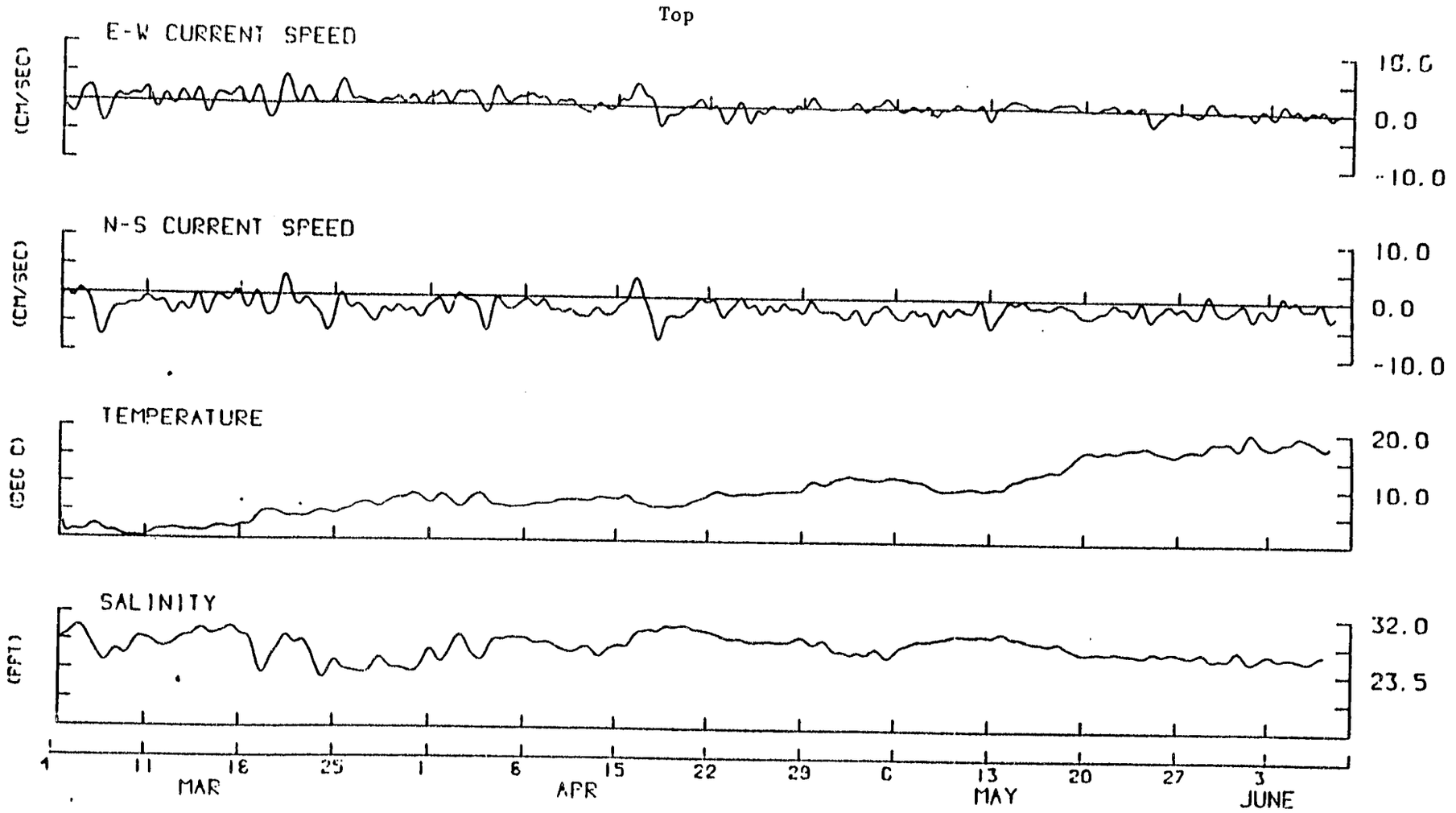

Figure 4.8 Low-passed (30 hour) current, salinity, and temperature records for Brightman station during deployment 2.011.

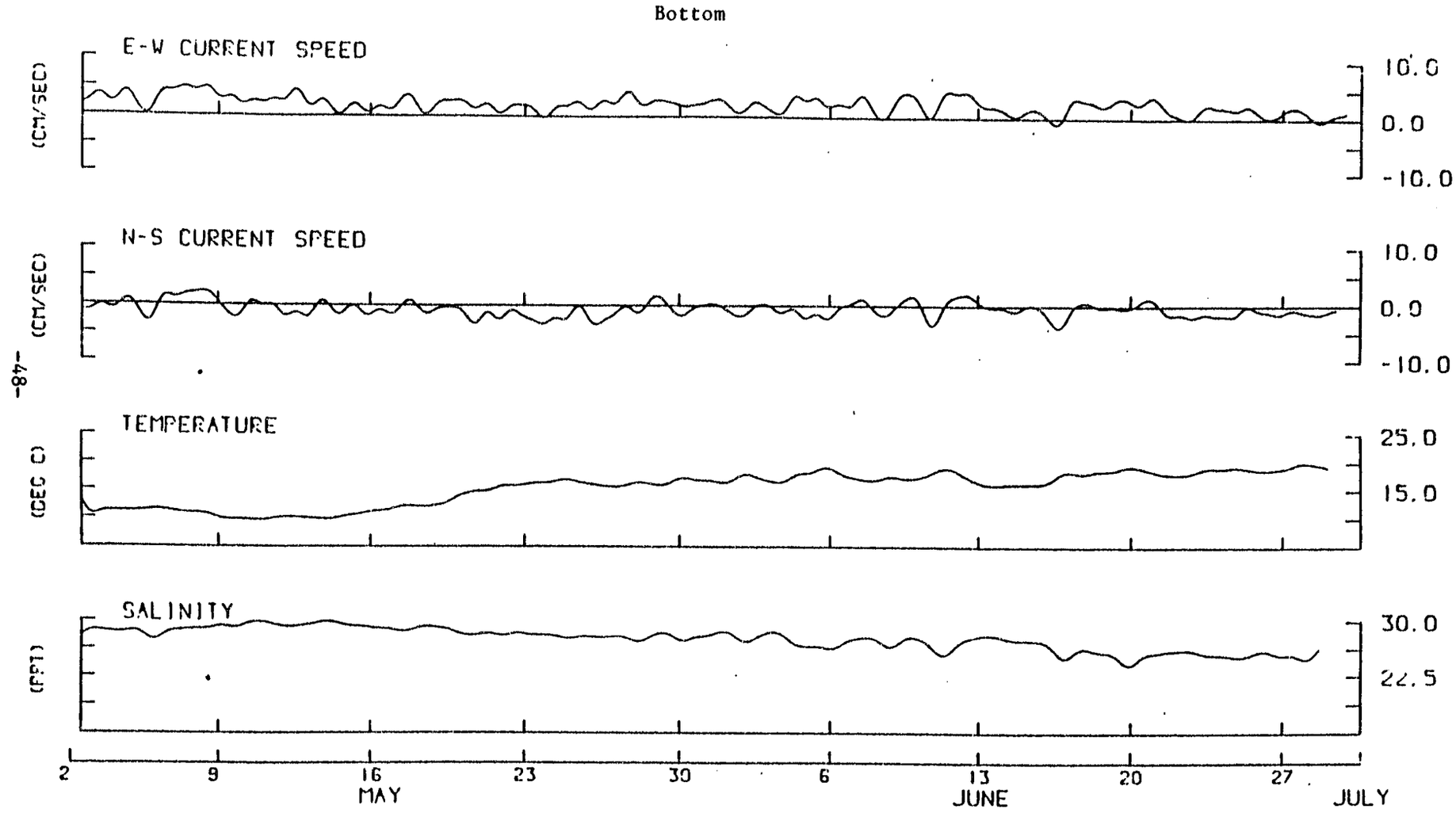

Figure 4.9 Low-passed (30 hour) current, salinity, and temperature records for Brightman station during deployment 3.186.

current but a definitely eastward average speed of 2 cm/s. Since the river is slightly stratified, with surface salinity of 26°/•• and bottom salinity of 28°/•• both these mean currents are consistent with density-driven flows, down-estuary at the surface and up-estuary at the bottom. However, there are other possible contributing causes to residual currents:

1. wind generated flows;
2. transient run-off or river inputs;
3. non-local long term events outside Mt. Hope Bay;
4. topographic effects causing a non-zero mean current at some stations, with zero mean flow in the cross-section.

All of these effects may occur in the Taunton River, but it is thought that density gradients are the primary cause.

The average N/S and E/W current speed for each meter and each deployment were computed and resolved into net mean velocity vectors. The results are listed in Table 4.7. The mean current speeds vary from 1.84 to 13.71 cm/s. The residual velocities are thus significant but not dominating and are comparable to density-driven currents.

The vectors from Table 4.7 can be plotted for visual inspection of each station. Figure 4.10 shows the mean current vectors at the Brightman station in the Taunton River, (a) near the surface, and (b) near the bottom. The axial components of these vectors are consistent with a classic two-layer density-driven flow. Both surface and bottom residual components tend toward the deep center channel of the river, which is probably a topographic effect.

Table 4.7

Mean Current Speed and Direction for each Deployment

Deployment			$\lvert\bar{V}\rvert$ (cm/s)	θ(° clockwise from true north)
BRIGHT	1.011	bottom	2.48	74.6
BRIGHT	1.229	surface	3.81	184.2
SAKON	1.186	mid	3.85	178.8
MTHOPE	1.027	surface	11.09	214.0
MTHOPE	1.029	mid	10.63	205.9
BRIGHT	2.011	surface	1.84	168.4
BRIGHT	2.229	bottom	2.07	81.7
SAKON	2.186	mid	3.33	168.9
MTHOPE	2.027	surface	9.56	205.1
MTHOPE	2.029	mid	8.59	208.1
BRIGHT	3.011	surface	1.86	170.9
BRIGHT	3.186	bottom	2.32	107.3
SAKON	3.229	mid	3.10	181.8
MTHOPE	3.027	mid	10.40	205.7
MTHOPE	3.029	surface	10.89	205.3
BRIGHT	4.186	BAD CURRENT RECORD		
MTHOPE	4.027	mid	11.64	205.4
MTHOPE	5.011	surface	8.76	196.4
MTHOPE	5.029	bottom	13.71	199.1
BFERRY	5.027	surface	4.38	209.1
BFERRY	5.186	bottom	6.62	161.1

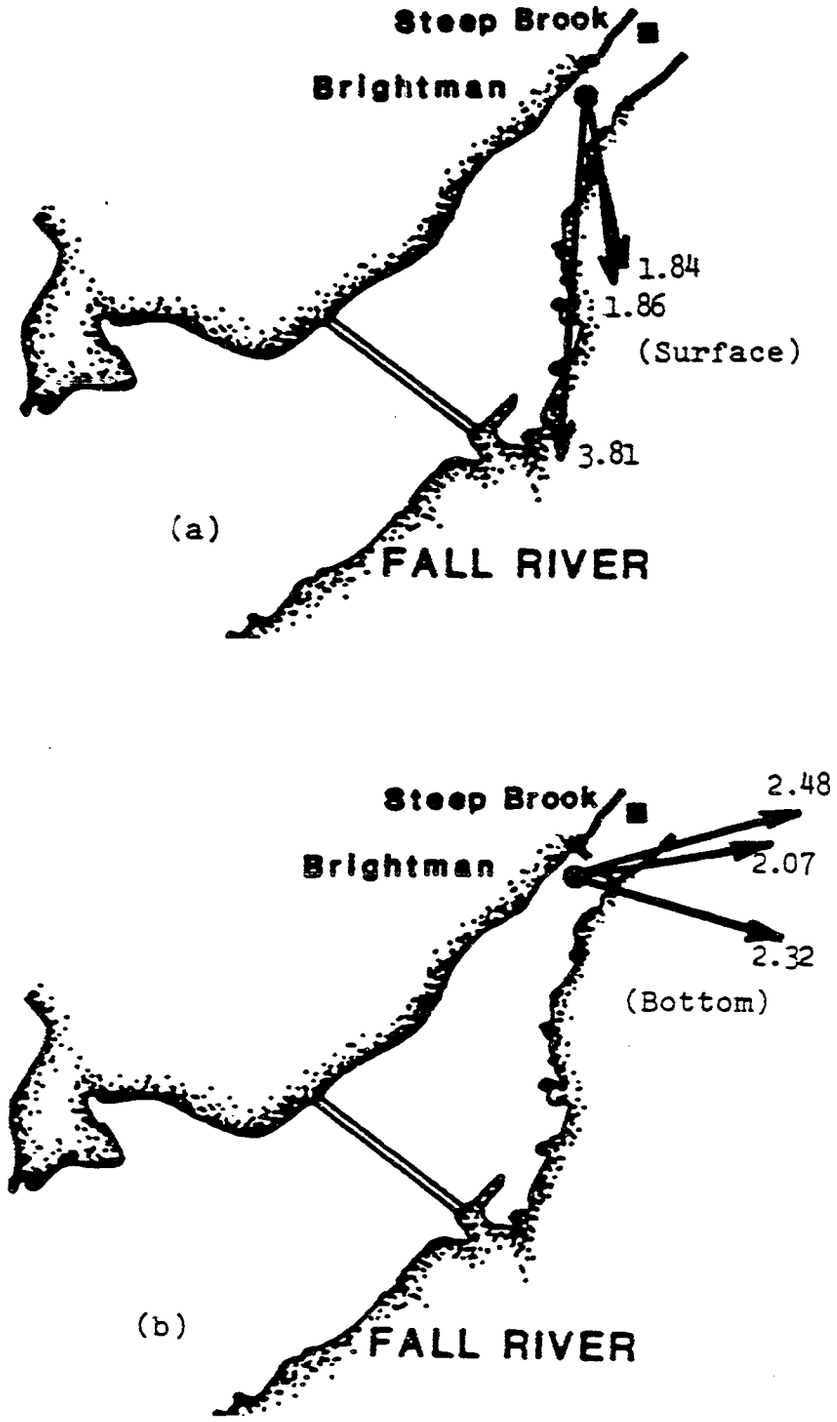

Figure 4.10 Mean residual current vectors (cm/s) for three deployments at the Brightman station.

Figure 4.11 shows residual current vectors at the Mt. Hope and Bristol Ferry stations near the Mt. Hope Bridge, (a) at the surface, and (b) at mid-depth and near the bottom. It is seen that all measured mean flows except possibly the Bristol Ferry bottom, have a strong component out under the bridge into Narragansett Bay. The component velocities of 4 to 14 cm/s are substantial. No residual inflow was measured. Taking the average residual flow to be 10 cm/s, with a flow cross-section under the bridge of approximately 10^4 m^2, these data imply a mean outflow of 1000 m^3/s, or sixty times more than the Taunton River fresh water flow. To carry this implausible conclusion further, since the volume of Mt. Hope Bay is 2.02 x $10^8 m^3$ (Chinman and Nixon, 1985), such a mean flow rate under the Mt. Hope Bridge would empty the entire Bay in 2.3 days. It follows that there must be residual inflow at other (unmeasured) stations near the Mt. Hope Bridge. The present data imply another topographical effect, possibly associated with eddy currents near the bridge structure or eddies caused by the sudden contraction of the land boundaries.

Figure 4.12 shows residual current vectors at the Hummocks near the Sakonnet River Bridge. All three meter deployments are at mid-depth and show an outward flow of about 3 cm/s. Since the cross-sectional area near this deployment point is about 5000 m^2, these measurements imply an outward mean flow of 150 m^3/s from Mt. Hope Bay into the Sakonnet River, or eight times greater than the Taunton River flow. Like the Mt. Hope Bridge result above, these flow rates are highly implausible and there must be points of inflow elsewhere along these boundary cross-sections. Without further long term current measurements across these sections, it is difficult to conclude anything about the spatial distribution of boundary residual

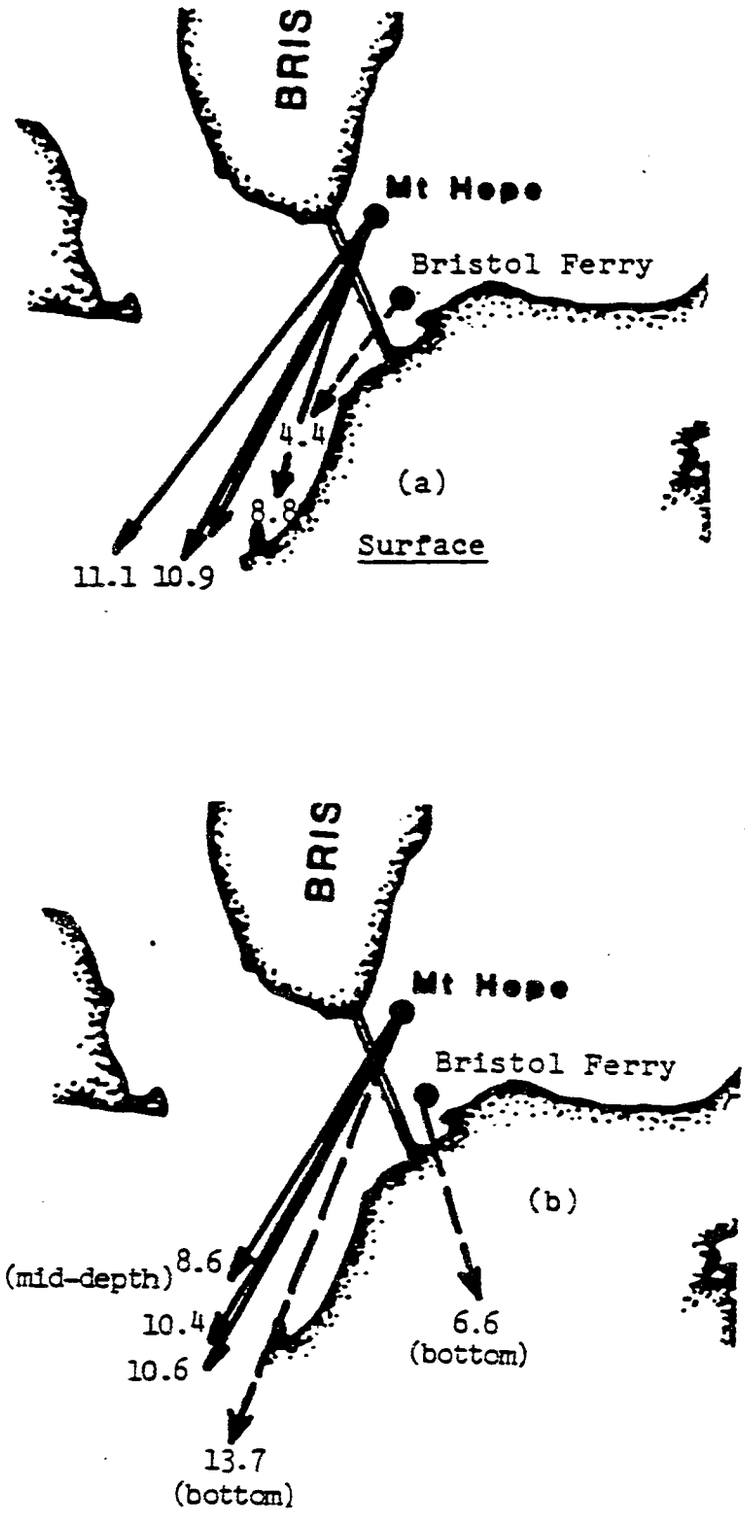

Figure 4.11 Mean residual current vectors (cm/s) for four deployments near the Mt. Hope Bridge.

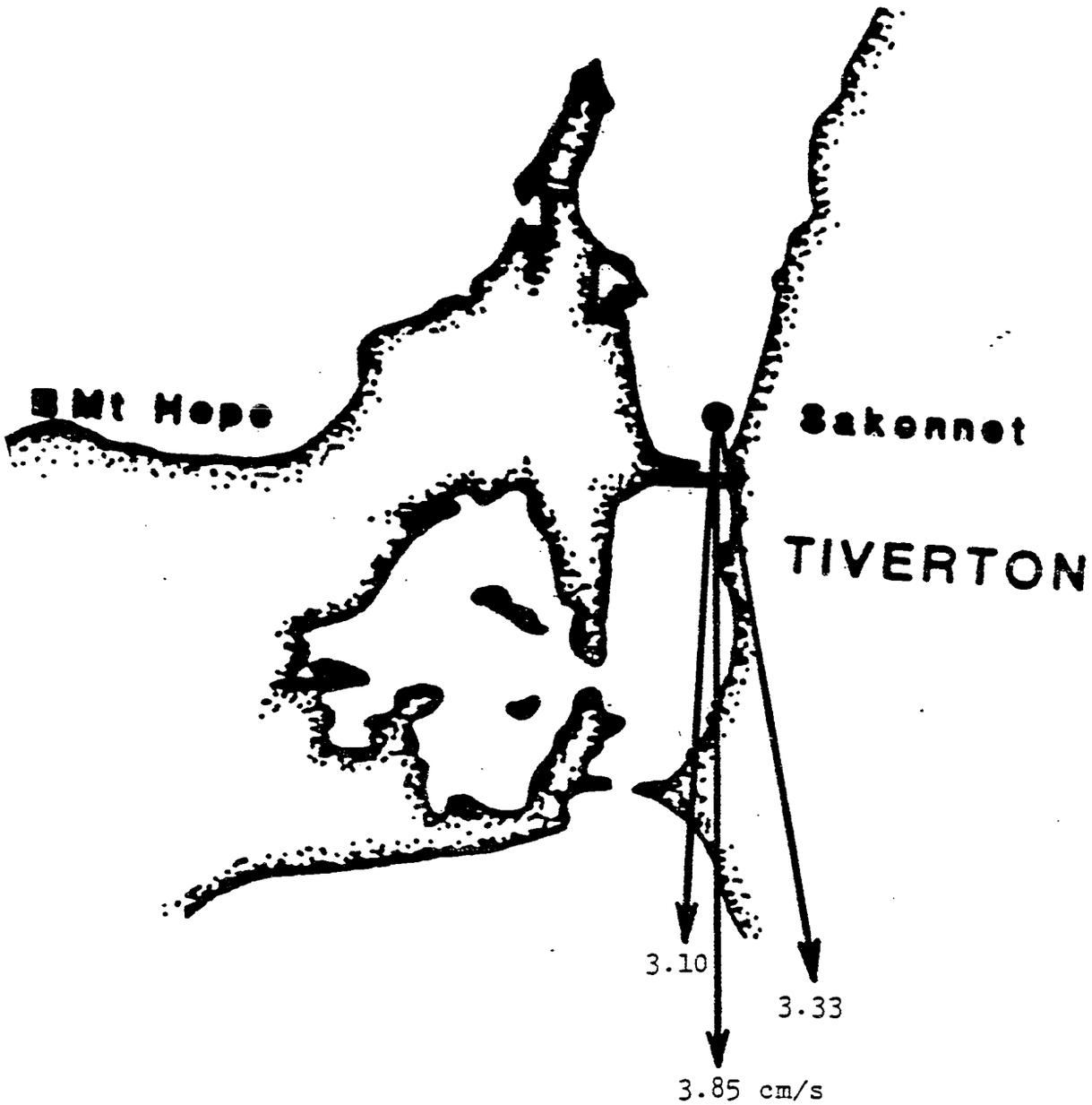

Figure 4.12 Mean residual current vectors (cm/s) for three deployments at mid-depth in the Sakonnet River near the Hummocks.

flows. Meanwhile, the Brightman measurements (Figure 4.10) do make a reasonable balance between net residual flows and the Taunton River flow rate.

4.3.2 Progressive Vector Plots

The tabulated time-mean residual current vectors and the sketches in Section 4.3.1 are oversimplified in that they give no indication of the possible variability of mean flows. A technique used to visualize residual flow variability is call the progressive vector plot, used in the thesis by Turner (1984). One takes the raw data for u (east/west) and v (north/south) and multiplies by the time interval of 5 minutes (300 s) to establish a pseudo-displacement of a particle passing through the meter in that interval. These positions are accumulated in the progressive vector plot to give a picture of overall integration motions associated with that meter position. Since these positions are for varying times at a single measurement point, they of course do not represent actual Lagrangian motions or pathlines of real particles. They illustrate residual motions at a point and they may or may not be highly variable.

Figure 4.13 shows progressive vector plots for four meter deployments near the surface at the Mt. Hope station, ranging in length from 18 to 97 days. The starting points are separated by 100 kilometers for clarity. All the raw data at 5-minute intervals was used to construct these plots, yet the displacement lines show almost no variability and proceed in nearly a straight line. Tidal excursions are essentially eliminated by these computations when plotted on these 100-kilometer scales. We conclude that the residual flow at this point is nearly constant, at rates from 9 to 11

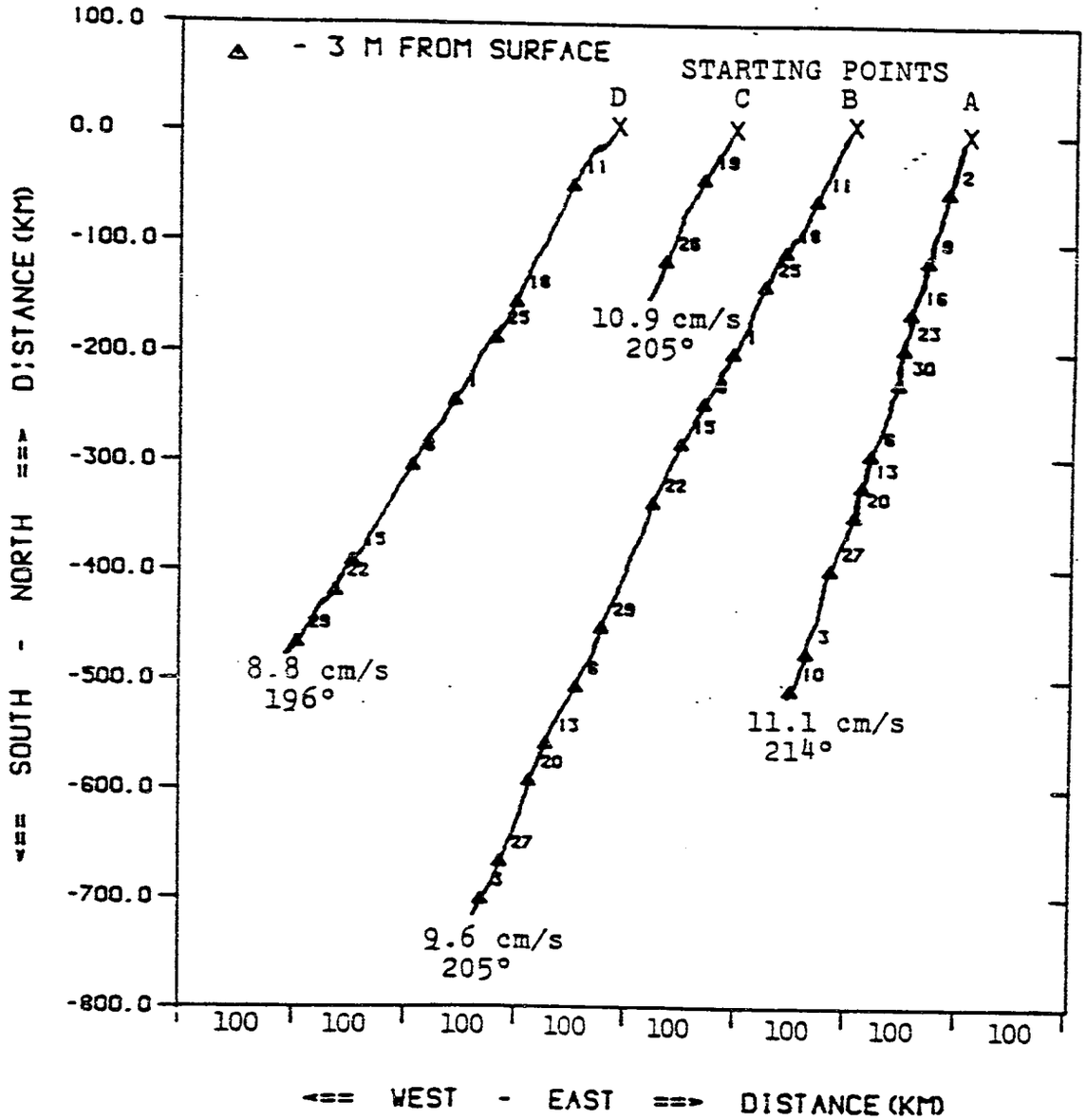

Figure 4.13 Progressive vector plots for four deployments near the surface of Mt. Hope station: (a) 1.027; (b) 2.027; (c) 3.029; (d) 5.011. For clarity, starting points are separated by 100 kilometers.

cm/s and a direction of about 205° clockwise from true north. Compare these progressive vector plots with the mean vectors shown in Figure 4.11.

Progressive vector plots at mid-depth for the Mt. Hope station are shown in Figure 4.14. The results are remarkably similar to the surface plots in Figure 4.13, although three different meters were used and their positions interchanged once. Again the displacements are relentlessly uniform, with little tidal excursion or direction change. The average residual flow is 10 cm/s at an angle of 206°.

Figure 4.15 shows the vector plots at surface and bottom during the 5th deployment at Bristol Ferry. Compare these displacements with the vectors in Figure 4.11. Apparently residual flows are less on the southeast side of the ship channel near the Mt. Hope Bridge.

Progressive vector plots for the Sakonnet station given in Figure 4.16 may be compared with the mean flow vectors from Figure 4.12. Curve B (deployment 2.186) shows some variability but generally the residual flow is south and into the Sakonnet River. Flow rates are less, averaging 3.4 cm/s, and the average direction is 177°. General flow activity is less at Sakonnet than at Mt. Hope or Brightman, as was pointed out in the discussion of tidal currents in Section 4.1.

Figure 4.17 shows vectors for three deployments near the surface at the Brightman station in the Taunton River. Here the river the tidal velocities are higher and not necessarily in the same direction as the main currents, so the tidal excursions are visible in the displacement plots. But the residual motion is still fairly uniform and toward the south, that is, down-estuary and into the center of the ship channel. Compare these progressive vectors with the mean velocity vectors in Figure 4.10(a). The

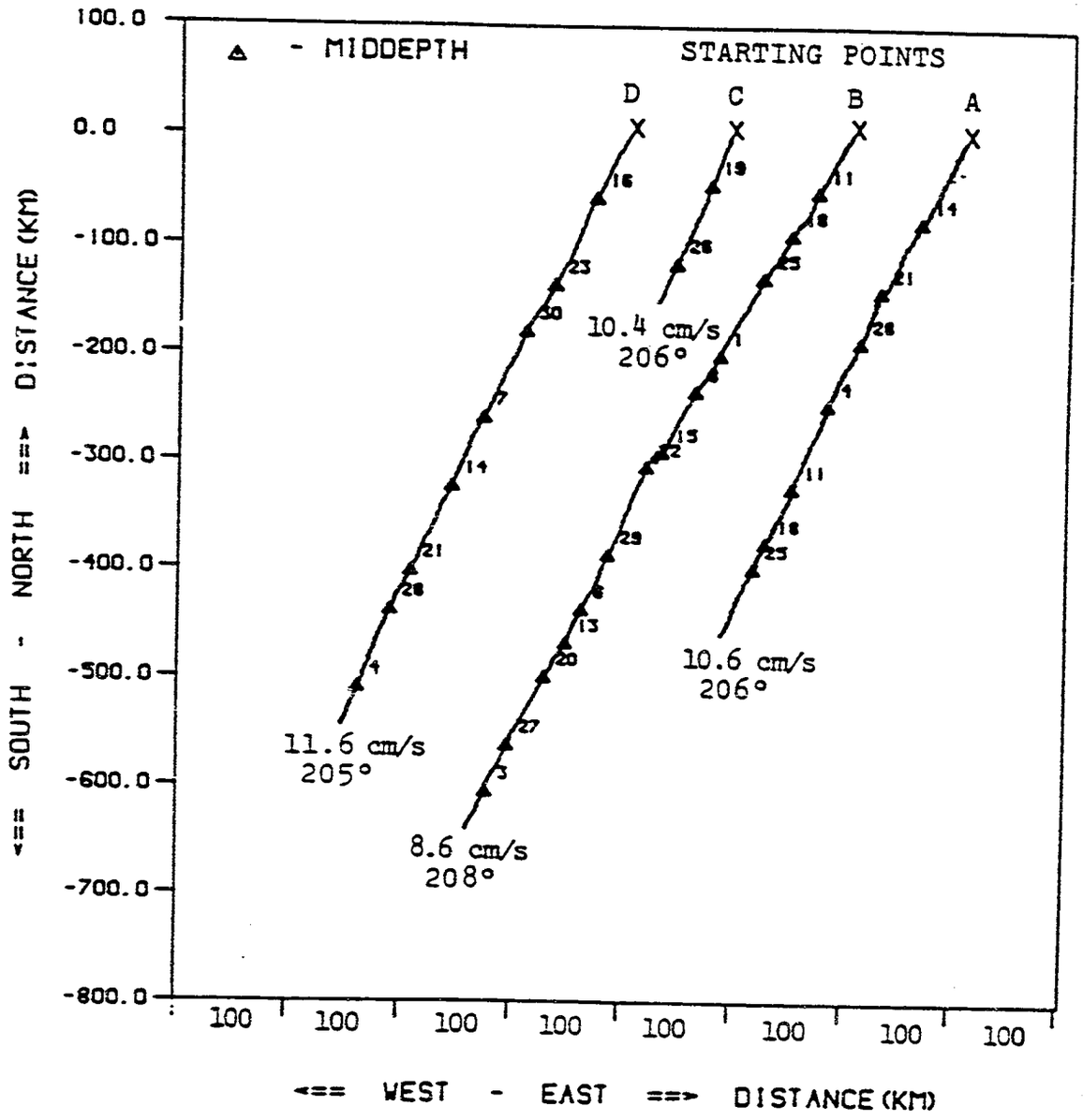

Figure 4.14 Progressive vector plots for four deployments at mid-depth at the Mt. Hope station: (a) 1.029; (b) 2.029; (c) 3.027; (d) 4.027. For clarity, starting points are separated by 100 kilometers.

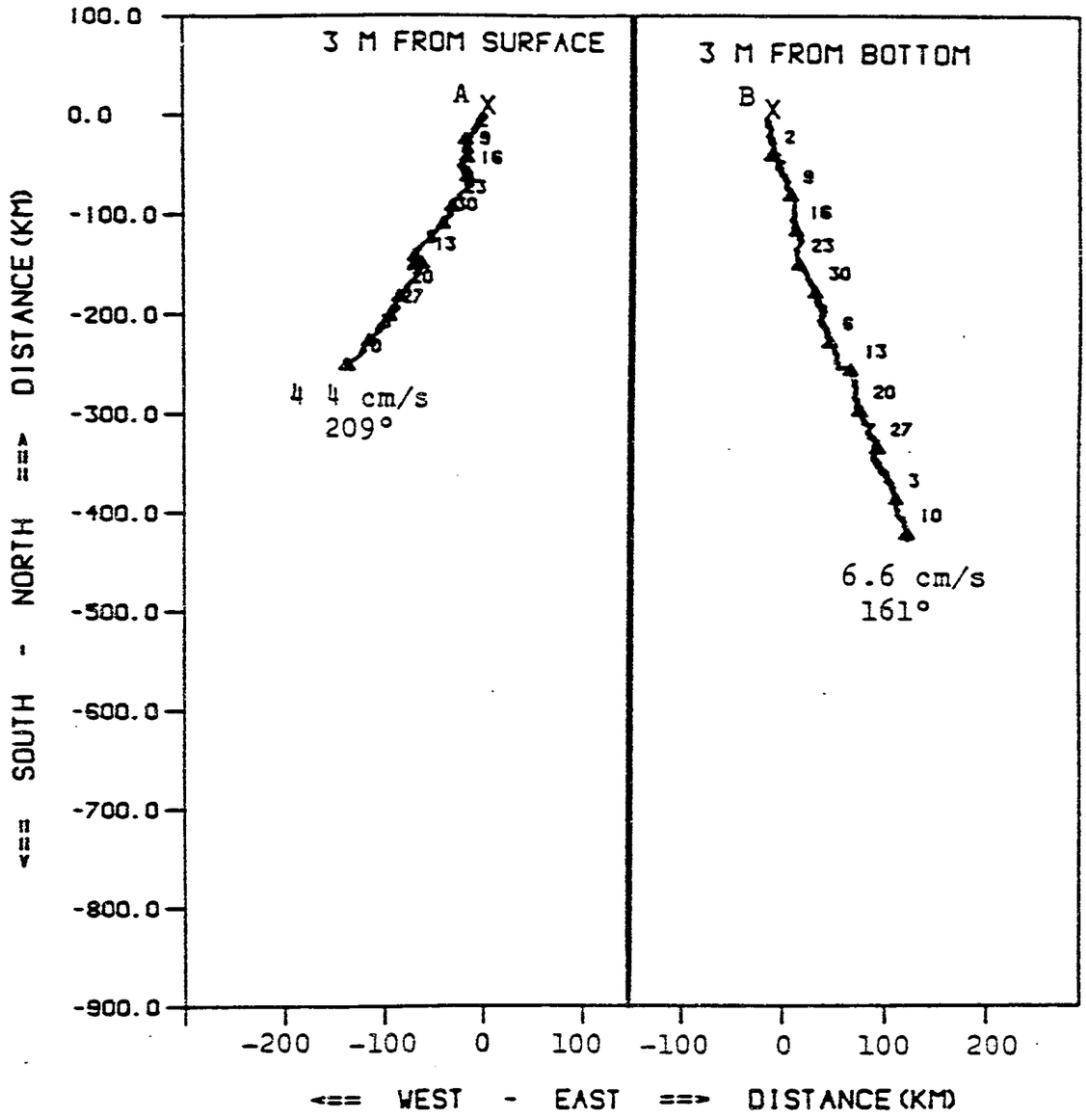

Figure 4.15 Progressive vector plots at the Bristol Ferry station near Mt. Hope Bridge: (a) deployment 5.027; (b) deployment 5.186. Data points (triangles) are shown at weekly intervals.

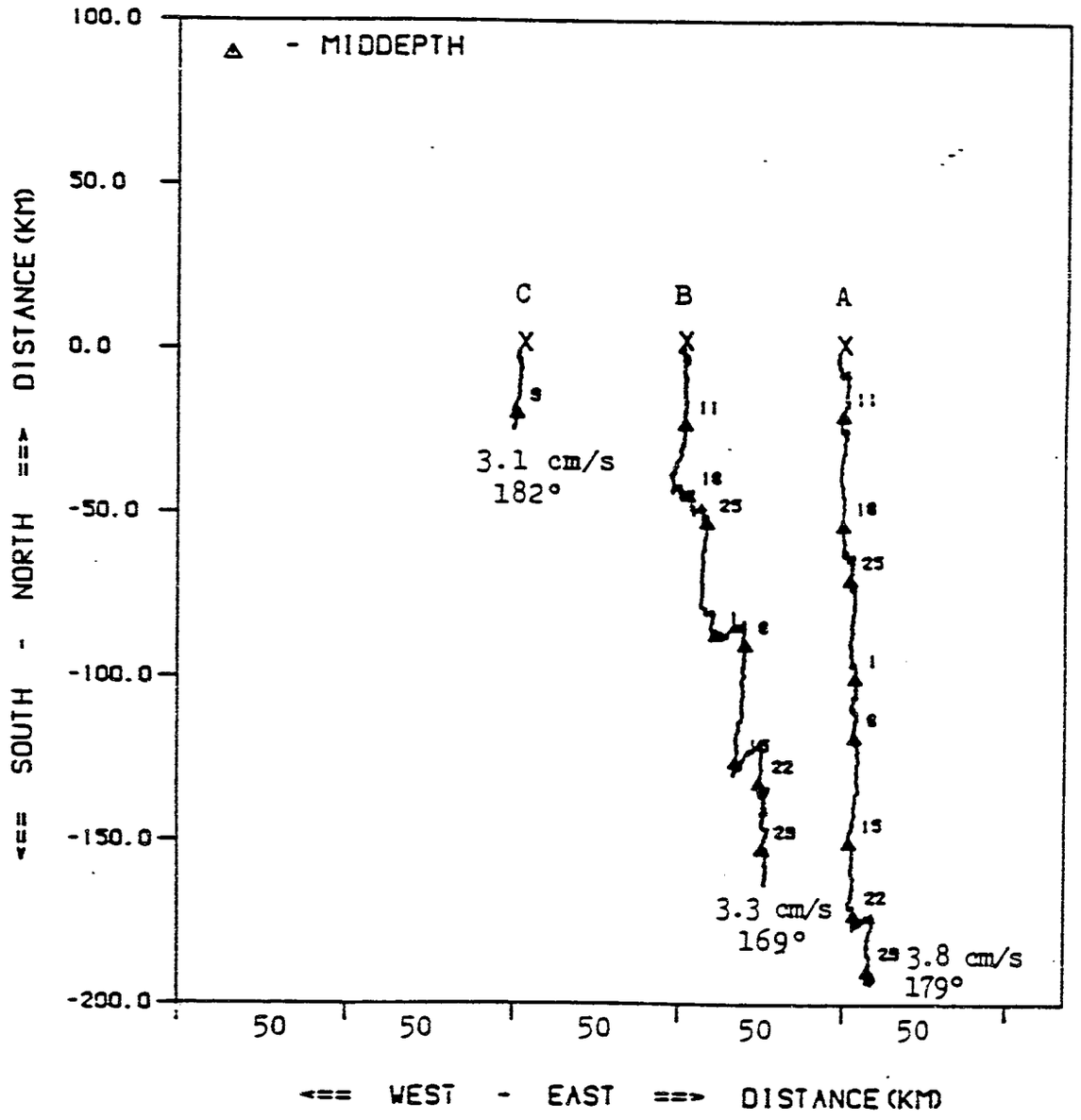

Figure 4.16 Progressive vector plots for three deployments at mid-depth at the Sakonnet station: (a) 1.186; (b) 2.186; (c) 3.229. For clarity, starting points are displaced by 50 kilometers. Data points (triangles) shown at weekly intervals.

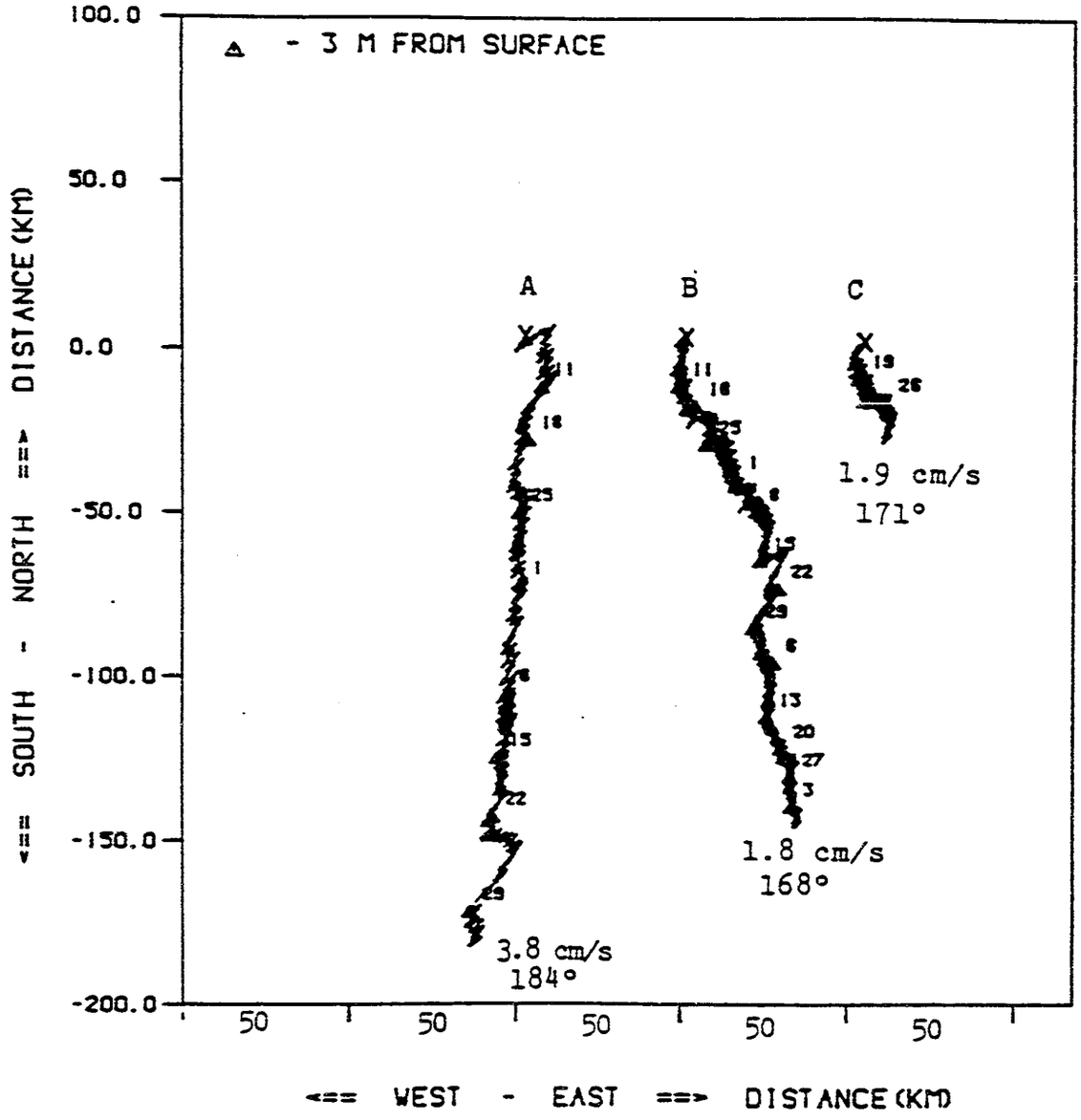

Figure 4.17 Progressive vector plots for three deployments near the surface at the Brightman station: (a) 1.229; (b) 2.001; (c) 3.011. For clarity, starting points are displaced by 50 kilometers. Data points (triangles) shown at weekly intervals.

mean residual surface speed of 2.5 cm/s is consistent with a density-driven circulation.

Progressive vector plots of the bottom flow at the Brightman station are given in Figure 4.18. Like the surface flows, the displacements are fairly uniform but show some tidal excursions. The average residual speed of 2.3 cm/s is consistent with a density-driven flow up-estuary and toward the center of the ship channel. Compare these progressive vectors with the mean velocities in Figure 4.10(b).

4.3.3 Comparison with Density Current Theory

The residual flow measurements at the Brightman station in the Taunton River (Figures 4.10, 4.17, and 4.18) support the concept of a two-layer density current driven by salinity variations in the river.

Figure 4.19 shows the temperature, density, and salinity structure at the Brightman station measured during a short-term field study on May 20, 1986. From surface to bottom, the temperature difference is 5.1°C, the salinity change is 3.3 °/••, and the density difference is 3.7 mg/cm^3. On that particular day the residual currents were about 3 cm/s down-estuary at the surface (Table 4.7) and 4 cm/s up-estuary at the bottom (Table 4.7). We may compare these estimates with the classic theory of two-layer flow.

The theory of density currents is covered in several texts on estuaries, such as Officer (1976), Dyer (1973), and McDowell and O'Connor (1977). These theories were combined into a very interesting three-dimensional numerical model of steady density-driven currents in Narragansett Bay by Hess (1974, 1976). Unfortunately, Hess did not include Mt. Hope Bay or the Sakonnet River in his model. For the remainder of the

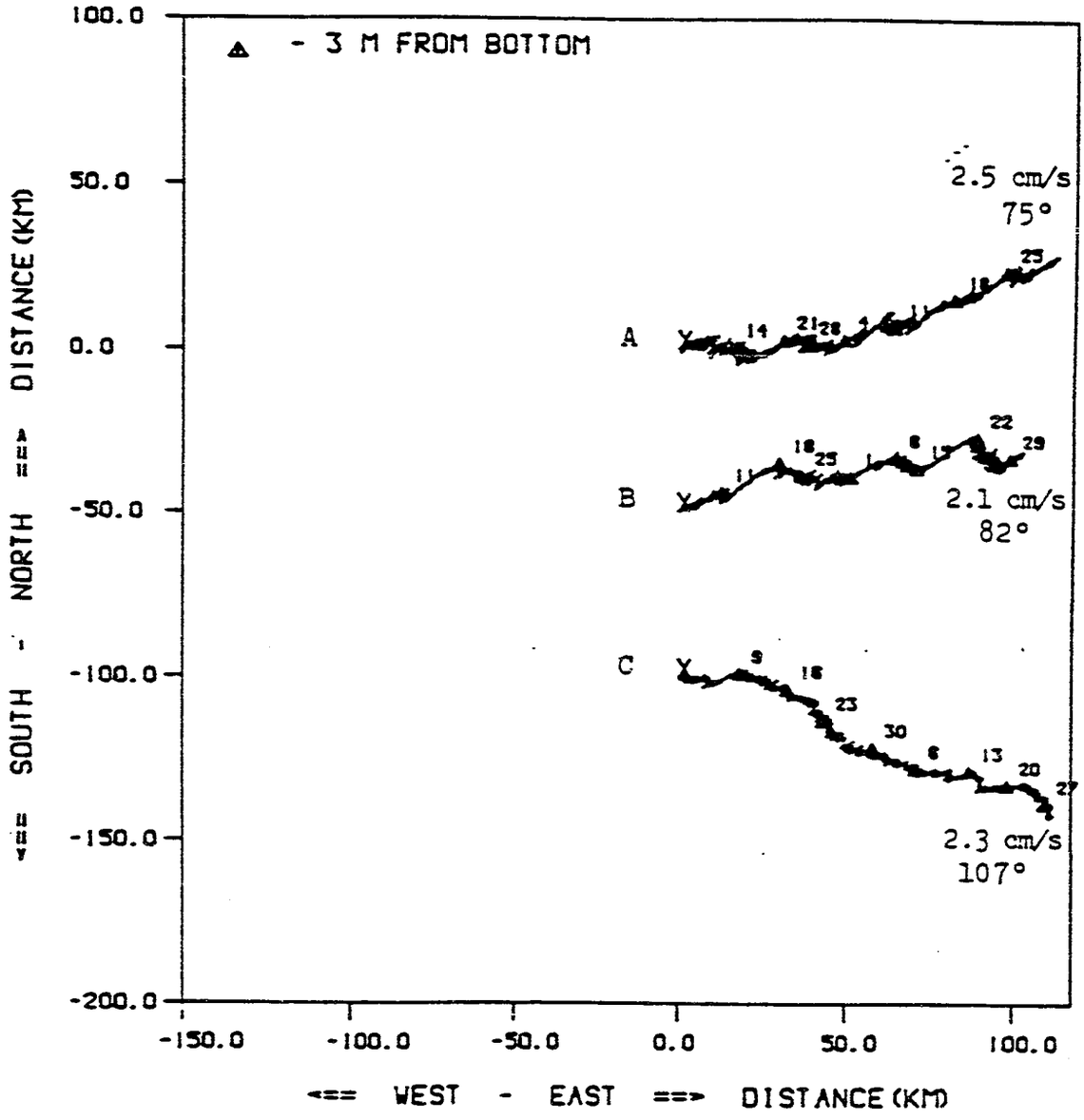

Figure 4.18 Progressive vector plots for three deployments near the bottom at the Brightman station: (a) 1.011; (b) 2.229; (c) 3.186. For clarity, starting points are displaced by 50 kilometers. Data points (triangles) shown at weekly intervals.

Bay, using a grid size of 926 m, Hess computes density currents from 1 to 5 cm/s, with highly variable regions of upwelling and downwelling throughout the bay.

Basically, a density current is caused by a persistent horizontal gradient in water density. In an estuary, such gradients are primarily caused by freshwater river flow mixing with saltwater ocean inputs, with thermal stratification effects being less significant. For example, for the Taunton River data of Figure 4.19, approximately 77% of the total density difference is due to salinity and 23% due to temperature changes.

In a simple two-layer density current with no lateral effects, the dominating long term mean vertical force balance on an element is between the vertical turbulent shear gradient and the horizontal density gradient:

$$\frac{\partial}{\partial z}\left(N_z \frac{\partial u}{\partial z}\right) = \frac{1}{\rho}\frac{\partial p}{\partial x} = \frac{gz}{\rho}\frac{\partial \rho}{\partial x} \qquad (4.1)$$

where N_z is the vertical eddy viscosity, z is vertical downward from the surface, and x is the horizontal direction of the density current u(z). At the bottom, z = h, there is no-slip, u = 0. At the surface, z = 0, in the absence of wind, there is no shear, $\partial u/\partial z = 0$.

With the simplifying assumptions of constant N_z and $\partial\rho/\partial x$, Officer (1976) shows that the solution for u is

$$u = K(1 - 9\eta\nu^2 + 8\eta^3), \quad \eta = z/h \qquad (4.2)$$

where

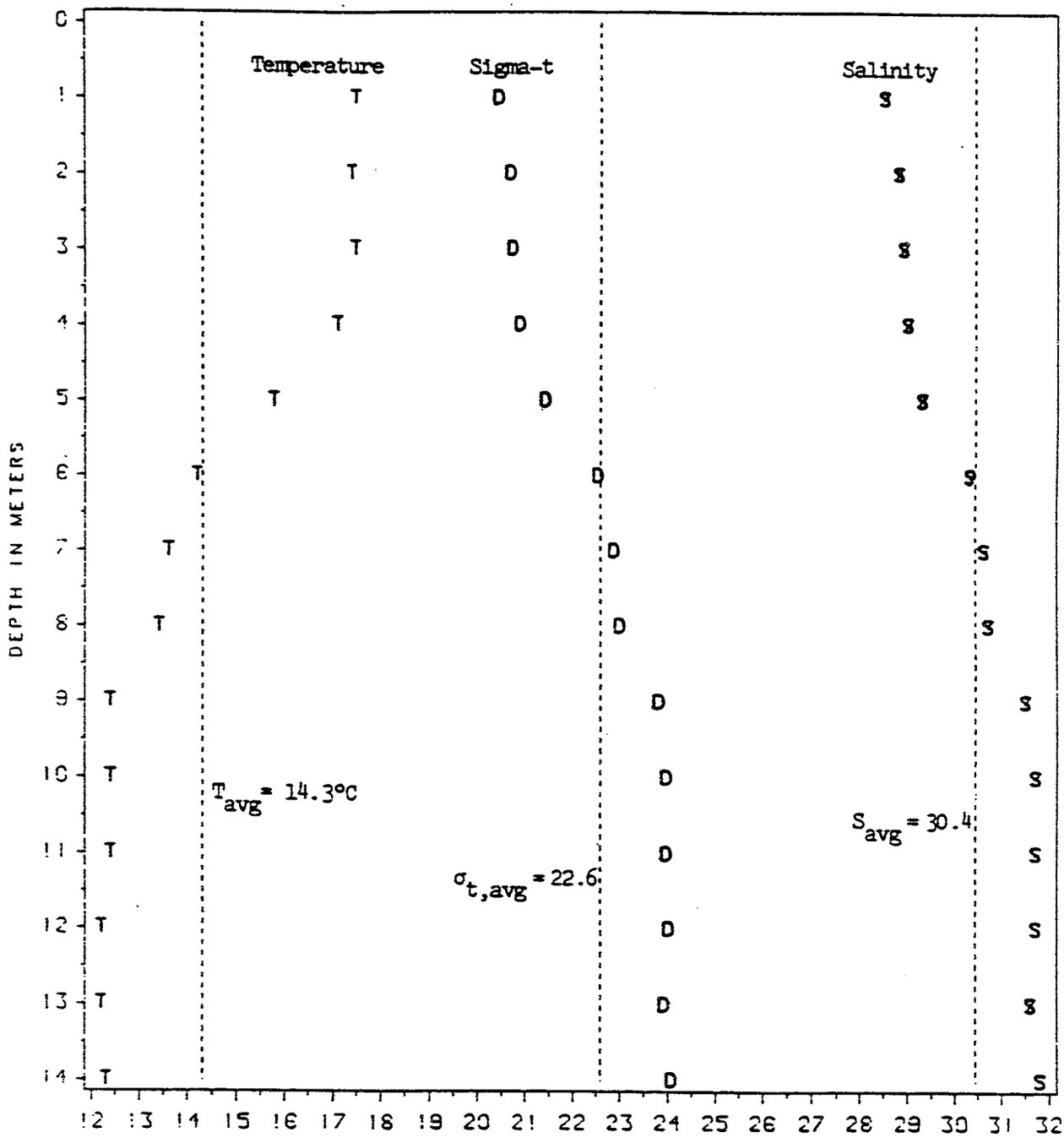

Figure 4.19 Temperature, sigma-t, and salinity versus depth for Brightman station (Figure 3.4) on May 20, 1986, approximately 2.5 hours before high tide at Newport, Rhode Island.

$$K = \frac{gh^3}{48\rho N_z} \frac{\partial \rho}{\partial x}$$

This equation is plotted in Figure 4.20 and is seen to be a two-layer flow with the upper layer moving in the direction of increasing density and the lower layer moving in the opposite direction with the same volume flux.

The maximum velocities in the two layers are given by

$$u_{s,max} = K \qquad \text{at } z = 0$$

$$u_{b,max} = 0.6875\ K \qquad \text{at } z = 0.75h$$

We may use this simple theory to compare with the measured residual currents in the Taunton River at the Brightman station.

From an intensive series of field measurements on July 9, 1986, to be discussed in Section 4.3.3, the mean density gradient along the ship channel in Mt. Hope Bay was found to be

$$\frac{1}{\rho} \frac{\partial \rho}{\partial x} = 2 \times 10^{-7}\ m^{-1}$$

This value is nearly independent of position in the channel and time in the tidal cycle and may be used in evaluating K in Equation (4.2). The channel depth near Brightman station, from Figure 4.19, is h = 14 m. But the eddy viscosity N_z is unknown and must be estimated. In Chapter 4 of his dissertation, Hess (1974) reviews the various experimental correlations for

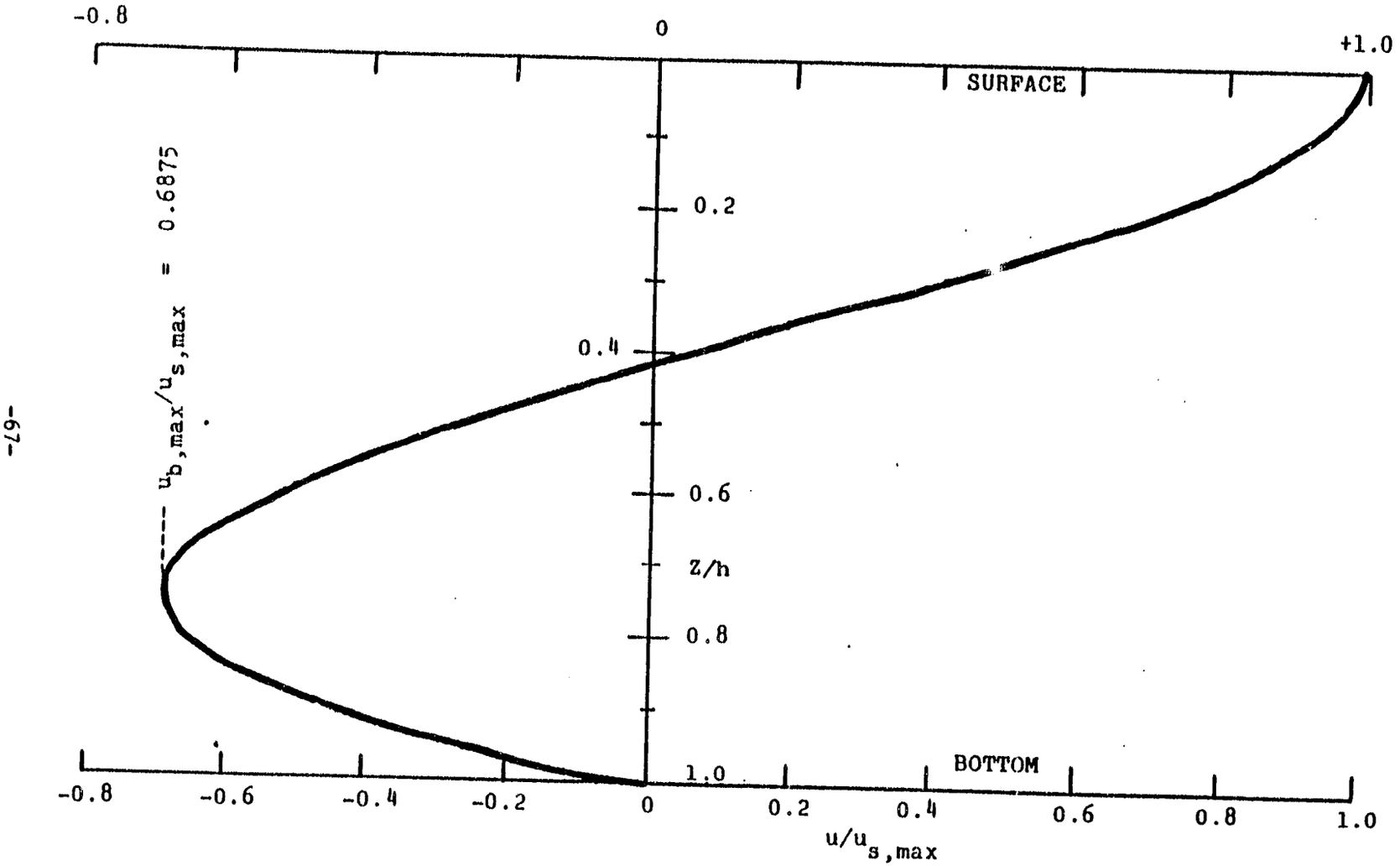

Figure 4.20 Theoretical shape of a two-layer density current from Equation (4.2), after Officer (1976).

vertical eddy viscosity. He recommends - and uses in his computer model - the following empirical formula:

$$N_z = 0.0004\ U\ h \qquad (4.3)$$

where U is the maximum tidal velocity of the channel, which at Brightman station is approximately 40 cm/s. Introducing these values into Equation (4.2) gives an estimate of K = 0.05 m/s. Thus the simplified theory from Equation (4.2) predicts, at Brightman,

$$u_{s,max} = 5.0 \text{ cm/s}$$

$$u_{b,max} = 3.4 \text{ cm/s}$$

These are comparable to but about twice as large as the measured Brightman residual flows from Figures 4.17 and 4.18. Since the field measurements could not monitor mean density gradients or vertical eddy viscosities, it is difficult to determine if the discrepancy is due to non-local, wind, or topographic effects. We can only conclude that the Taunton River residual flow is consistent with a two-layer density-driven model.

Equation (4.2) assumes a very wide estuary with negligible horizontal diffusion. Hansen and Rattray (1965) modified the theory to include a finite width b and eddy diffusion of salt (density). Their refined theory gives velocity profiles very similar to Figure 4.20, but the maximum up-and down-estuary velocities are related not to mean density gradient but the mean freshwater velocity,

$$u_r = Q_r/A_{section}$$

where Q_r is the river flow and $A_{section}$ is the cross sectional area of the estuary, and a gravitational Rayleigh number:

$$R = \frac{g\alpha\bar{S}\ h^3}{N_z K_x} \tag{4.4}$$

where $\bar{S}$ is the mean salinity in the water column, α is the saline density expansion coefficient ($= 8\times10^{-4}$ at 15°C), and K_x is the horizontal eddy diffusion coefficient. Figure 4.21 plots the maximum velocities in each layer as a function of the product (ν Ra), where ν is a small parameter related to Ra and a horizontal diffusion parameter M defined by

$$M = K_z K_x b^2/Q^2 \tag{4.5}$$

Assuming zero wind, Hansen and Rattray (1965) derive the following algebraic equation for computing ν:

$$1630\ (M1-\nu) = 32\nu + 0.033\ \nu^2 Ra + 0.022\ \nu^3 Ra^2 \tag{4.6}$$

They also treat surface wind shear effects, which we omit in the present discussion. Finally, in addition to velocity, their theory leads to salinity distributions as a function of z/h, Ra, and M. Here we refer only to their result for the salinity S_o at the surface:

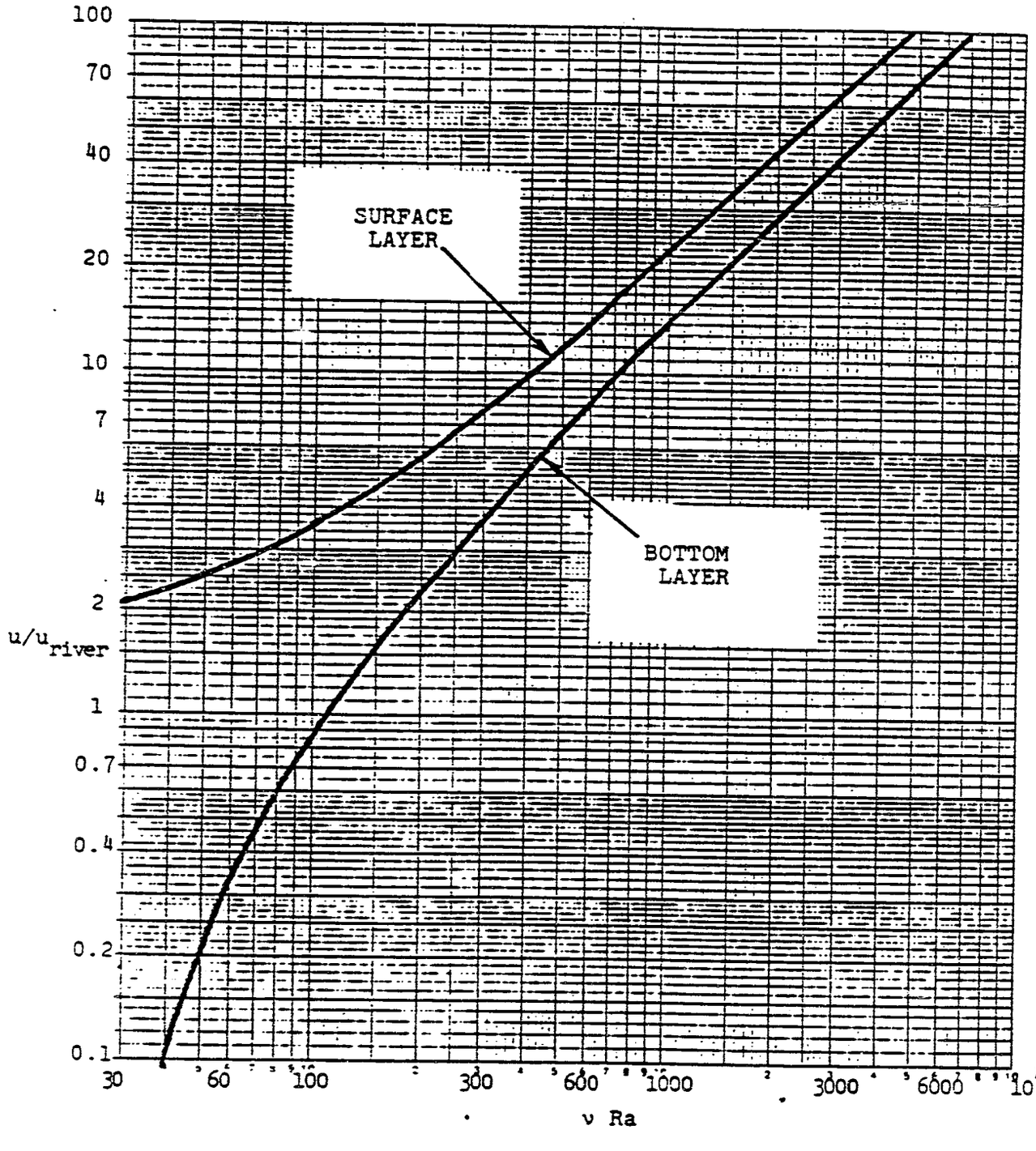

Figure 4.21 Maximum surface and bottom density-driven velocities from the theory of Hansen and Rattray (1965) for zero wind.

$$\frac{M}{\nu}\left(1 - S_o/\bar{S}\right) = 0.092 + \nu Ra/576 \qquad (4.7)$$

Again we cannot compare this theory to actual measurements without estimating the eddy coefficients. We assume that N_z is given by Equation (4.3) and use a similar correlation for K_x also recommended by Hess (1974):

$$K_x = 0.293\ U\ h \qquad (4.8)$$

We then apply the theory to the Taunton River data as we did before for Officer theory.

With S = 30.4°/•• from Figure 4.19, we have sufficient information to evaluate Ra= 1.76 x 10^5 from Equation (4.4). Rather than evaluate M by using still a third empirical correlation of K_z, which varies strongly with the degree of stratification in the estuary (Hess, 1974, Figure 4.7), we attempt to fit the theory directly to the observed salinity distribution. From Figure 4.19, S_o = 28.4•/••,, sot that Equation (4.7) becomes

$$u_b = 7 \text{ cm/s}$$

These are about three times higher than the measured residual flows in Figures 4.17 and 4.18. These discrepancies are sufficient to conclude that existing density-flow theory cannot be used for an accurate <u>prediction</u> of the residual flows in a given estuary. Rather, the estuary data can later be used to <u>calibrate</u> the theory to the particular location.

4.3.4 Intensive Tidal Cycle Measurements

An intensive series of salinity and temperature measurements were taken in Mt. Hope Bay over approximately one tidal cycle, from 0546 to 1727 on May 20, 1986. The times for high tide in Newport, Rhode Island on that day were 0523 and 1750.

As shown in Figure 4.22, the data were taken at ten stations in the bay. There were two stations at each water boundary: Taunton River (#1,2), Mt. Hope Bridge (#6,7), and Sakonnet (#8,9). The remaining four stations (#3,4,5,10) were at various mid-bay points. At each station salinity and temperature were measured at 1-meter depth intervals from surface to bottom. Boat travel time was such that each station could be visited every four hours. For example, measurement times at station #1 were 0546, 0956, 1406, and 1718. The complete data set from this survey is given in Appendix E.

The discussion here is primarily upon the tidally averaged data. At the Brightman stations (#1,2), tidal excursions in salinity were significant, up to 2.6°/••, but at all other stations the variation was 1°/•• or less.

As might be expected, the tidally-averaged salinity was spatially variable, depending on the relative proportions of freshwater and saltwater flow present in the station cross-section. Figure 4.23(a) shows the mean salinity structure at stations 1 and 2 near Brightman Bridge in the Taunton River. The river is clearly stratified, with salinity differences of 3°/•• from surface to bottom. This type of structure causes the strong density currents noted already in Section 4.3.3. The Taunton River would be classically described as a partially mixed estuary (Officer 1976).

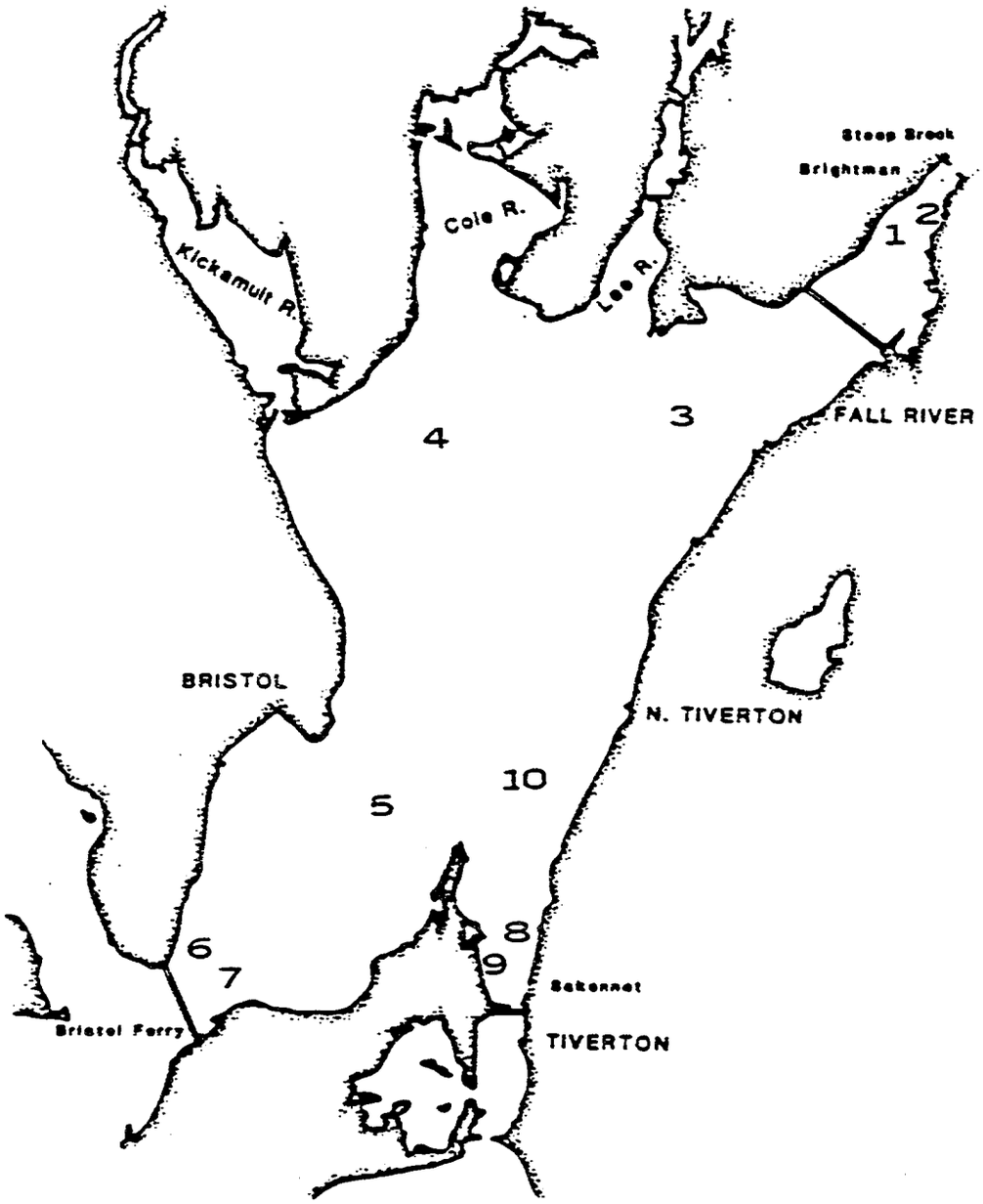

Figure 4.22 The ten measuring stations for the intensive survey of May 20, 986.

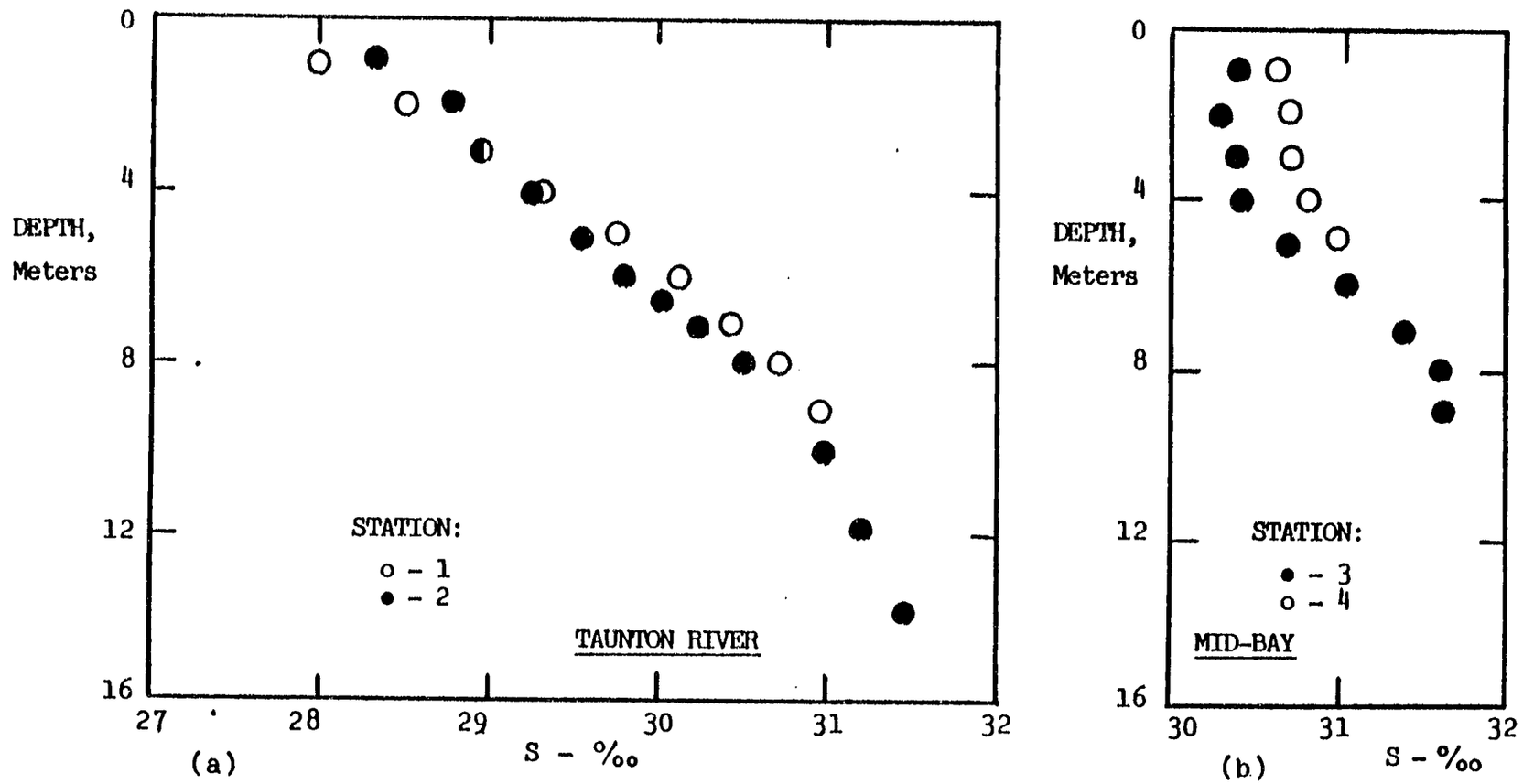

Figure 4.23 Mean salinity profile during the intensive survey of May 20, 1986: (a) Taunton River; (b) mid-bay.

Further down the ship channel, at station 3, the stratification is less pronounced, as shown in Fig. 4.23(b). Neighboring station 4, out of the ship channel in shallower water, shows nearly uniform (well-mixed) salinity.

The stations near the Mt. Hope and Sakonnet boundaries in Figure 4.24 show decreasing stratification, with surface-to-bottom salinity differences of 0.6°/•• or less. The sections very near the boundaries (#5,6,8,9), where tidal flow overwhelms the freshwater contributions, are well-mixed. The interior points slightly up-estuary (#7,10) are slightly stratified. We conclude that saline stratification decreases monotonically as we proceed down-estuary from the Taunton River and is more pronounced in the ship channel. The profiles at Mt. Hope Bridge and Sakonnet are well-mixed, which helps explain why no two-layer density flows were detected there, as discussed in Section 4.3.2

The mean properties computed from this survey can be used to sketch - with considerable uncertainty but at least qualitative accuracy - the spatial distributions of salinity and temperature in Mt. Hope Bay. Figure 4.25 shows the mean surface salinity in the bay. There is a 2°/•• drop up to the Brightman St. Bridge station. Thus the surface longitudinal density gradient in the River is nearly three times greater than in the Bay proper, implying stronger density currents.

The distribution of mean bottom salinities in the Bay is given in Fig. 4.26. Bottom salinity gradients are considerably less than at the surface due to strong up-estuary saltwater intrusion and highly variable bottom topography.

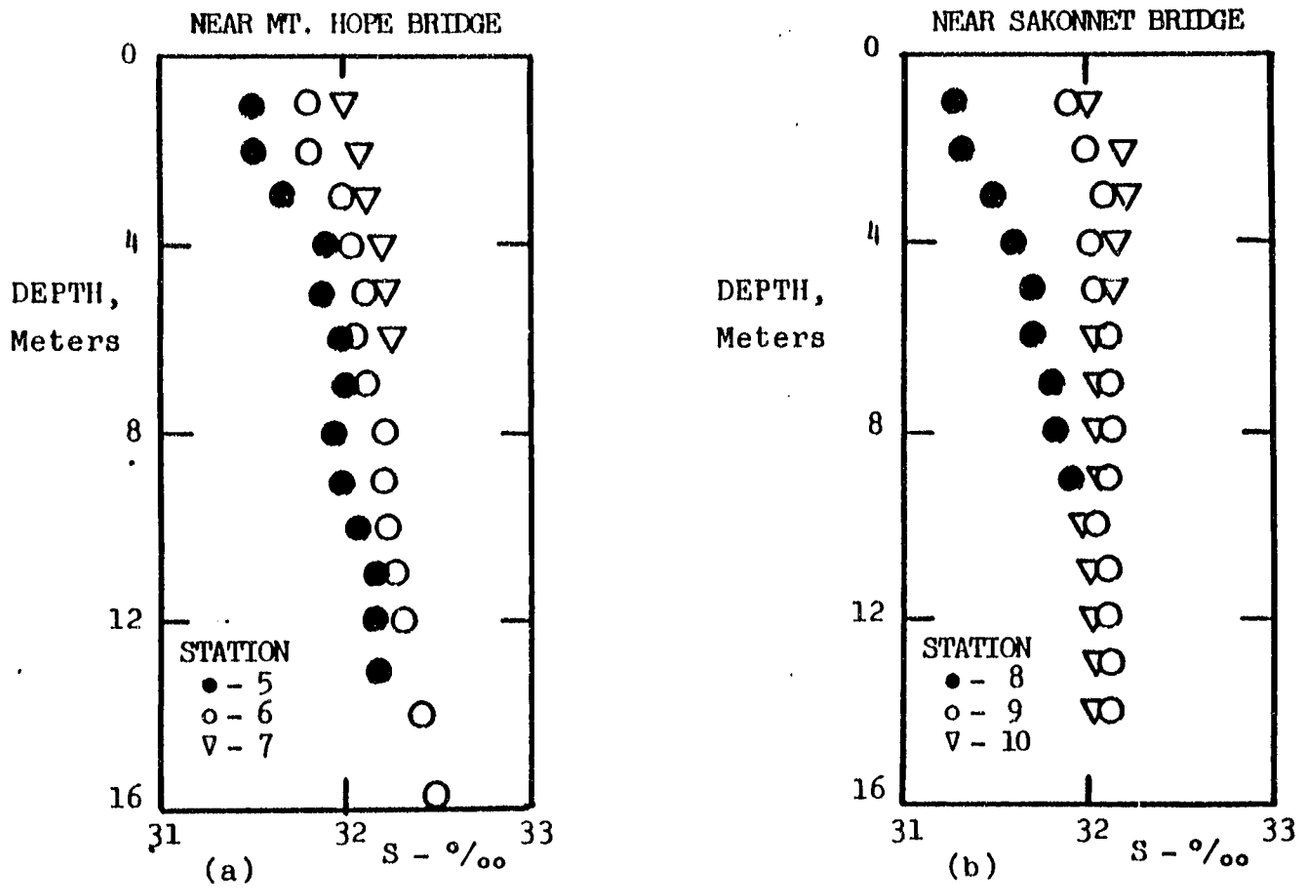

Figure 4.24 Mean salinity profiles during the intensive survey of May 20, 1986; (a) near Mt. Hope Bridge; (b) near Sakonnet.

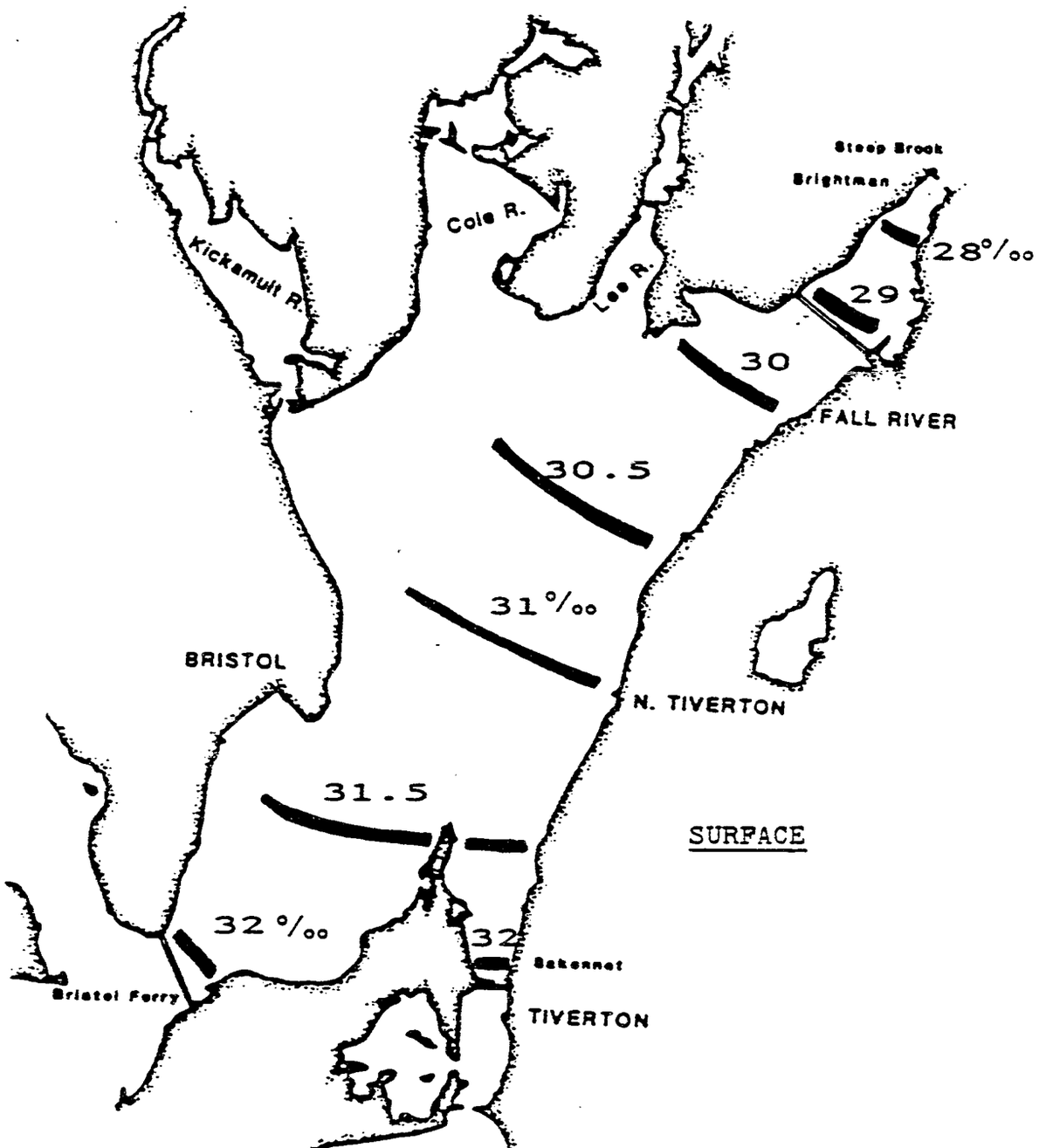

Figure 4.25 Average surface salinities in Mt. Hope Bay from the intensive survey of May 20, 1986.

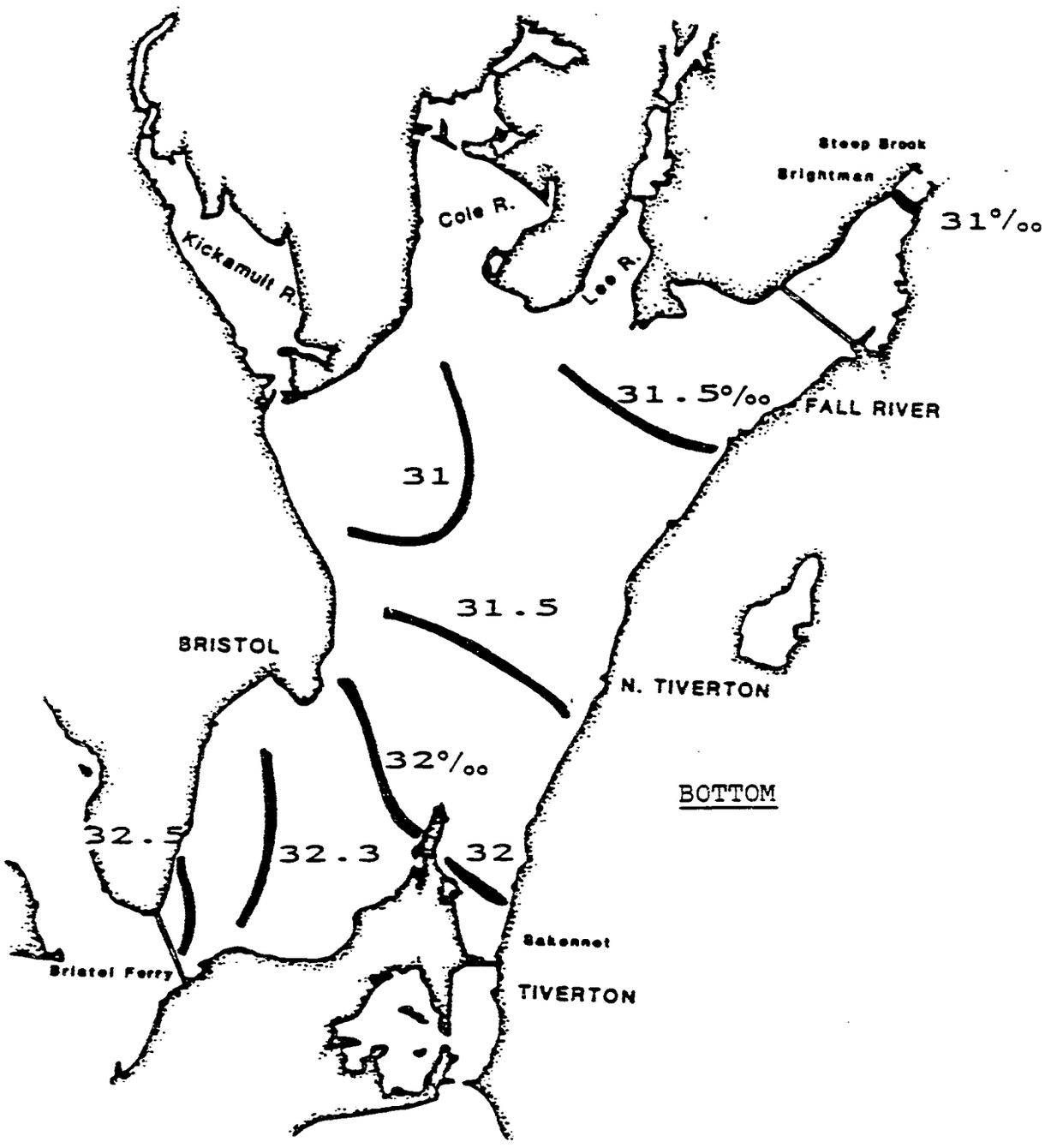

Figure 4.26 Average bottom salinities in Mt. Hope Bay from the intensive survey of May 20, 1986.

The average surface temperatures in the Bay on this day (20 May 1986) are shown in Fig. 4.27. Basically the surface waters become warmer up-estuary, with the hottest area (18°C) being near the thermal outfall of the Brayton Point power plant. In contrast, the mean bottom temperatures shown in Fig. 4.28 are more irregular and seem to be warmest in the center of the bay. The variable bottom topography and the presence of the Brayton Point thermal outfall make interpretation of these bottom temperature contours difficult.

The tidally-averaged vertical temperature profiles are shown in Figure 4.29 and are similar qualitatively to the mean salinity profiles. The thermal structures of the Taunton River and nearby stations (Figure 4.29 (a)) are stratified, with vertical variations of 4°-5°C. Somewhat less stratification is seen in Figure 4.29(b) at the stations near Mt. Hope Bridge (#5,6,7). The two stations at the Sakonnet River Bridge (#8,9) are thermally well mixed, but nearby ship-channel station 10 shows vertical variations of 2°C. In general, vertical temperature variations are stronger everywhere in the Bay than their equivalent salinity variations. It is not known to what extent this thermal structure is affected by the thermal outfall from Brayton Point.

As mentioned, the tidal excursions of salinity and temperature were small everywhere except in the Taunton River. The time variation of instantaneous salinity profiles at station 2 near Brightman Street are shown in Figure 4.30. These profiles were measured at approximately 250-minute intervals, beginning and ending near high tide. One can see - with some artistic license - that these profiles essentially vary tidally from top to bottom, with the surface salinity 'wave' leading the bottom

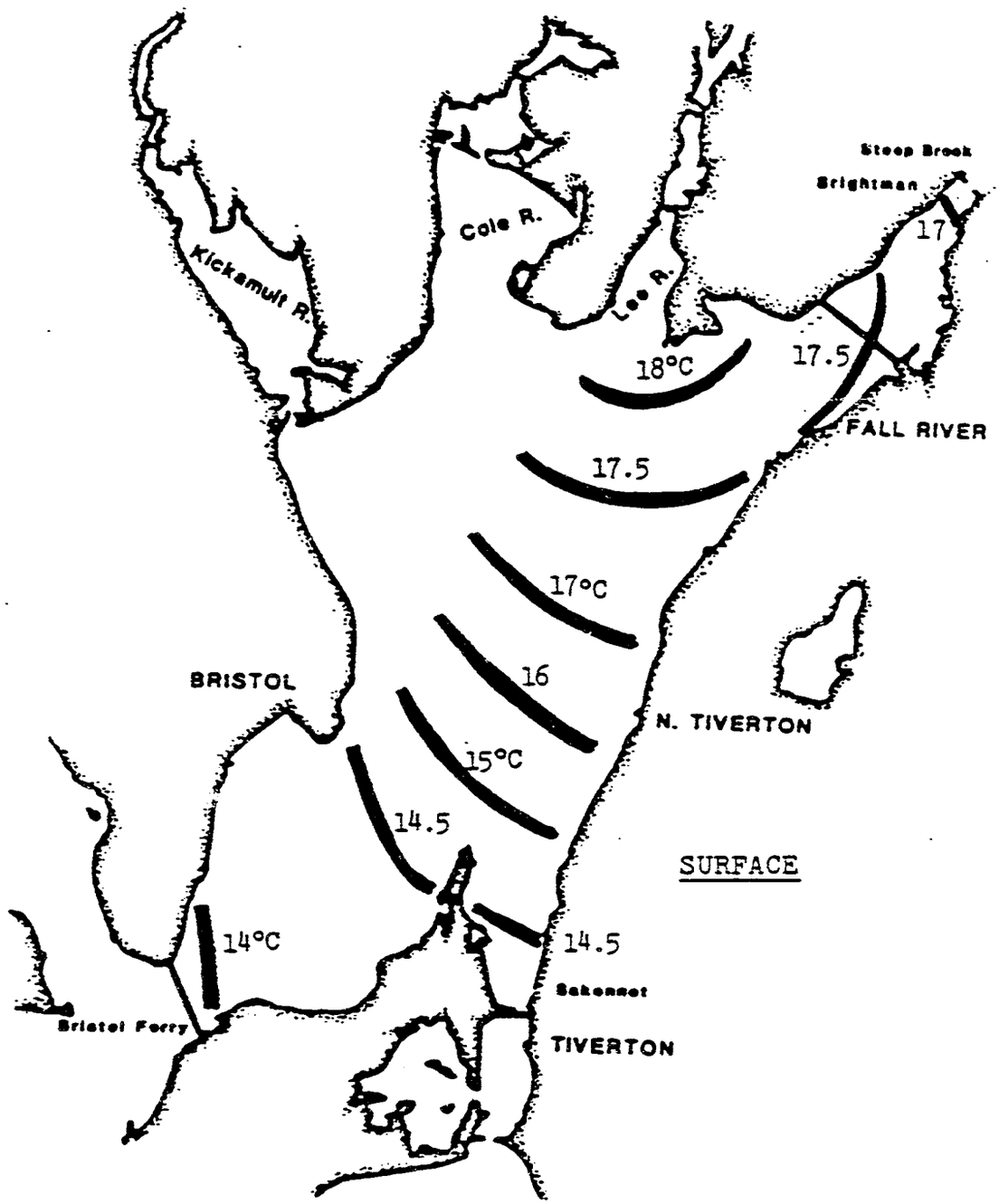

Figure 4.27 Average surface temperatures (°C) in Mt. Hope Bay from the intensive survey of May 20, 1986.

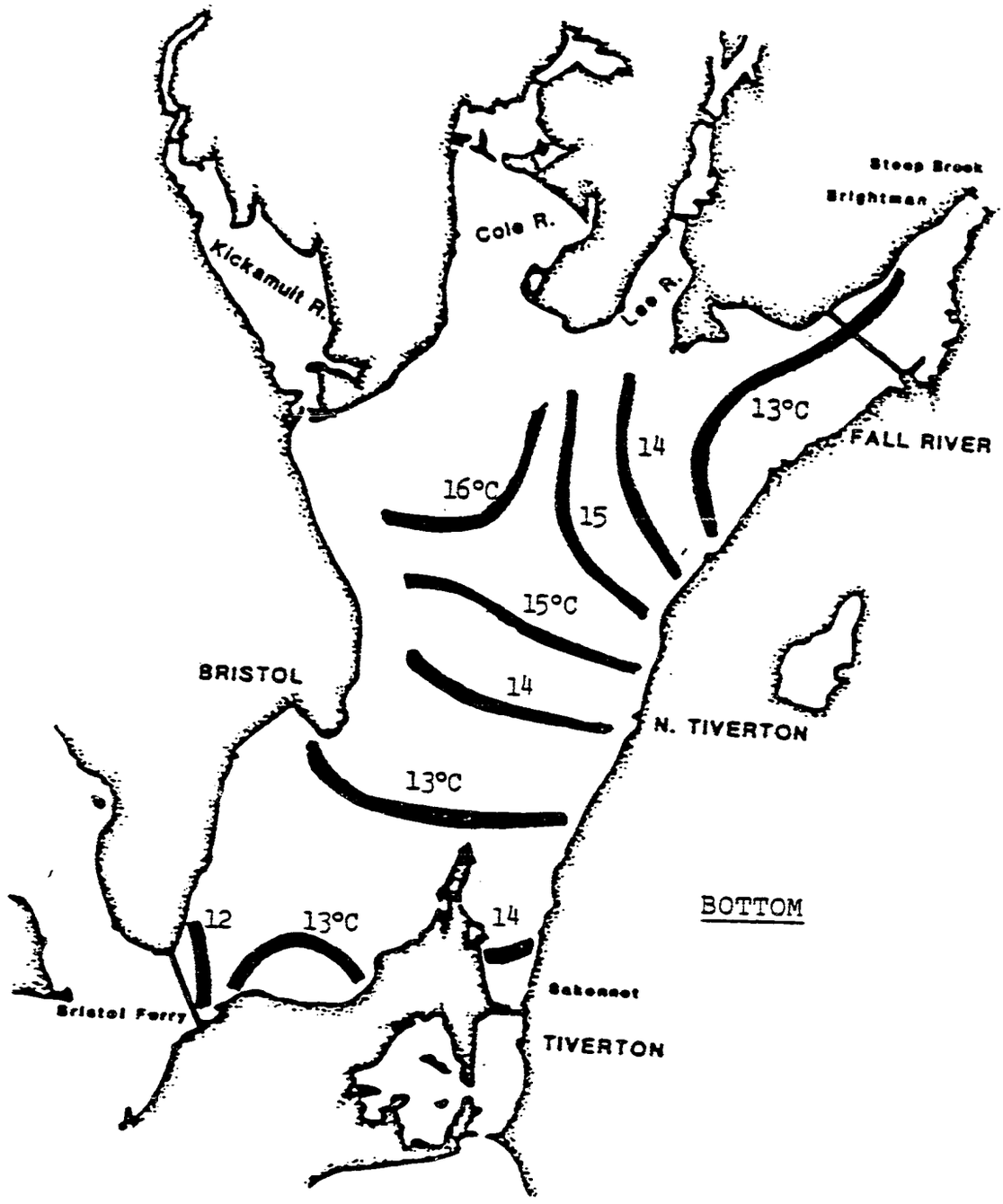

Figure 4.28 Average bottom temperatures (°C) in Mt Hope Bay from the intensive survey of May 20, 1986.

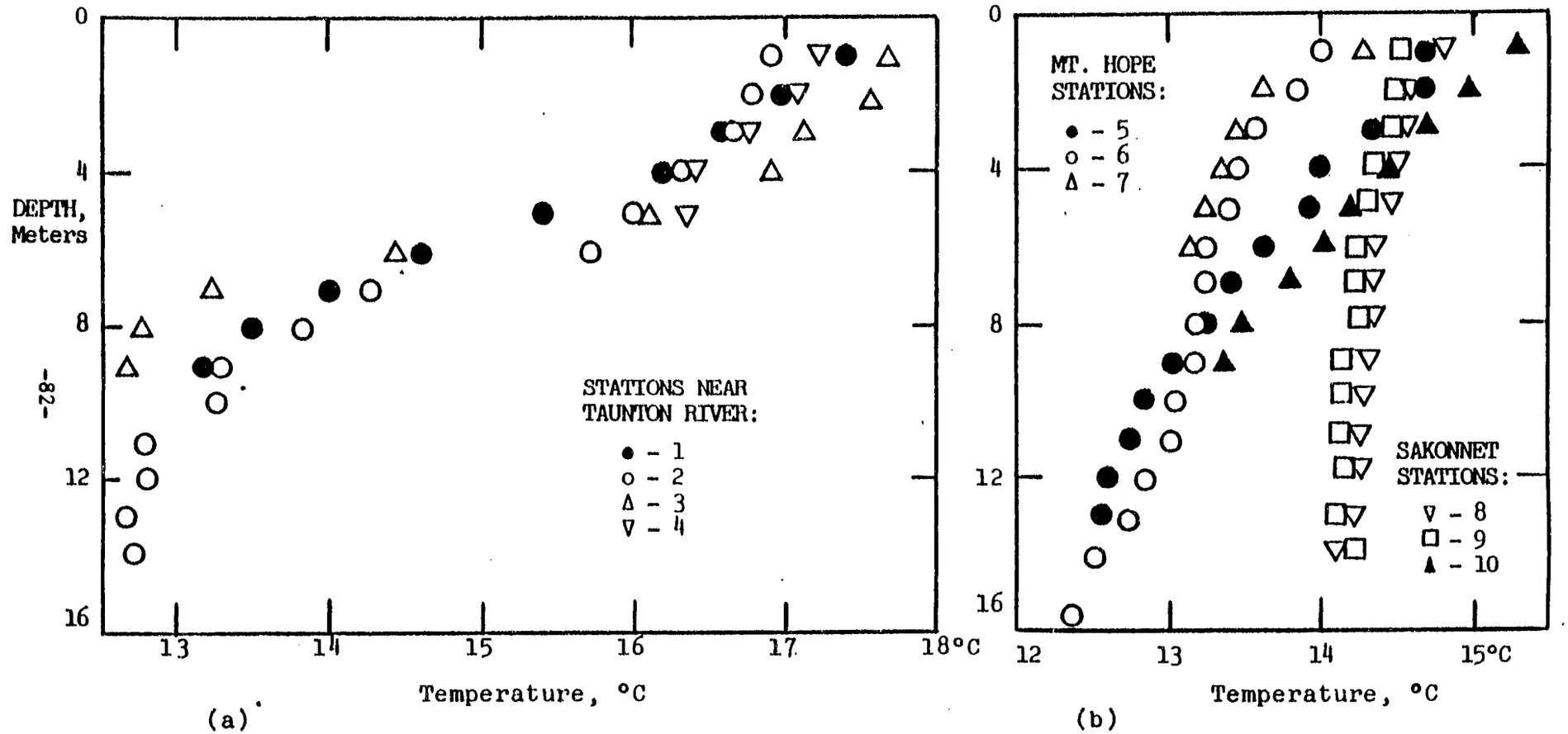

Figure 4.29 Mean temperature profiles during the intensive survey of May 20, 1986: (a) near the Taunton River; (b) near the Mt. Hope Bridge or the Sakonnet River Bridge.

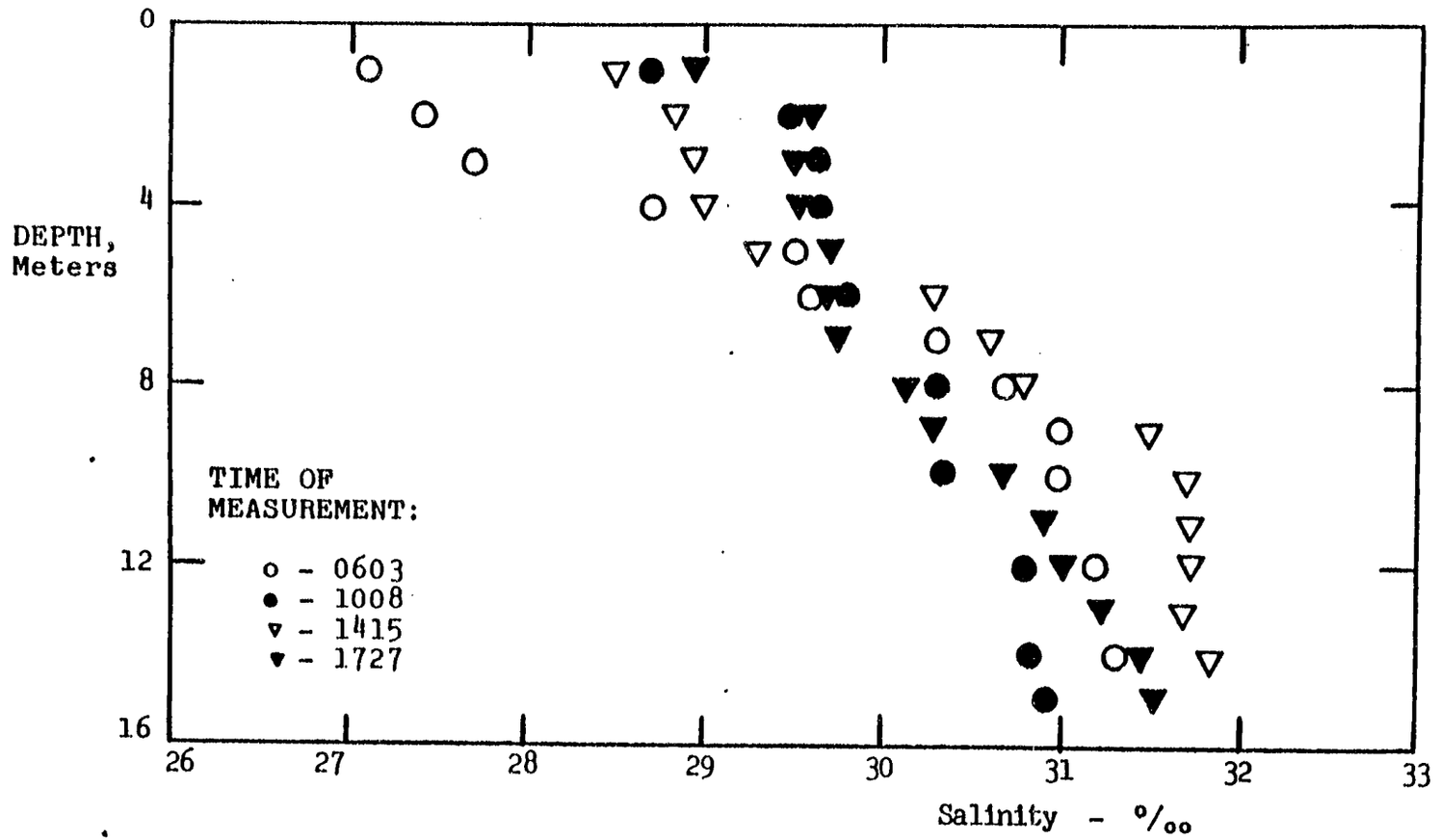

Figure 4.30 Instantaneous salinity profiles at Station #2 during the intensive survey of May 20, 1986. High tides at Newport, Rhode Island were at 0523 and 1750.

salinity variation by about three hours. Mid-depth (6 m) is nearly a nodal point for these vertical tidal variations.

The time variation of temperature profiles at station #2 in the Taunton River is shown in Figure 4.31 and shows a quite different effect from the salinity variations. The variations at each depth are approximately diurnal in character, with the surface warming and the bottom cooling. These effects are probably more related to solar heating and cooling than to tidal variations.

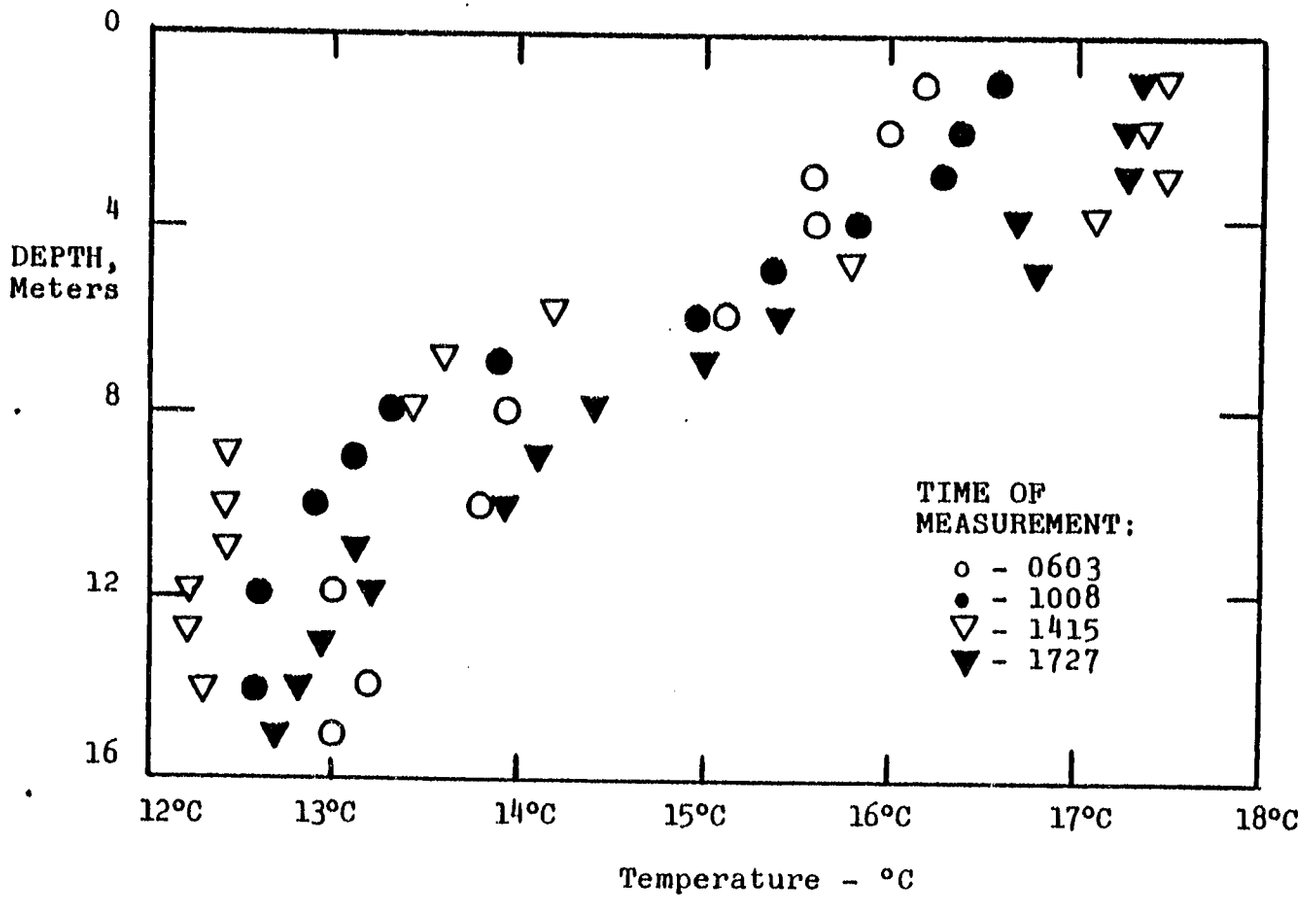

Figure 4.31 Instantaneous temperature profiles at Station #2 during the intensive survey of May 20, 1986. High tides at Newport, Rhode Island were at 0523 and 1750.

5. HYDRODYNAMIC MODEL

Finite element and boundary fitted coordinate hydrodynamic models have been employed to predict the circulation in Mt. Hope Bay. The finite element model was employed because it is one of the standard techniques used to predict hydrodynamics in coastal and estuarine areas. The boundary fitted coordinate model application represents an initial test of a new modeling methodology. Section 5.1 presents the governing equations used in both models. Section 5.2 outlines the solution methodologies employed for each approach. Application to the study area is given in Sections 5.3 and 5.4 for the finite element and boundary fitted coordinate models, respectively. The primary focus of the model studies has been on the tide since it predominates the current and sea surface elevation variability in the area (Section 4.1).

5.1 Governing Equations

Since the water column remains vertically well-mixed over most seasons in Mt. Hope Bay (Section 2.2, 4.3.4), a two-dimensional vertically averaged hydrodynamics model has been selected to investigate the circulation. The equations of motion and continuity, assuming a two dimensional vertically averaged representation, are found in Leendertse (1967) or Hess and White (1974). Only a brief overview is presented.

Employing the right-handed cartesian coordinate system where the vertical axis z is measured positive upwards referenced to mean sea level, the vertically averaged x and y momentum equations become

$$\frac{\partial U}{\partial t} + U\frac{\partial U}{\partial x} + V\frac{\partial U}{\partial y} = -g\frac{\partial \eta}{\partial x} + f\,V\,\frac{1}{\rho(h+\eta)}\,(\tau_{s_x} - \tau_{b_x}) \tag{5.1}$$

$$\frac{\partial V}{\partial t} + U\frac{\partial V}{\partial x} = V\frac{\partial V}{\partial y} = -g\frac{\partial \eta}{\partial x} + f\,V\,\frac{1}{\rho(h+\eta)}\,(\tau_{s_y} - \tau_{b_y}) \tag{5.2}$$

in which f is the Coriolis parameter; τ_{s_x} and τ_{s_y} are the surface shear stresses; and τ_{b_x} and τ_{b_y} are the bottom shear stresses in the x and y directions, respectively. It has been assumed that the density, ρ, is constant and that the water column is hydrostatic.

The vertically averaged velocities, U. and V, are defined as

$$U = \frac{1}{(h+\eta)}\int_{-h}^{\eta} u\,dz \tag{5.3}$$

$$V = \frac{1}{(h+\eta)}\int_{-h}^{\eta} v\,dz \tag{5.4}$$

in which u and v are the depth dependent velocity components in the x and y directions, respectively; h is the mean sea level depth; and η is the sea surface elevatopm measured from mean sea level.

The vertically averaged continuity equation becomes

$$\frac{\partial \eta}{\partial t} + \frac{\partial[(h+\eta)\,U]}{\partial x} + \frac{\partial[(h+\eta)\,V]}{\partial y} = 0 \tag{5.5}$$

Specification of bottom stress, follow the well-known quadratic relationship:

$$\tau_{b_z} = \frac{\rho g U (U^2 + V^2)^{1/2}}{C^2} \tag{5.6}$$

$$\tau_{b_y} = \frac{\rho g V (U^2 + V^2)^{1/2}}{C^2} \tag{5.7}$$

in which the Chezy coefficient, C, is weakly dependent on depth and is inversely dependent on the Manning factor n, which parameterizes bottom roughness as

$$C = \frac{K}{n} (h + \eta)^{1/6} \tag{5.8}$$

in which K is a constant which depends on the units employed.

5.2 Solution Methodology

5.2.1 Finite Element Approach

The two-dimensional vertically averaged hydrodynamic model equations (Equations 5.1, 5.2, and 5.5.) are solved using a Galerkin weighted residual finite element method with linear interpolating functions and triangular elements. A split time or semi-implicit method (Wang and White, 1976), where the continuity and momentum equations are solved in successive order, is used for the time integration. Detailed development of the numerical solution and methodology and stability criteria can be found in Isaji and Spaulding (1981) and Wang and White (1976). Additional references on finite element solutions to the shallow water wave equation include Grotkop (1973), Pinder and Gray (1977) and Wang and Connor (1975).

5.2.2 Boundary Fitted Coordinate Approach

The basic idea of the boundary-fitted coordinate system approach is to generate transformation functions such that all boundaries are coincident with coordinate lines. Following the extensive work of Thompson et al (1974, 1976, 1977a, b), Thames (1975) and Thames et al (1977) the natural coordinates ξ and η are taken as solutions of an elliptic boundary value problem with one of the coordinates constant on the boundaries.

The curvilinear coordinates are determined by solving an elliptic system of the form

$$\xi_{xx} + \xi_{yy} = P(\xi,\eta) \tag{5.9}$$

$$\eta_{xx} + \eta_{yy} = Q(\xi,\eta) \tag{5.10}$$

with Dirichlet boundary conditions, the ξ coordinate being specified as constant on the boundary and equal to another constant on the opposite boundary. The η coordinate than varies monotonically over the same range on both the boundaries. Subscripts indicate differentiation and will be used in the text to follow with x denoting the eastward direction and y the northward direction.

The dependent and independent variables in Equations (5.9) and (5.10) must be interchanged so that all numerical computations are performed in a uniform rectangular transformed plane. This results in a coupled system of quasi-linear elliptic equations for determining $x(\xi,\eta)$ and $y(\xi,\eta)$ in the transformed plane, and is given by

$$\alpha x_{\xi\xi} - 2\beta x_{\xi\eta} + \gamma x_{\eta\eta} = - J^2[x_\xi P(\xi,\eta) + x_\eta Q(\xi,h)] \tag{5.11}$$

$$\alpha y_{\xi\xi} - 2\beta y_{\xi\eta} + \gamma y_{\eta\eta} = - J^2[y_\xi P(\xi,\eta) + y_\eta Q(\xi,h)] \tag{5.12}$$

where

$$\alpha = x_\eta^2 + y_\eta^2 \qquad \gamma = s_\xi^2 + y_\xi^2$$

$$\beta = x_\xi x_\eta + y_\xi y_\eta \qquad J = x_\xi y_\eta - x_\eta y_\xi \tag{5.13}$$

While this set of equations is considerably more complex than the original set, the boundary conditions are now specified on straight lines and the coordinate spacing is uniform in the transformed plane. It should further be noted that the orthogonal and conformal curvilinear grids, as well as the simple stretched rectangular girds, are special cases of the boundary-fitted coordinate approach given here. The functions $P(\xi,\eta)$ and $Q(\xi,\eta)$ may be used to move the coordinate lines within the solution domain. Thompson et al (1977a) and Swanson (1987) approximate these by a sum of decaying exponentials which allow for both line and point attraction.

The horizontal coordinates of the model domain are next transformed such that ξ and η become independent variables. The transformations are given as

$$F_x = \frac{1}{J}[(Fy_\eta)_\xi - (Fy_\xi)_\eta] \tag{5.14}$$

$$F_y = \frac{1}{J}[(Fx_\eta)_\xi - (Fx_\xi)_\eta] \tag{5.15}$$

where F denotes some arbitrary function and J is the Jacobian defined by the coordinate transformation (Equation 5.13). This transformation maps the (x,y) coordinate system to (ξ,η) space. The horizontal velocities however remain in their original orthogonal form. The boundary conditions are also transformed to achieve no flux at the closed boundaries, and appropriate stresses and dynamic conditions at the free surface and bottom boundaries.

The reader is referred to Swanson (1987) for a detailed presentation of the derivation of the governing equations and the associated boundary conditions in boundary fitted coordinates.

The first step in the computational procedure is to compute the spatial derivative x_ξ, x_η, y_ξ and y_η and Jacobian J at each grid point using the transformation equations (Equations 5.11 and 5.12). The derivatives, scaled to the appropriate size, are then available as input to the circulation model and constitute a complete description of the mesh geometry.

The basic approach to solving the equations of motion is to split them into an exterior or vertically averaged mode and an interior mode which describes the vertical structure. The rationale for this approach is to solve those terms which restrict the time step implicitly and the other terms explicitly thus increasing the allowable time step and hence reducing the computational time for a simulation.

The vertically averaged equations of motion and continuity are solved using a semi-implicit method (Madala and Piacsek, 1977; Swanson, 1987) on a space-staggered grid system (Method C grid of Arakawa and Lamb, 1977). The new time velocities from the momentum equations are algebraically

substituted into the continuity equation resulting in a Helmholtz equation. This equation is then solved by Gaussian elimination or successive over relaxation (SOR) methods to predict surface elevations. The new time velocities are then determined explicitly from the new time surface elevations through the momentum equations. The interior mode is then executed. The vertical structure of the horizontal velocities is calculated using an explicit calculation with an implicit specification of the vertical diffusion term. The procedure is repeated for the desired number of time steps.

The transformation derivatives x_ξ, x_η, y_ξ and y_η and the resulting Jacobian are defined at all variable locations of the hydrodynamic model grid. This requires that the grid transformation calculations be performed on a grid with twice the resolution of the circulation model. The use of this higher resolution grid for the transformation calculations removes the need for averaging the transformation derivatives in the circulation model and assures a geometrically conservative mapping.

Model formulation and implementation, in computer code, were tested using a series of illustrative examples in which analytic solutions were available for comparison and determination of model performance. In these test cases the nonlinear convective acceleration terms were ignored and the governing equations solved on a Cartesian coordinate system to permit comparison with analytic solutions. The model was applied in a two dimensional vertically averaged mode to predict seiching in a frictionless constant depth and width basin (Officer, 1976), tidal propagation in a wedge shaped sector with constant and variable bottom topography following Lynch and Gray (1978), and wind forced flow in a closed elliptic

cylindrical basin (Blumberg and Herring, 1982). In the three dimensional mode the model was applied to steady wind driven flow in a closed basin and to density induced forcing in rectangular channel (Hansen and Rattray, 1965). In all cases the model agreed well (within 2-3%) with the corresponding analytic solution. A detailed presentation of the model specifications and comparisons to the analytic solutions are given in Swanson (1987).

5.3 Application of Finite Element Hydrodynamic Model to Study Area

The two-dimensional finite element hydrodynamic model was applied to the Mt. Hope Bay study area. The lower Taunton River, south of the Segreganset River discharge to the Taunton, was approximated by a variable width and depth channel. Open boundaries were placed across the transect under the Mt. Hope Bridge and across the causeway at the connection between Mt. Hope Bay and the Sakonnet River. Freshwater inflow was specified at the head of the Taunton River at 13 m^3/s. Contributions from the Kickamuit, Cole, and Lee Rivers into Mt. Hope Bay were ignored because they are extremely small compared to the Taunton discharge.

The Mt. Hope Bay portion of the study area was approximated by the triangular mesh finite grid system shown in Figure 5.1. Only the representation of the lower portion of the Taunton River is shown. The finite element mesh was chosen to allow variable resolution throughout the study area and specifically to provide higher resolution in areas where bathymetric gradients or topographic changes, and hence changes in currents and sea surface elevation, are significant. In general the finest resolution was employed in the lower reaches of the Taunton River.

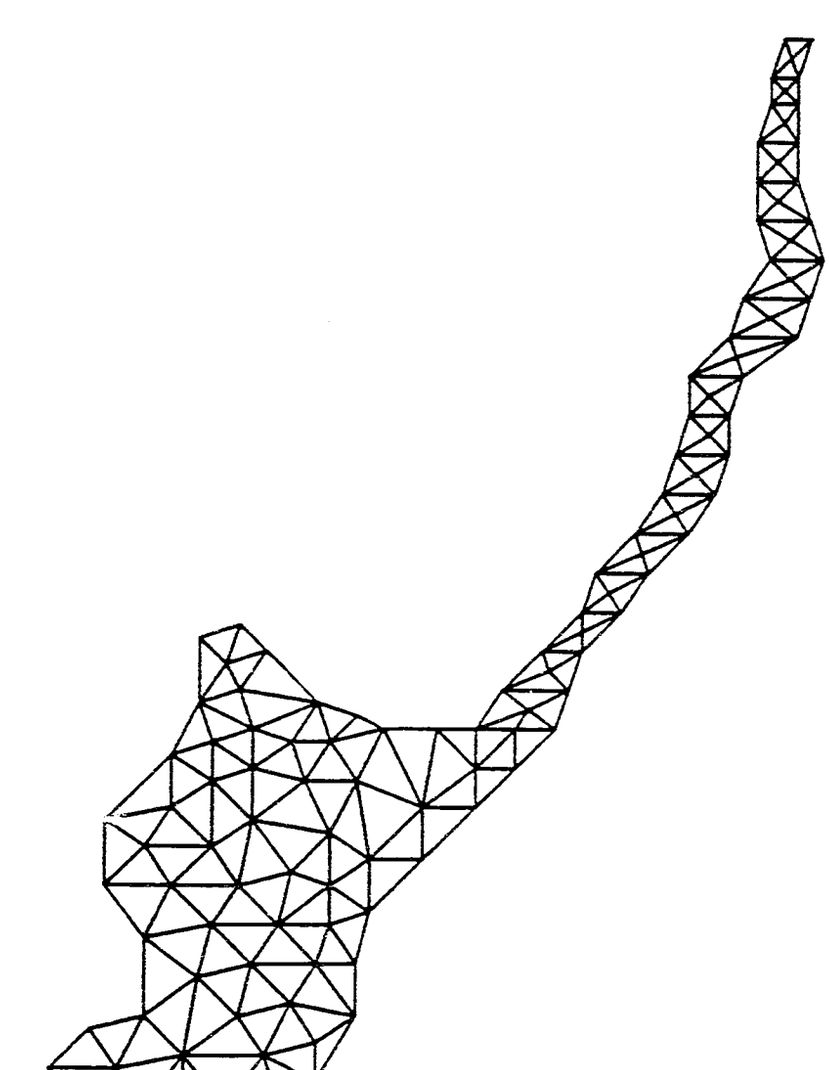

Figure 5.1 Triangular finite-element grid system used to describe the study area.

For each node the mean low water (MLW) depth was determined from the NOAA/NOS (National Ocean Survey) navigation charts for Narragansett Bay and Fall River (Chart Nos. 13221 and 13227). Depths inside the particular triangle were averaged to provide an estimate of the local depth for input to the model. Since the NOS charts provide estimates of the mean low water (MLW) depth the values were corrected to Mean Sea Level (MSL) by adding half the tidal range. The tidal range was assumed to be constant throughout the area at 1.1 m (Section 4.1). The approximate river geometry north of the confluence with the Segreganset River in Dighton, Massachusetts (width/depth or cross-sectional area) was obtained from a USGS map of the region.

5.3.1 Free Oscillation Experiment

To determine the natural frequency of Mt. Hope Bay and the Taunton River, a simple free oscillation experiment was performed. The hydrodynamic model was initiated with a cosine surface elevation profile proceeding from zero at the Mt. Hope Bay bridge transect and reaching a maximum value of 0.5 m in the vicinity of Fall River. No cross bay variation of elevation was assumed. The major axis of the system is assumed along the direction of the shipping channel. The boundary condition at the Mt. Hope Bay transect was set to zero surface elevation and the Sakonnet River boundary was assumed closed.

The model predicted surface elevation power spectrum was analyzed and showed a primary response at a period of 3.5 hours. This value can be compared to the 5.7 hours estimate for Narragansett Bay by Haight (1936) based on a simple analytic expression and the 4.8 hour estimate based on

hydrodynamic model simulations by Hess and White (1974) and Gordon (1982). No independent estimates however are available for Mt. Hope Bay.

5.3.2 River Flow

One area of particular interest is how the flow from the Taunton River is divided between the Sakonnet River and the east passage of Narragansett Bay on its way to Rhode Island Sound. Assuming that the tides have relatively little influence on the extremely small river flows the hydrodynamic model was run to estimate the flow distribution between the two exits from Mt. Hope Bay. An arbitrary river flow rate of 1000 units/s was specified at the head of the Taunton River. The free surface elevations at the Mt. Hope Bridge and Sakonnet River transects were held at mean sea level. Figure 5.2 shows the model predicted flow velocity after steady state conditions were achieved. The velocities drop dramatically as the flow discharges into the Mt. Hope Bay proper due to the large increase in cross-sectional area. The model predicted distributions show that 68% of the flow volume exists through the Mt. Hope Bridge transect. The remaining 32% exists southward through the Sakonnet River. These calculations are in excellent agreement with Hicks (1959) estimates of 70% to 30%, respectively.

5.3.3 Tidal Simulations

As noted in Section 4.1 the tide and in particular the M_2 component (period 12.42 hours) dominates the variability in the observed currents. A simulation of the M_2 tide was performed to determine the tidal currents in the area. The surface elevation and currents were started at rest for the

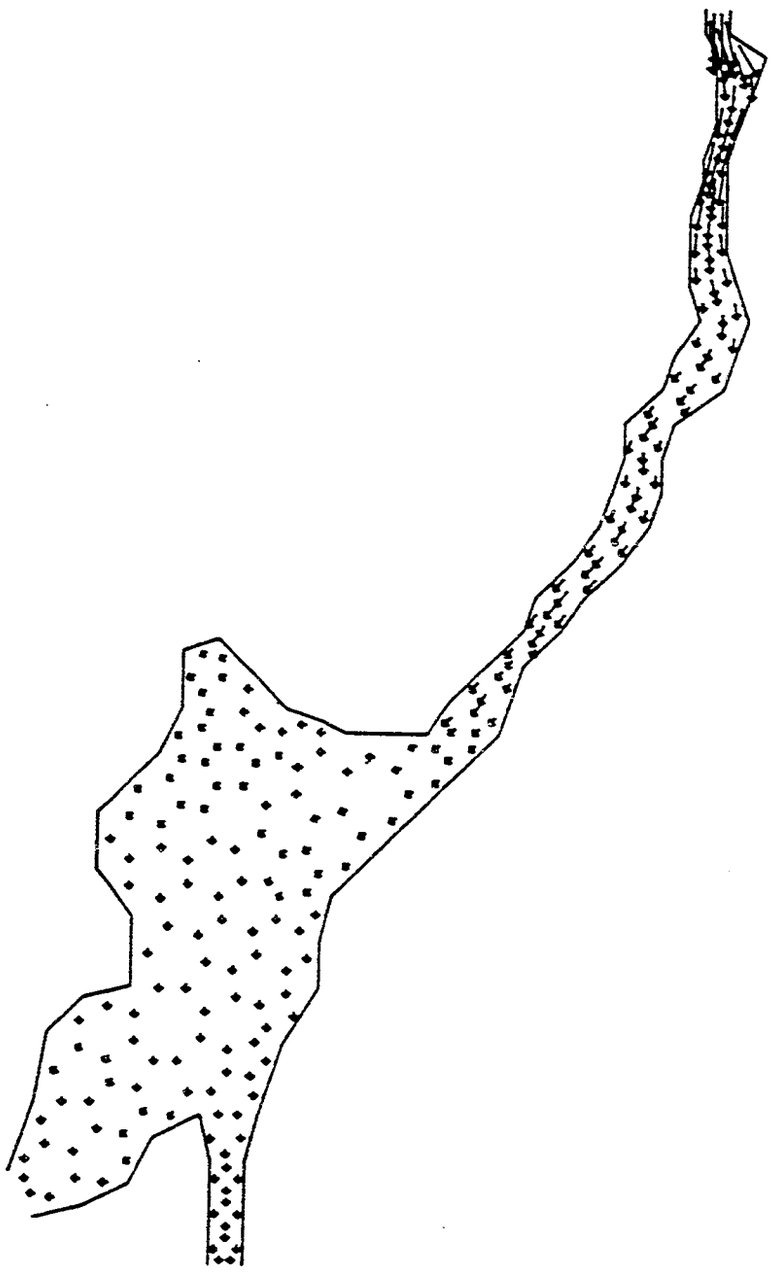

Figure 5.2 Model predicted currents for an imposed flow issuing from the Taunton River.

tidal simulations. Tidal amplitudes and phases on the Mt. Hope Bridge and Sakonnet River open boundaries were specified based on interpolation of NOAA/NOS observations from the general area (Turner, 1984). No other forcing (i.e. wind) was included. The amplitude and phase (Greenwich) were 5.3. cm and 221° respectively at both Mt. Hope Bridge and the head of the Sakonnet River. The Manning friction factor was set to 0.03 and was held constant throughout the study area.

Figures 5.3 and 5.4 show the model predicted currents for maximum flood and maximum ebb conditions, respectively. The current pattern is primarily controlled by the sharp variations in cross sectional area of the system and by the deep water channel proceeding from Mt. Hope Bridge to the lower Taunton River (in the vicinity of Fall River). The currents along this general axis are generally stronger than those in shallower water to the northwest or in the entrance to the Sakonnet River. The maximum current occur in a narrow section of the lower Taunton River near the Brightman Street Bridge and reach values of 23.6 cm/s (observed, 22.6 cm/s). The entrance to Mt. Hope Bay under the bridge has the highest currents with maximums of only a few cm/s (observed, 4.6 cm/s). Similarly weak currents are observed off the Gardners Neck and Touisset areas.

Figure 5.5 shows the tidal current roses. A tidal rose is constructed by drawing the predicted tidal current vectors at two hour intervals from a common reference point. The figure shows that for the majority of the area the tidal currents are rectilinear (flood and ebb currents are opposite in direction). Only in areas of low currents is there any circular or elliptic pattern to the roses and even there the deviations from the rectilinear behavior are minor. The directional response of the roses is

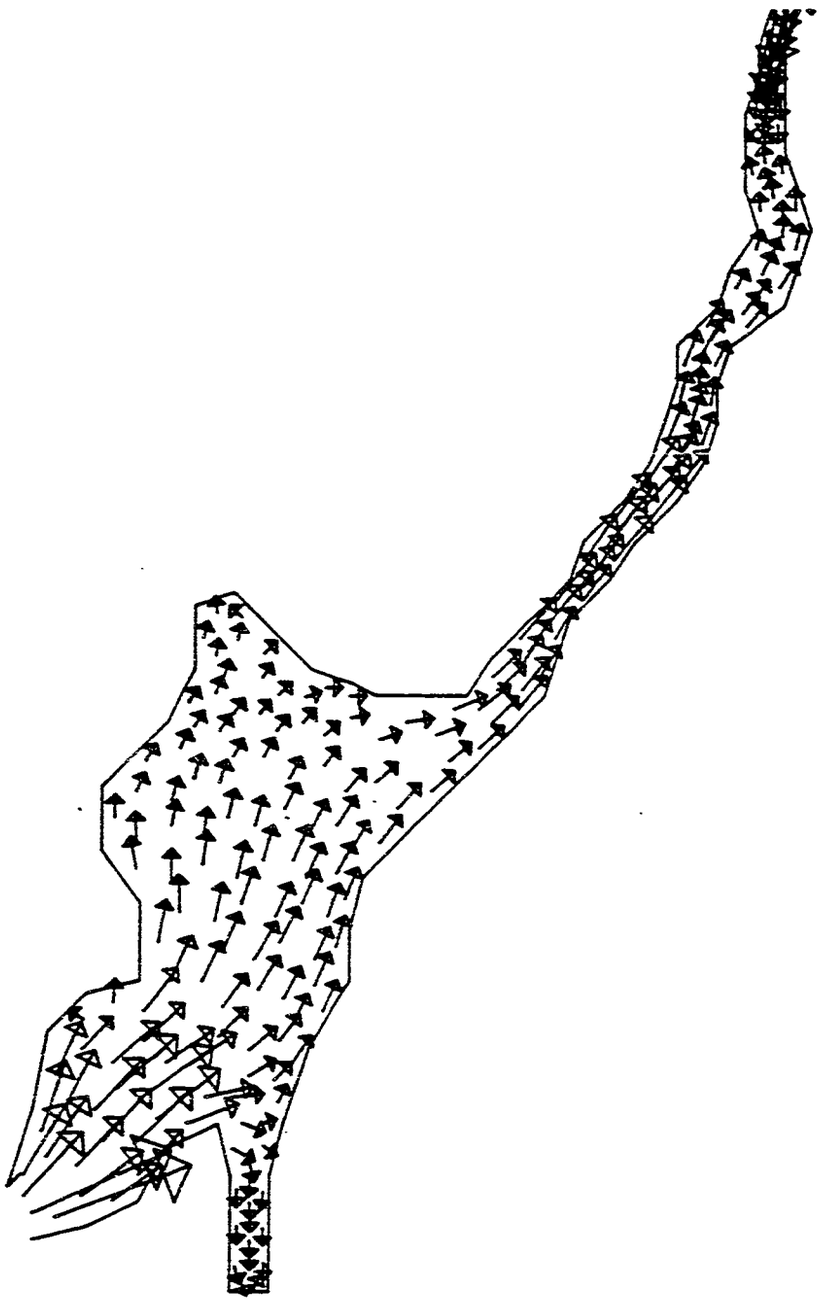

Figure 5.3 Finite element hydrodynamic model predicted maximum flood tidal currents.

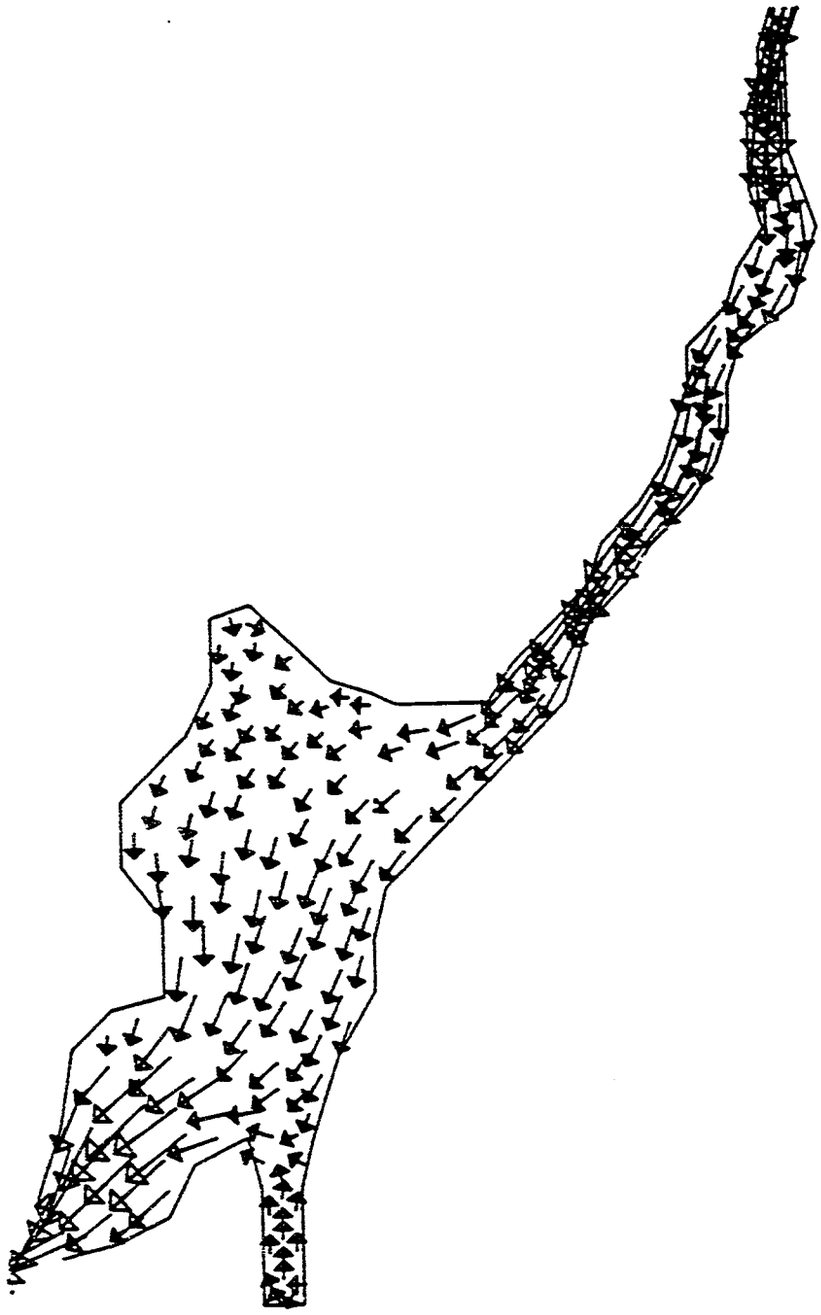

Figure 5.4 Finite element hydrodynamic model predicted tidal current roses.

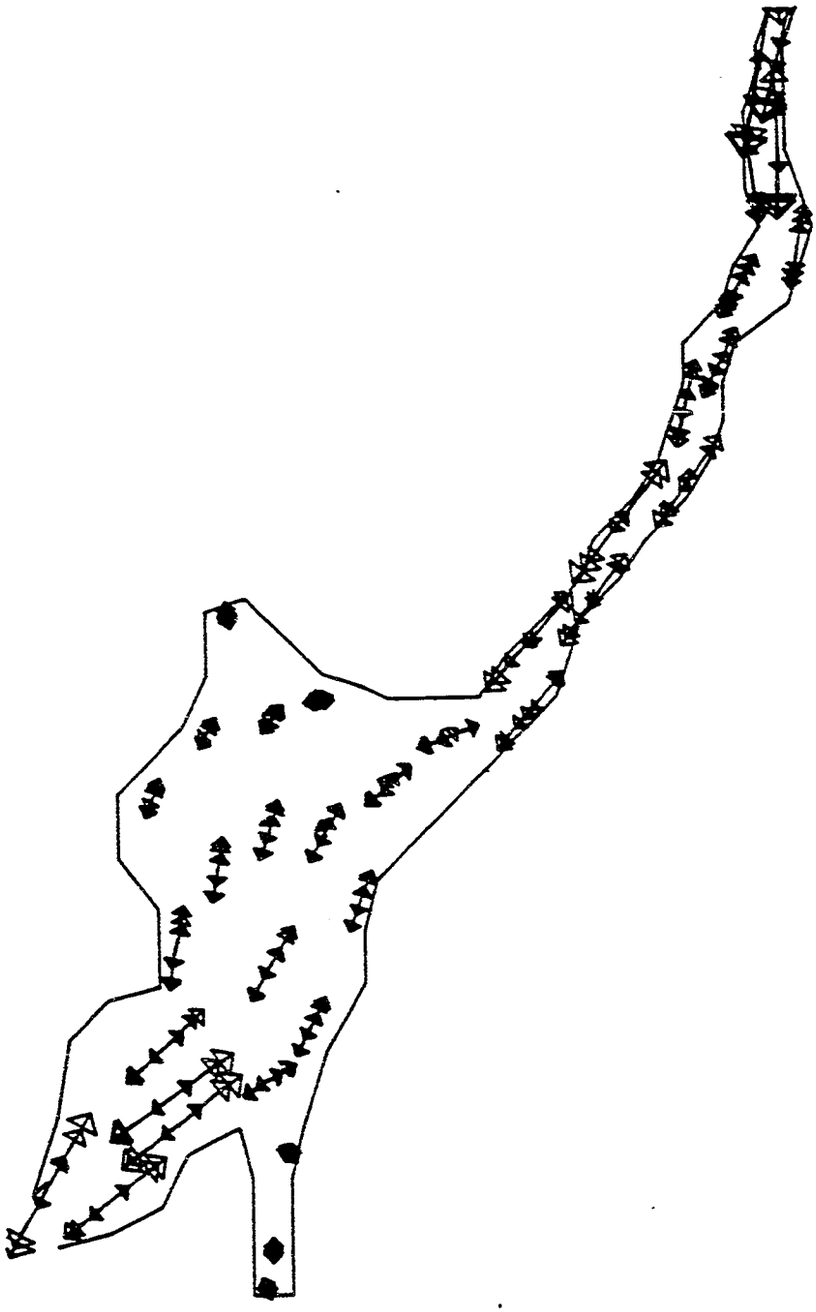

Figure 5.5 Finite element hydrodynamic model predicted tidal current roses.

controlled by a combination of the local bathymetry and the larger scale topography. The magnitude of the currents is as described earlier.

A time series of the surface elevation and tidal currents is presented for the measurement station at Mt. Hope Bridge in Figure 5.6. A similar graph is presented for the Brightman Street Bridge transect in Figure 5.7. The first 3 to 6 hours of the time series are contaminated by model initialization errors and therefore should be ignored. Even though the model was driven with an M_2 tide generation of its harmonic (M_4), while not evident at the Mt. Hope station (Figure 5.6), are clearly seen at the Brightman station (Figure 5.7). This is most clearly illustrated by the double peaked flood currents. For both stations the tidal currents lead the surface elevation by 3.1 hours. This shows, as expected, that the tide exhibits a standing wave behavior in the area (Officer, 1976).

When the M_4 tidal component is included in the forcing at the boundary (5.9 cm, 109.3°), the currents clearly illustrate (Figure 5.8 and 5.9) the presence of the M_4 tidal constituent resulting in a double peaked flood, but a single peaked ebb. The effect is much more pronounced at the Brightman Bridge transect due to nonlinearities (frictional dissipation and the convective acceleration terms) in the governing equations.

The magnitude of the tidal flow through the Brightman transect is 600 m^3/s compared to 3500 m^3/s through the Mt. Hope Bridge transect. The annual average mean discharge for the Taunton River is approximately 18 m^3/s. The tidal flow is a factor of 33 and 194 higher at Brightman and Mt. Hope Bridges, respectively, than the river flow.

A sensitivity study showed that model predictions are relatively insensitive to the magnitude of the bottom friction coefficient. The

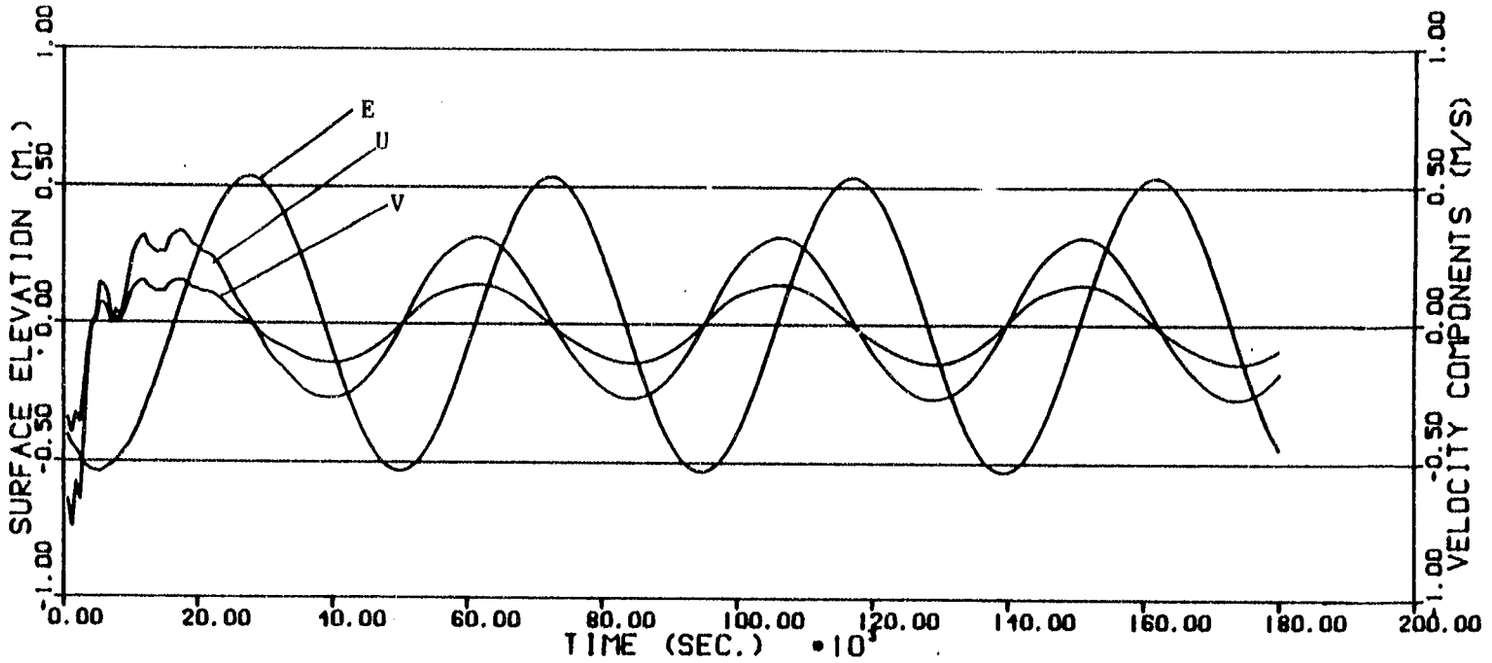

Figure 5.6 Time series of finite element model predicted (M_2) sea surface elevation (cm) and velocities (cm/s) (U-north, V-east) at the Mt. Hope Bridge measurement station.

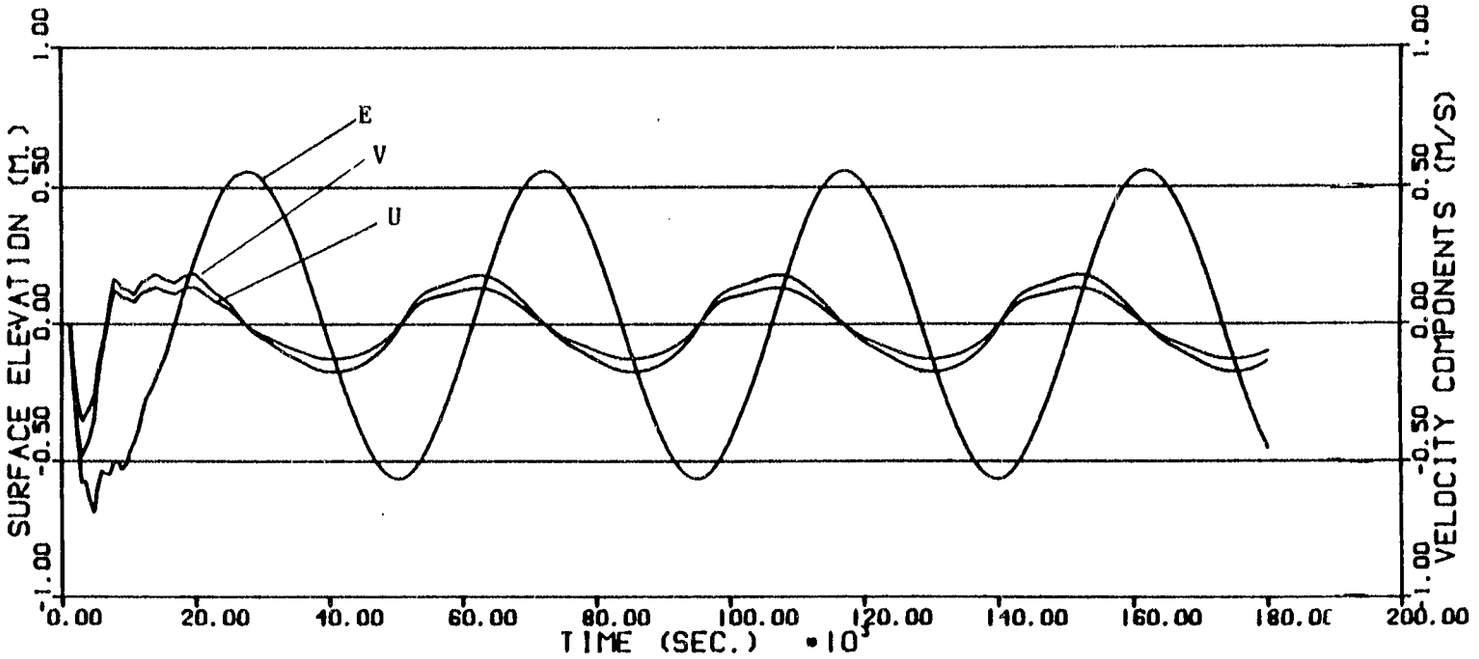

Figure 5.7 Time series of finite element model predicted (M_2) sea surface elevation (cm) and velocities (cm/s) (U-north, V-east) at the Brightman Street measurement station.

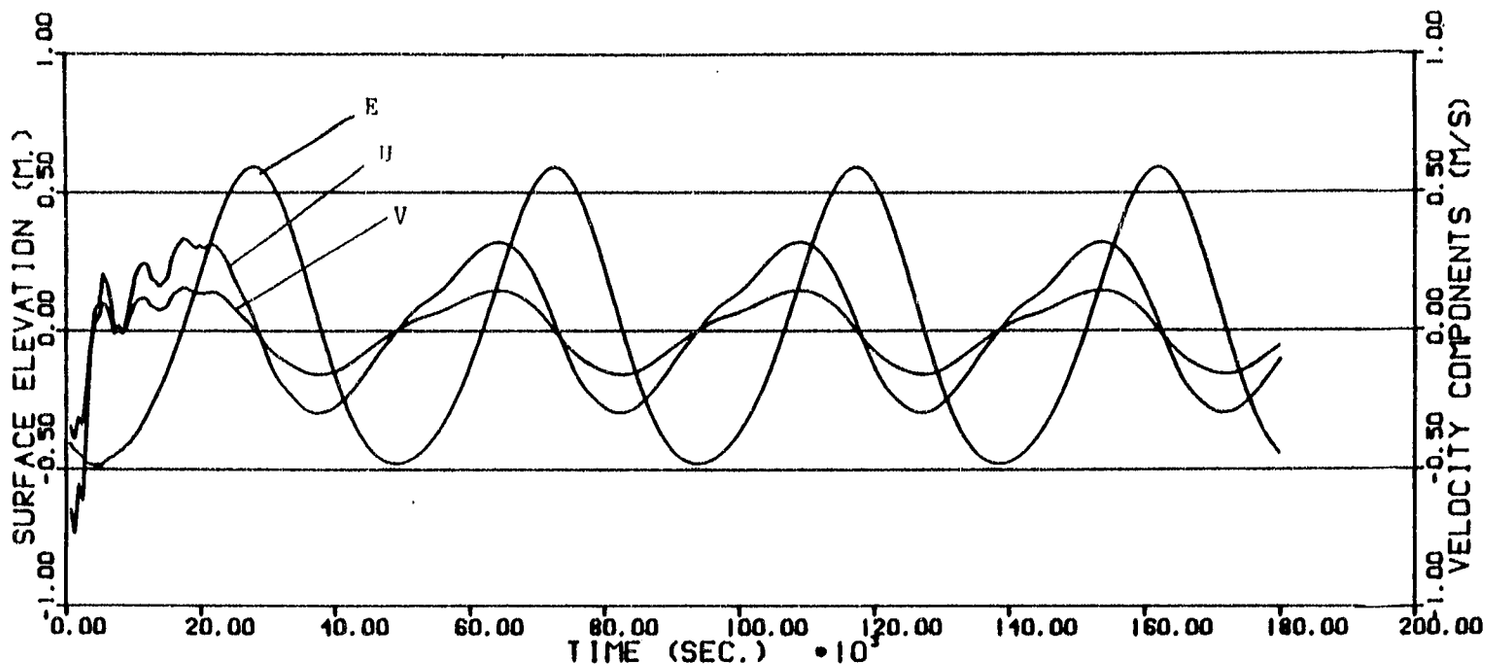

Figure 5.8 Time series of finite element model predicted (M_2 and M_4) sea surface elevation (cm) and velocities (cm/s) (U-north, V-east) at the Mt. Hope Bridge measurement station.

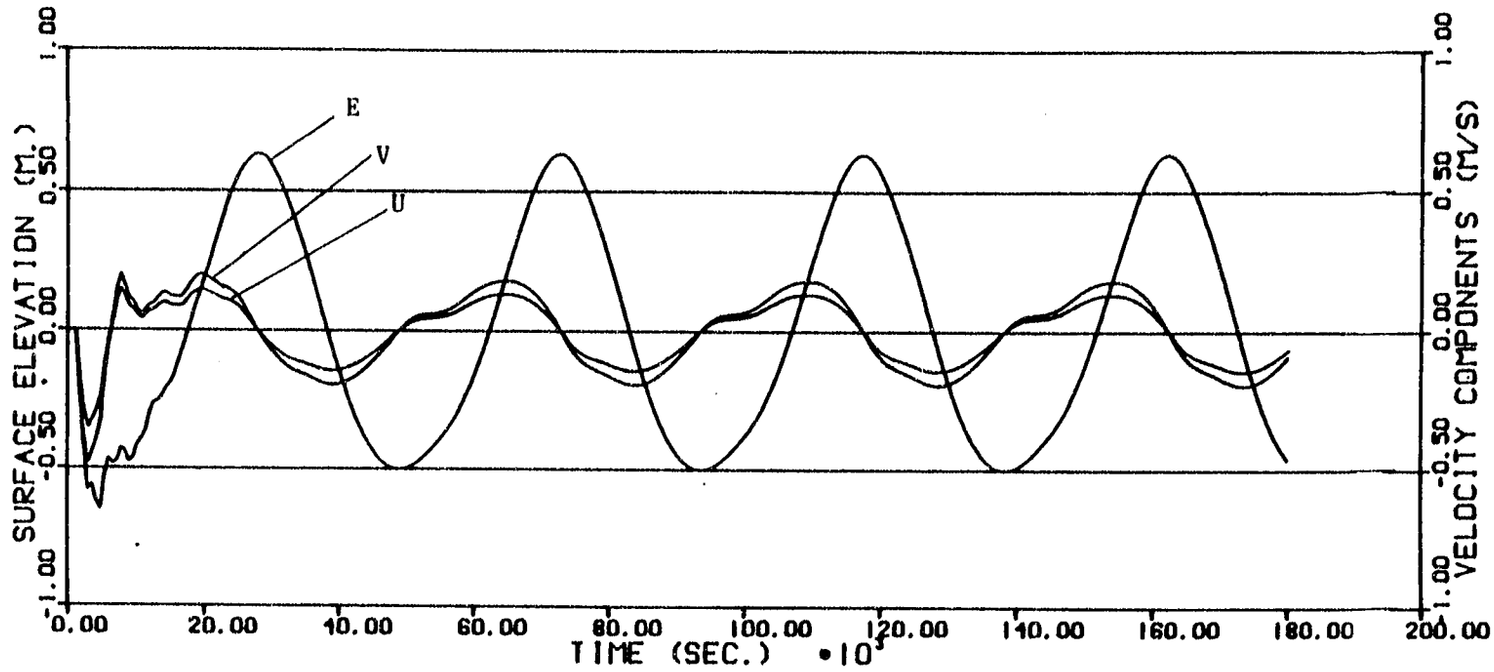

Figure 5.9 Time series of finite element model predicted (M_2 and M_4) sea surface elevation (cm) and velocities (cm/s) (U-north, V-east) at the Brightman Street measurement station.

result was expected because of the standing wave nature of the area (Gordon, 1982; Officer, 1976). The role of the open boundary at the Sakonnet River transect in forcing the tidal circulation in Mt. Hope Bay was also of interest. To evaluate its influence a simulation was run where the Sakonnet River transect was treated as a closed boundary. Comparison of the cases, with this boundary open and closed, showed little difference except in the immediate vicinity of the boundary. One can conclude that tidal flow through this boundary has minimal impact on the tidal circulation in Mt. Hope Bay proper. However, as noted in Section 5.3.2, the impact on the river flow distribution is substantial.

The time of high water throughout the system varies very little. Assuming high tide at the Mt. Hope Bridge transect is at 0 minutes high tide occurs 4 and 8 minutes later at Sakonnet River entrance and Brightman Street Bridge, respectively.

5.4 Application of Boundary Fitted Coordinate Hydrodynamic Model to Study Area

The boundary fitted coordinate hydrodynamic model was applied to the Mt. Hope Bay area of Narragansett Bay using the same study domain, boundary conditions, and bathymetry as the finite element model.

The study was approximated by the boundary fitted coordinate grid system shown in Figure 5.10. Figure 5.10a shows the mesh system generated by the coordinate generation program. The hydrodynamic grid system is shown in Figure 5.10b and has half the grids as Figure 5.10a. The finest resolution is employed in the Taunton River. The same number of grid points are used to describe the lateral variability in Mt. Hope Bay proper

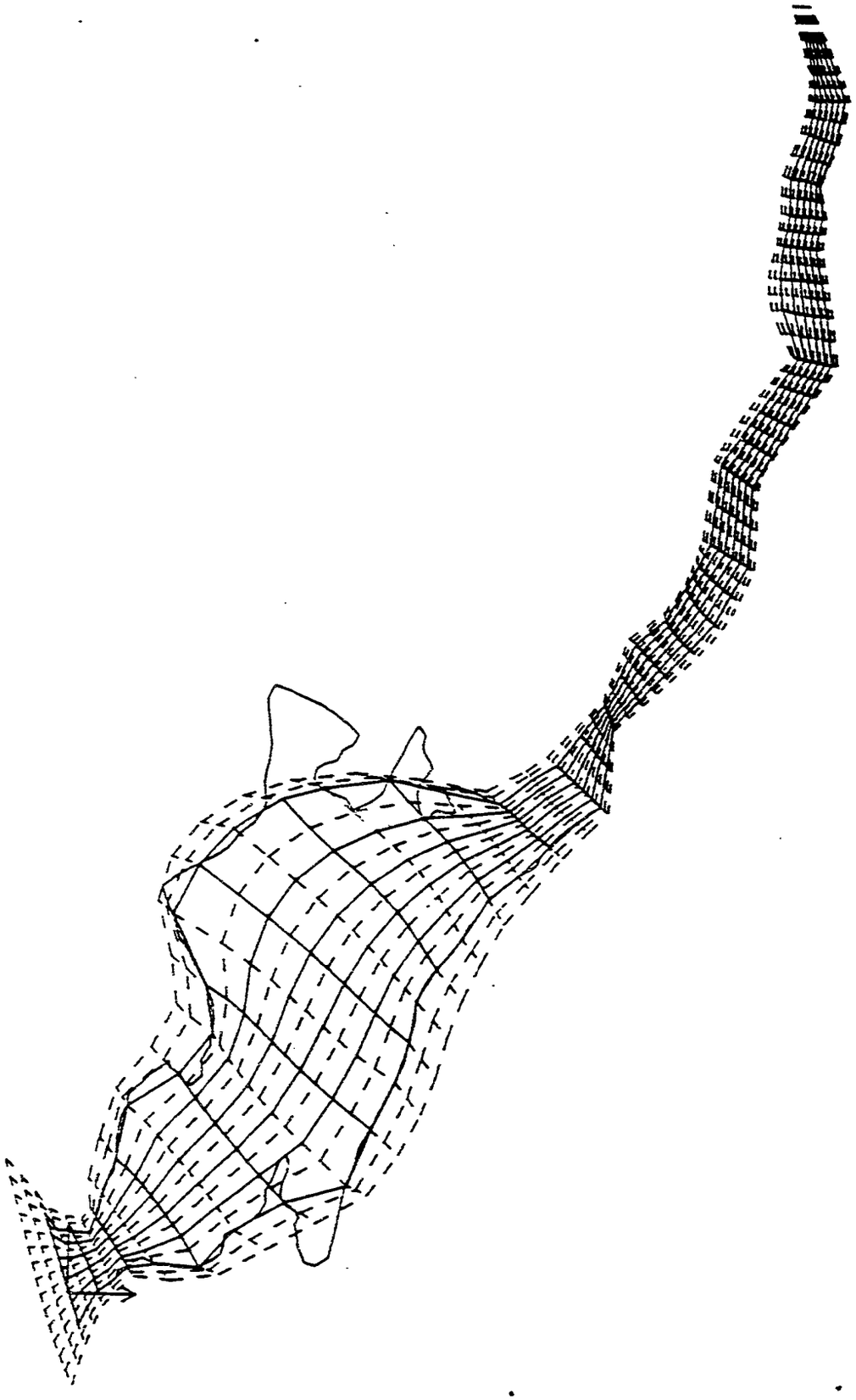

Figure 5.10 Boundary fitted coordinate system used to describe the study area (a) coordination generation program output.

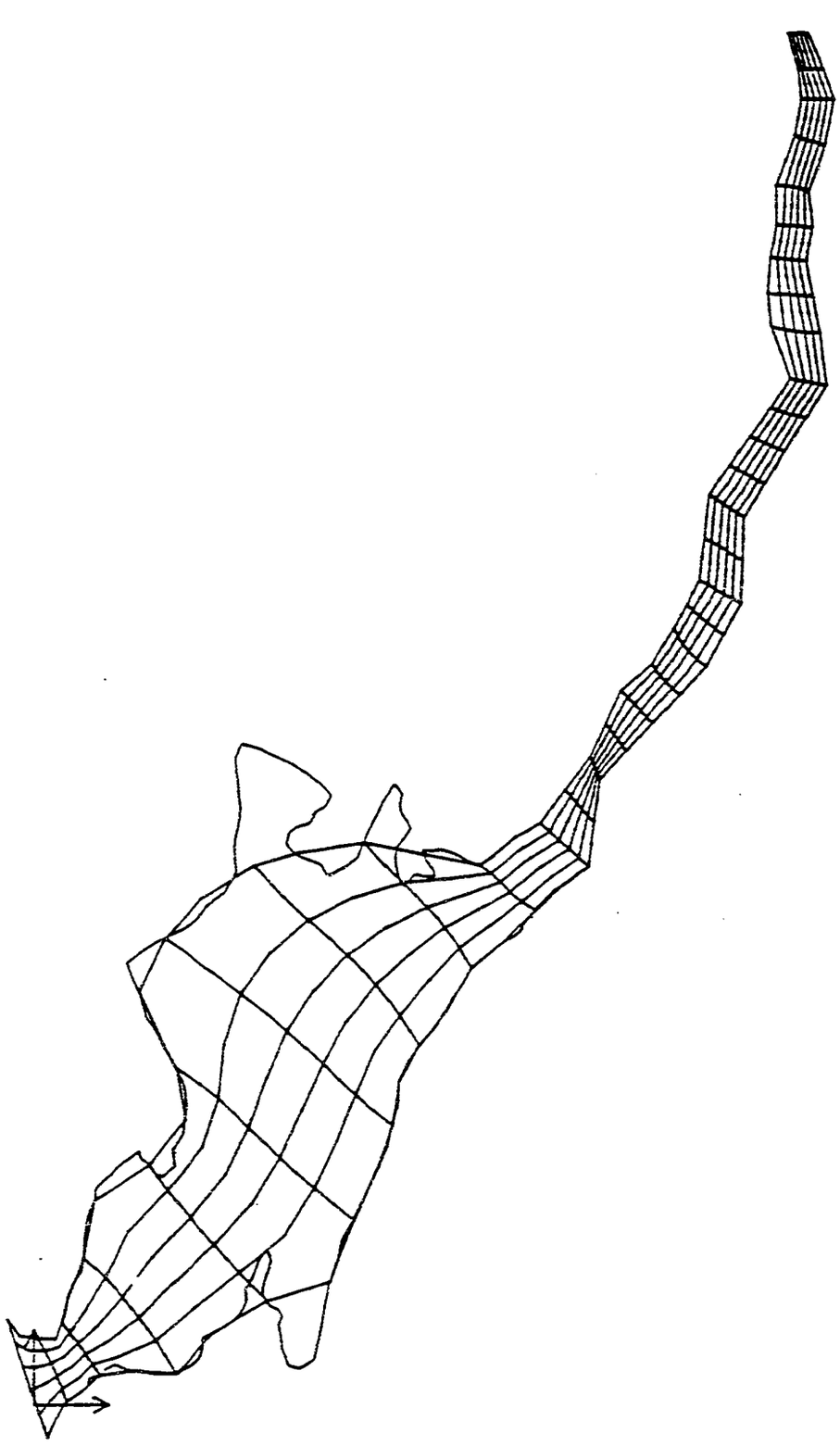

Figure 5.10 Boundary fitted coordinate system used to describe the study area (b) hydrodynamic model grid.

as in the lower Taunton River. The boundary fitted coordinate mesh transforms into a rectangular, square grid system. The study area is a simple rectangle and hence the boundary conditions are particularly straightforward since there are no interior or exterior corners.

5.4.1 Free Oscillation Experiment

To determine the natural frequency of Mt. Hope Bay and the lower Taunton River, a simple free oscillation experiment was performed. The simulation employed the same approach as used in the previously described finite element model simulation. The primary response was observed at a period of 3.5 hours. This is a good agreement with the finite element result.

5.4.2 Tidal Simulations

The M_2 tide (period 12.42 hours) dominates the variability in the observed currents. A simulation of the M_2 tide was performed to determine the tidal currents in the area. Tidal amplitudes and phases on the Mt. Hope Bay open boundary were specified as in the finite element model. Since the finite element model simulations showed that predicted currents were not affected by the Sakonnet River boundary, it was assumed closed in the present simulation. The Manning friction factor was constant at 0.03 throughout the study area.

Figures 5.11 and 5.12 show the model predicted currents for maximum flood and maximum ebb conditions, respectively. The current pattern as shown earlier is primarily determined by the variable geometry and secondarily by the deep water channel proceeding from Mt. Hope Bridge to

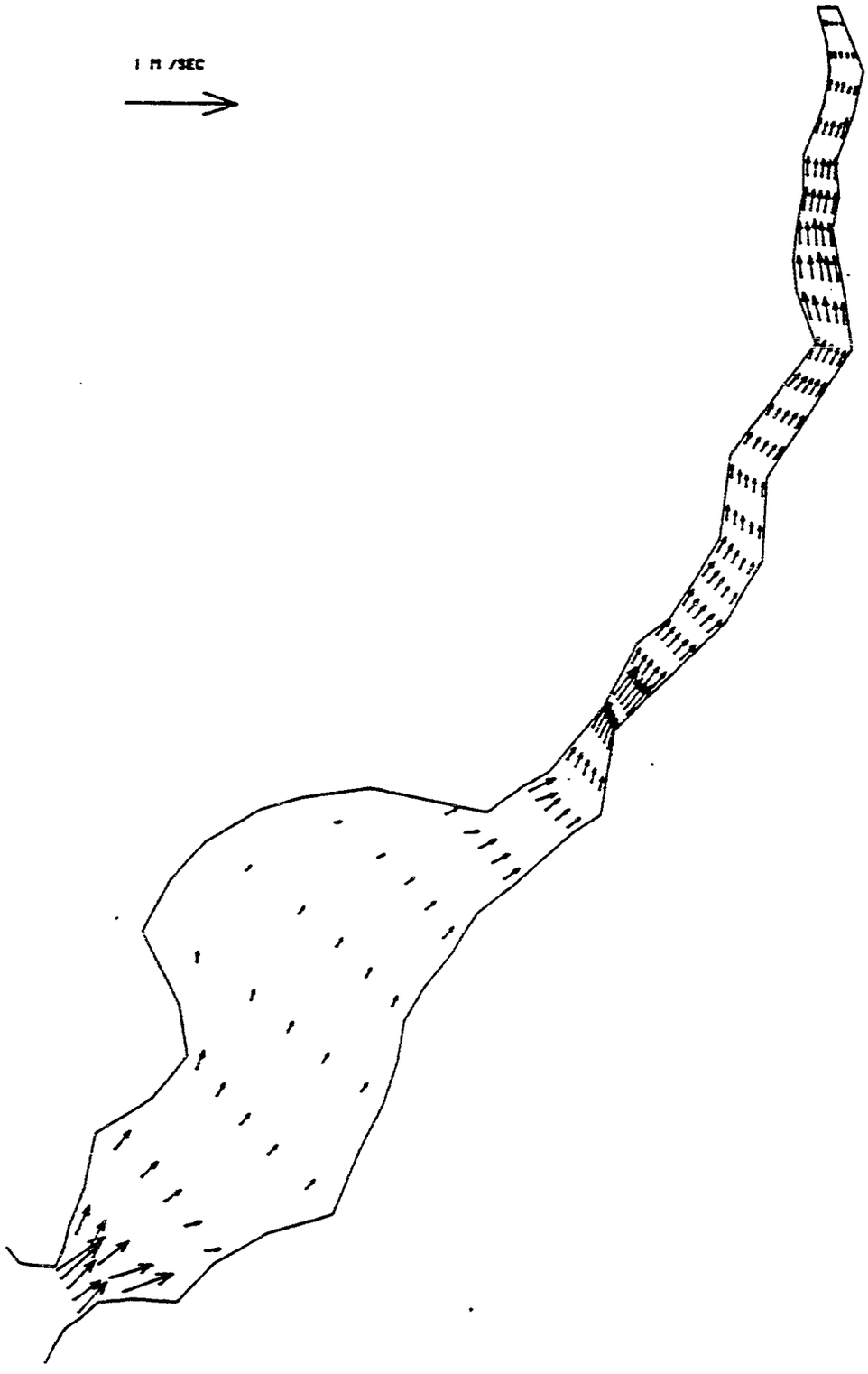

Figure 5.11 Boundary fitted coordinate hydrodynamic model predicted maximum flood tidal currents.

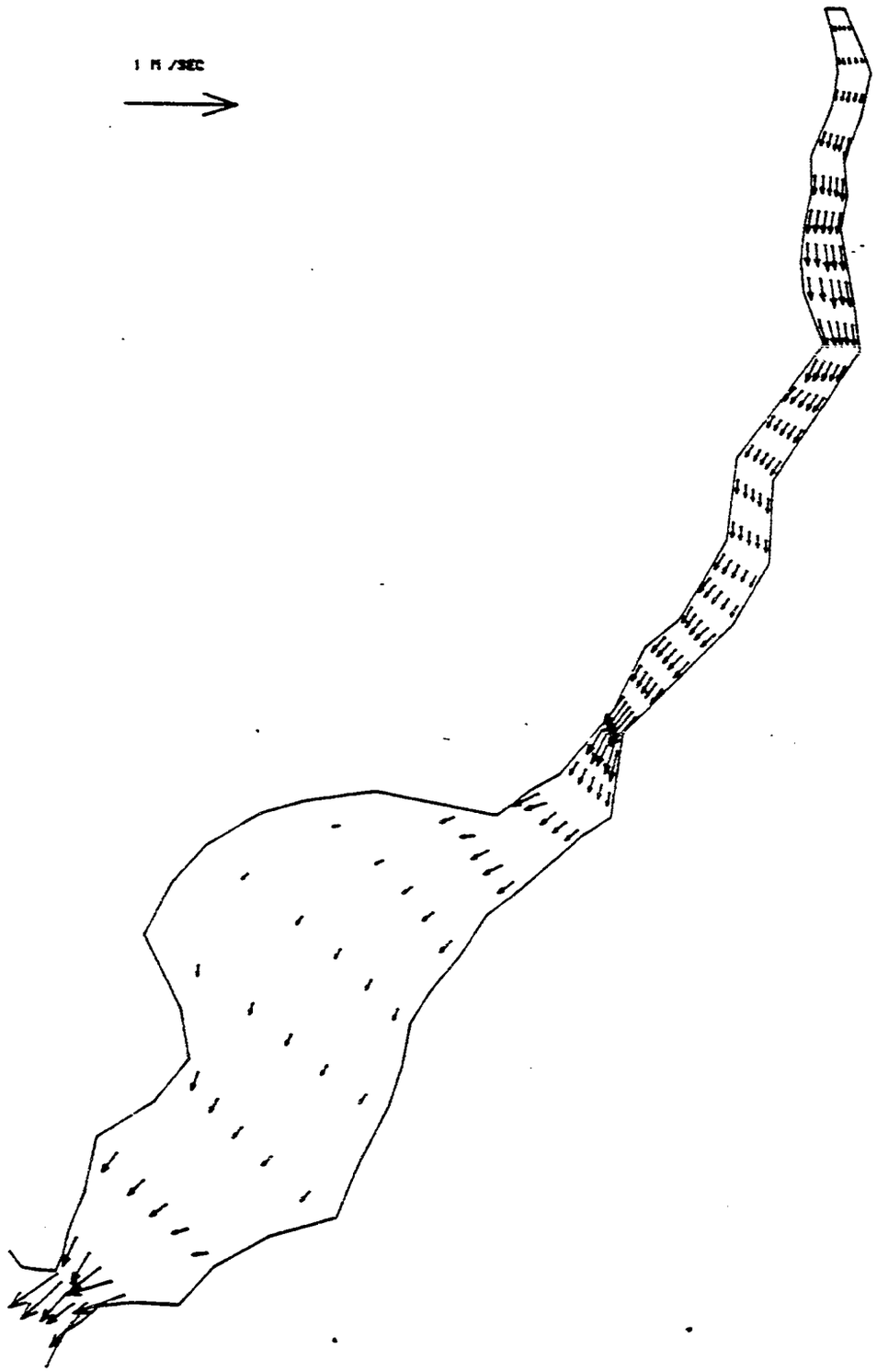

Figure 5.12 Boundary fitted coordinate hydrodynamic model predicted maximum ebb tidal currents.

the lower Taunton River (in the vicinity of Fall River). The currents along this axis are slightly stronger than in the shallower water to the northwest. The maximum currents that occur in a narrow section of the lower Taunton River near the Brightman Street Bridge reach values of 32.8 cm/s. The entrance to Mt. Hope Bay under the bridge has the highest currents with maximum speeds of 30-40 cm/s depending on the exact location.

Figure 5.13 shows the tidal currents roses. For the majority of the area the tidal currents are rectilinear (flood and ebb currents are opposite in direction). Only in areas of low currents is there any circulation or elliptic patterns to the rose and even there the deviations from the rectilinear behavior are minor. The magnitude of the currents is as described earlier.

A time series of the surface elevation and tidal currents for M_2 forcing is presented for the transects at Mt. Hope Bridge in Figure 5.14. A similar graph is presented for the Brightman Street Bridge transect in Figure 5.15. For both stations the tidal currents lead the surface elevation by 3.1 hours. This shows, as expected, that the tide exhibits a standing wave behavior in the area (Officer, 1976).

The currents barely show the presence of the M_4 tidal constituent resulting in a double peaked flood, but a single peak ebb. The effect is much more pronounced at the Brightman St. Bridge transect due to nonlinearities in the governing equations. Inclusion of M_4 in the forcing at the open boundary however shows this behavior quite clearly. This is shown in Figure 5.16 for Mt. Hope Bridge and Figure 5.17 for Brightman St. Bridge.

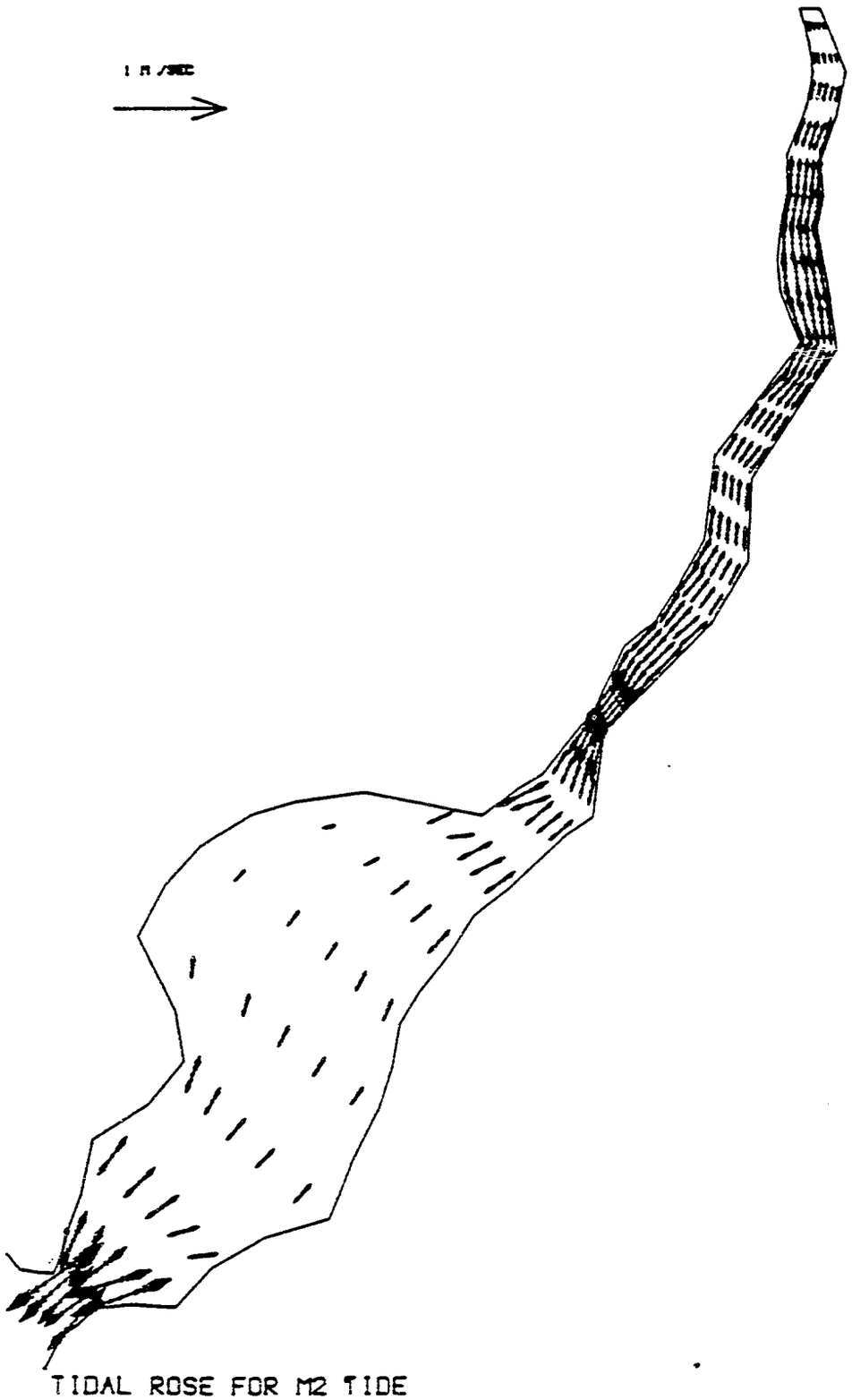

Figure 5.13 Boundary fitted coordinate hydrodynamic model predicted tidal current roses.

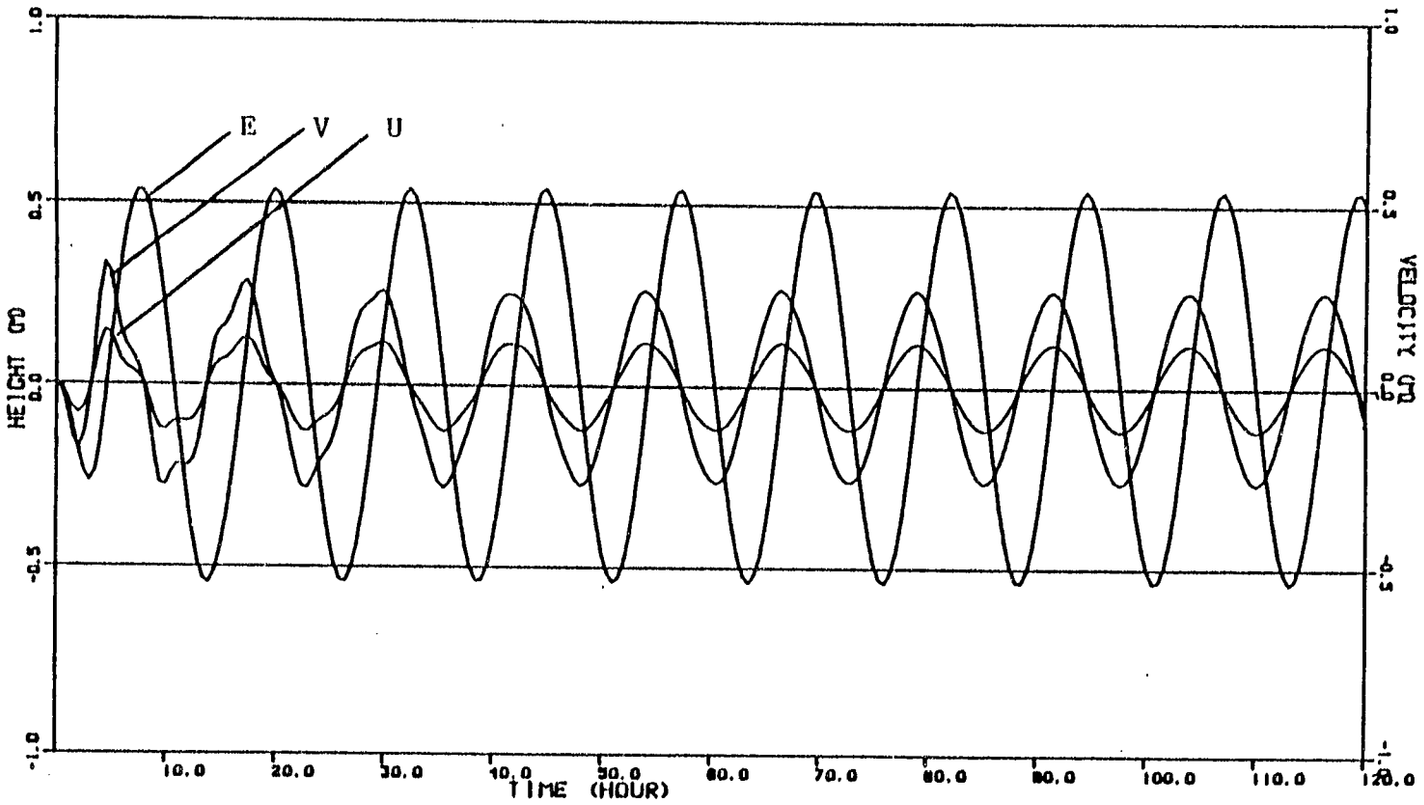

Figure 5.14 Time series of boundary fitted coordinate hydrodynamic model predicted (M_2) sea surface elevation (cm) and velocities (cm/s) (U-east, V-north) at the Mt. Hope Bridge measurement station.

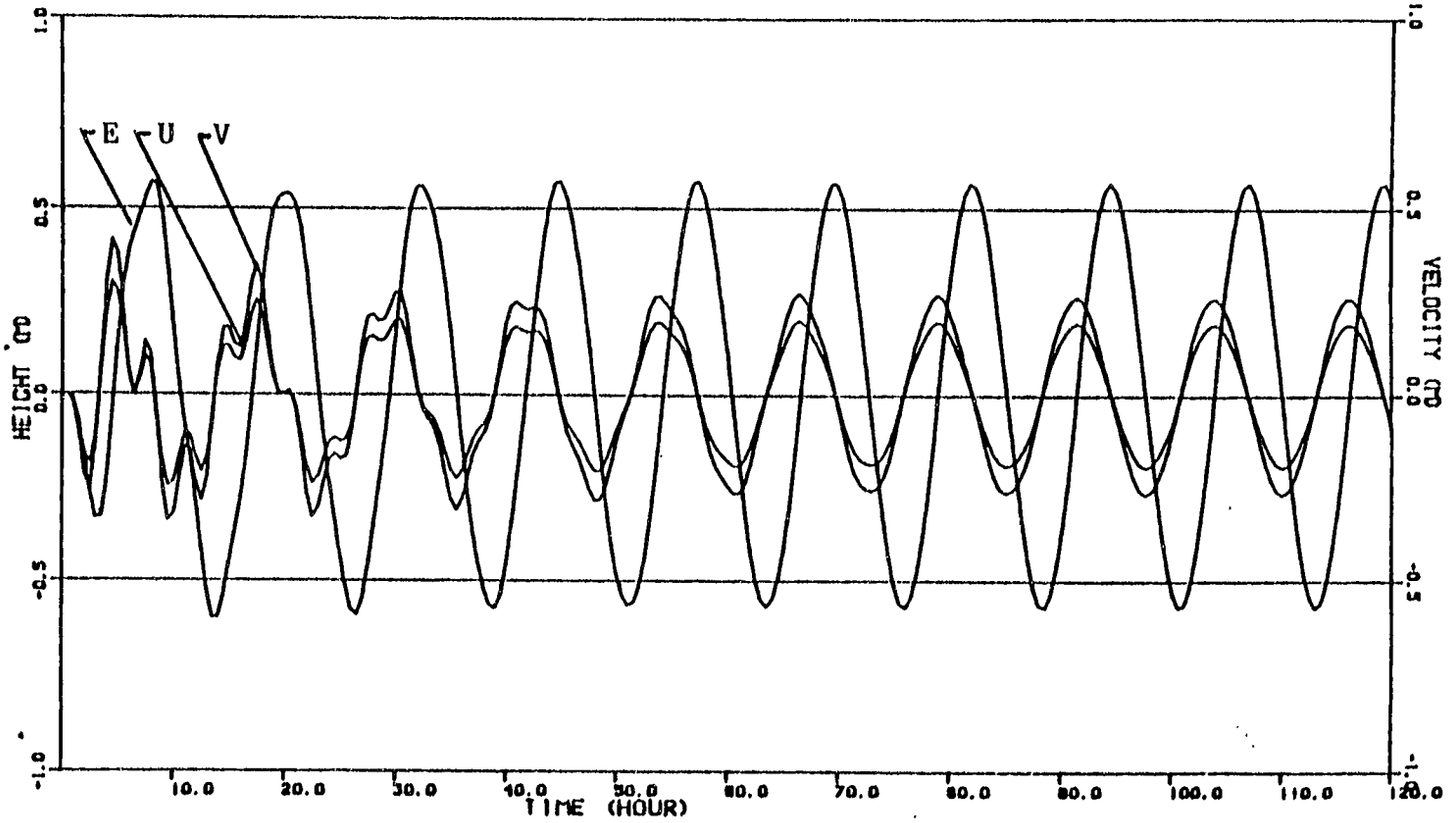

Figure 5.15 Time series of boundary fitted coordinate hydrodynamic model predicted (M_2) sea surface elevation (cm) and velocities (cm/s) (U-east, V-north) at the Brightman Street measurement station.

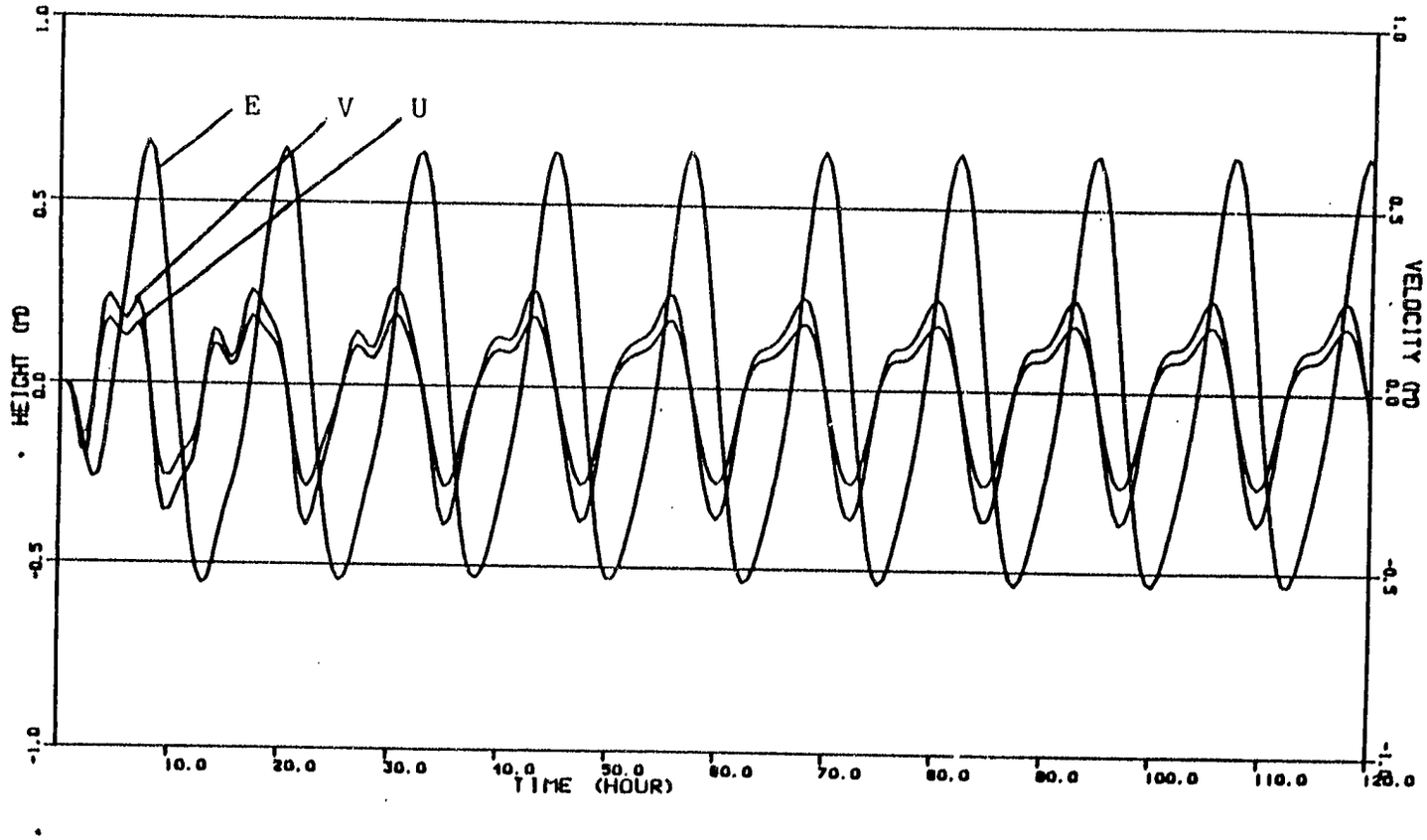

Figure 5.16 Time series of boundary fitted coordinate hydrodynamic model predicted (M_2 and M_4) sea surface elevation (cm) and velocities (cm/s) (U-east, V-north) at the Mt. Hope Bridge measurement station.

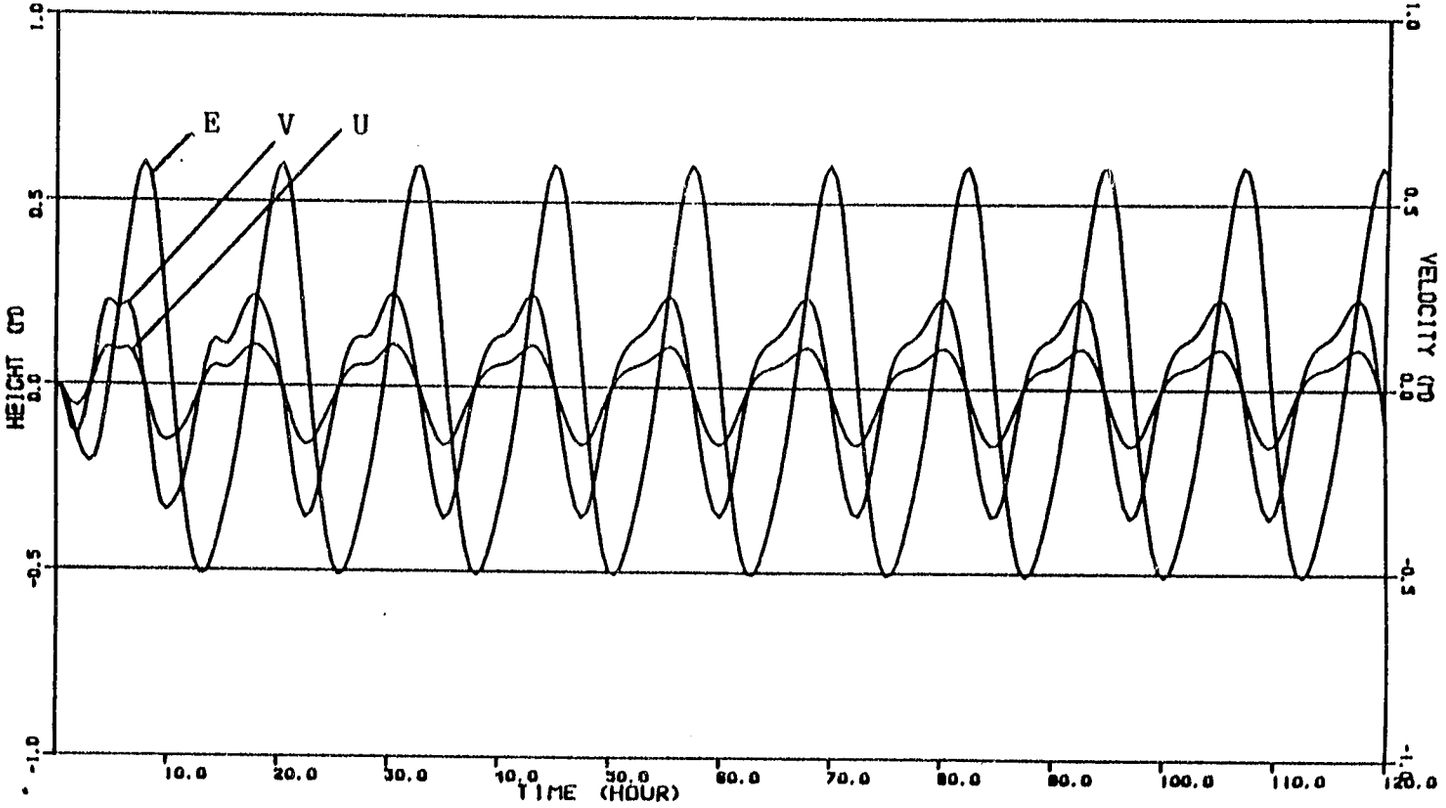

Figure 5.17 Time series of boundary fitted coordinate hydrodynamic model predicted (M_2 and M_4) sea surface elevation (cm) and velocities (cm/s) (U-east, V-north) at the Brightman Street measurement station.

6. CONCLUSIONS

Based on the analysis of the field data and modeling investigations the following conclusions evolve.

1. Both field data and the hydrodynamic models show that the sea surface elevation and currents in the area are dominated by the M_2 tide in approximately a standing wave pattern, with tidal currents leading surface elevation by approximately 90° or 3 hours. The M_2 currents typically account for 80-90% of the current variance and 90% of the surface elevation variance. The M_4 tidal components while relatively small are important and generate a double peaked flood, single peaked ebb similar to that observed in Narragansett Bay proper. The M_4 tide is also observed to increase in magnitude to the M_2 as one moves from Mt. Hope Bridge to the lower Taunton River.
2. Tidal currents (M_2) are generally weak in the Sakonnet River (4.6 cm/s) (on the Mt. Hope Bay side of the bridges) and stronger under Mt. Hope Bridge (20.3 cm/s) and near the Brightman Street Bridge (22.6 cm/s). Model predictions show that the tidal currents are slightly stronger in the dredged channel system from Mt. Hope Bay Bridge to the Taunton River than in the shallower areas to the northwest. Typical maximum mid-bay model predicted values are 10 cm/s.
3. The tidal range (1.14 m) shows no amplification from the Mt. Hope Bridge to Steep Brook (lower Taunton River) stations. The high water phase difference predicted by the hydrodynamic model is typically on the order of 5 minutes between the two stations. This estimate has been impossible to verify with the limited sea surface elevation

observations. To a first order the sea surface is seen to respond uniformly throughout Mt. Hope Bay. This observation is consistent with the standing wave nature of the system.

4. Low frequency currents (30 hour filtered) show little wind induced forcing and are dominated by relatively steady flows. For the Brightman Street Bridge station a classical stratified, but topographically controlled, estuarine pattern is displayed with flow up river at the bottom and down river at the surface. For the Sakonnet River and Mt. Hope Bridge measurement sites the flow is consistently out of Mt. Hope Bay. More detailed measurements at the Mt. Hope Bridge transect in deployment 5 show consistent outflow of 4.4 to 13.7 cm/s at all four measurement stations. Using the transect observed mean velocities/direction and the associated cross sectional areas, for the three boundary stations (Brightman Street Bridge, Mt. Hope Bridge, and Sakonnet River Bridge) we predict a strong net outflow from Mt. Hope Bay; about two orders of magnitude larger than the river flow. Strong lateral variations in the Mt. Hope Bridge currents are a potential cause of this imbalance in net flows through the system.

5. The hydrography of the area shows that throughout Mt. Hope Bay the water column is well mixed. As one approaches the lower end of the Taunto River the fresh water river plume is clearly observed and the water column becomes stratified. Two layer net estuarine flow is observed in the area. Use of simple analytic models for density induced flows give estimates that are qualitatively consistent with observations but predicted values are a factor of two or more larger than measurements. The differences appear to be attributable to the

variable topography and bathymetry of the area that is not represented in the simple uniform channel models.

6. Model simulations show that the Taunton River freshwater flow exits Mt. Hope Bay through the Mt. Hope Bridge and Sakonnet River transects with a distribution of 68% and 32%, respectively. These values are in excellent agreement with earlier estimates by Hicks (1959) that show a 70%/30% split.

7. Hydrodynamic model simulations show that the tidal response of the area is dominated by the flow through the Mt. Hope Bridge transect. Simulations with the Sakonnet River transect closed show little variations in currents or surface elevations in the bay proper. Accurate tidal predictions however require careful representation of the lower reach of the Taunton River and Mt. Hope Bay proper.

8. The finite element and boundary fitted coordinate tidal hydrodynamic model simulations show results consistent with standing wave dynamics. Model predictions depend most strongly on topographic and bathymetric representation of the study area.

9. This is the first time the boundary fitted coordinate model has been applied to an actual estuarine system and compared with observations. The results of this preliminary analysis are quite encouraging and have illustrated the ability of this modeling approach to represent complex geometry typical of a small estuarine system.

ACKNOWLEDGEMENTS

This two-year study was jointly funded by the University of Rhode Island Sea Grant program and the EPA-sponsored Narragansett Bay Project.

Mr. Larry Simoneau, Ocean Engineering, provided considerable support in keeping the oceanographic instrumentation functioning and was extremely helpful in solving numerous data reading and processing problems. The computational resources necessary for data processing and analysis and numerical modeling were provided by the University of Rhode Island (URI) Academic Computer Center (ACC). Dr. David Shonting of the Naval Underwater Systems Center (NUSC), Newport, Rhode Island kindly allowed us to use his Endeco current meter reader on numerous occasions. Data for meteorological conditions was provided to us on a monthly basis by the NOAA, U.S. Weather Service office at Green Airport, Warwick, Rhode Island. Flow data for the Taunton River was provided courtesy of Mr. Herb Johnston, United States Geological Survey (USGS), Providence office. The USGS Boston office provided us with the cross-sectional areas and depths for the Taunton River system.

REFERENCES

Alden Research Laboratories, ARL, 1970. Model Study Brayton Point Station, Somerset, Massachusetts for New England Power Company, Alden Research Laboratories, Worchester Polytechnic Institute.

Arkawa, A. and V.R. Lamb, 1977. Computational Design of the Basic Dynamical Process of the UCLA General Circulation Model. Methods in Computational Physics, Vol. 17, Academic Press, 173-265.

Blumberg, A. and H.J. Herring, 1982. A vertically integrated circulation model using curvilinear coordinates, Preliminary Report U.S. Department of Interior, Contract AA851-CT1-61, 17 pp.

Carrier, R., W. Brown, and J. Irish, 1982. TIHARC User's Guide, unpublished manuscript, University of New Hampshire.

Chinman, R.A. and S.W. Nixon, 1985. Depth-Area-Volume Relationships in Narragansett Bay, NOAA/Sea Grant Marine Technical Report 87, University of Rhode Island.

Dennis, R.E., and E.E. Long, 1971. A User's Guide to a Computer Program for Harmonic Analysis of Data at Tidal Frequencies, NOAA Technical Report, NOS 41, U.S. Dept. of Commerce, NOAA, National Ocean Survey, Rockville, Maryland.

Dunn, C.Q., L.Z. Hale and A. Bucci, 1979. The Bay Bib: Rhode Island Marine Bibliography, Revised Edition, Vols. I and II. University of Rhode Island Mar. Tech, Reports, Nos. 70 and 71.

Dyer, K.R., 1973. Estuaries: A Physical Introduction, John Wiley & Sons, New York.

Environmental Devices Corporation (ENDECO), 1979. ENDECO Type 2501 Data Translator Operation Manual, Marion, Massachusetts.

EPA, 1971. Report on Pollution of the Interstate Waters of Mt. Hope Bay and its Tributary Basins. Environmental Protection Agency, Washington, D.C. 70 pp plus Append.

Gordon, R.B., 1982. Wind Driven Circulation in Narragansett Bay, Ph.D. Dissertation, Department of Ocean Engineering, University of Rhode Island, Kingston, Rhode Island.

Grotkop, G. 1973. Finite element analysis of long period water waves, Comput. Methods Appl. Mech. Eng.. 2, 147-157.

Haight, F.J., 1936. Currents in Narragansett Bay, Buzzards Bay and Nantucket and Vineyard Sounds, Special Pub. No. 208, Washington,: U.S. Dept. of Commerce, Coast and Geodetic Survey.

Hansen, D.V. and M. Rattray, 1965. Gravitational Circulation in Straits and Estuaries, J. Marine Research, 23, 104-122.

Hess, K.W., 1974. A Three-Dimensional Model of Steady Gravitational Circulation and Salinity Distribution in Narragansett Bay, Ph.D. Dissertation, Department of Ocean Engineering, University of Rhode Island, Kingston, Rhode Island.

Hess, K.W., 1976. A three-dimensional numerical model of the estuary circulation and salinity in Narragansett Bay, Estuarine and Coastal Marine Science 4: 325:338.

Hess, K.W. and F.M. White, 1974. A Numerical Tidal Model of Narragansett Bay, Ocean Engineering, University of Rhode Island, Marine Technical Report No. 20. 141 p.

Hicks, S.D., 1959. The Physical Oceanography of Narragansett Bay, Limnology and Oceanography, 4, pp. 316-328.

Isaji, T. and M.L. Spaulding, 1981. Numerical Modeling of Entrainment and Far Field Thermal Dispersion for NEP 1 and 2. Charlestown, Rhode Island, Oak Ridge National Laboratory, ORNL/TM-7590.

Kjerfve, B., 1979. "Measurements and Analysis of Water Current, Temperature, Salinity and Density," in Estuarine Hydrography and Sedimentation, K.R. Dyer (ed.), Cambridge University Press, New York.

Leendertse, J.J., 1967. Aspects of a Computational Model for Long-Period Water-Wave Propagation, Rand Corp., Memorandum RM 5294-PR, Santa Monica, California.

Lynch, D.R. and W.G. Gray, 1978. Analytic Solutions for Computer Flow Model Testing, J. Hydraul. Div., Am. Soc. Civ. Eng., 104: 1409-1428.

Madala, R.V. and S.A. Piacsek, 1977. A Semi-Implicit Numerical Model for Baroclinic Oceans, J. of Comp. Physics, 23: 167-178.

McDowell, D.M. and B.A. O'Connor, 1977. Hydraulic Behavior of Estuaries, John Wiley & Sons, New York.

Officer, C.B., 1976. Physical Oceanography of Estuaries (and Associated Coastal Waters), New York: Wiley.

Pilson, M.E.Q., 1985. On the Residence Time of Water in Narragansett Bay, Estuaries.

Pinder, G.F. and W.G. Gray, 1977. Finite Element Simulation in Surface and Subsurface Hydrology, Academic Press, New York, New York.

Schureman, P., 1941. Manual of Harmonic Analysis and Prediction of Tides, U.S. Coast and Geodetic Survey, Special Report No. 98, U.S. Govt. Printing Office, Washington, D.C.

Spaulding, M.L., 1984. A Vertically Averaged Circulation Model Using Boundary Fitted Coordinates. Journal of Physical Oceanography, Vol. 14, 973-982.

Swanson, J.C., 1987. A Three Dimensional Numerical Model System of Coastal Circulation and Water Quality. Ph.D. Dissertation, Department of Ocean Engineering, University of Rhode Island, Kingston, Rhode Island.

Swanson, J.C. and M.L. Spaulding, 1974. Tides and Tidal Currents of Narragansett Bay, Ocean Engineering, Sea Grant, University of Rhode Island, Marine Technical Report 35.

Swanson, J.C. and M.L. Spaulding, 1984. A Three-Dimensional Semi-Implicit Boundary Fitted Coordinate Hydrodynamic Model: User's Manual, report prepared by Applied Science Associates, Inc., Wakefield, Rhode Island, Report 84-19.

Thames, F.C., 1975. Numerical Solution of the Incompressible Navier-Stokes Equations About Arbitrary Two-Dimensional Bodies, Ph.D. Dissertation, MIssissippi State University.

Thames, F.C., J.F. Thompson, C.W. Mastin and R.L. Waler, 1977. Numerical Solutions of Viscous and Potential Flow About Arbitrary Two-Dimensional Bodies Using Body-Fitted Coordinate Systems. J. Comput. Phys. 24, 245-273.

Thompson, J.F., F.C. Thames, and C.W. Mastin, 1974. Automatic Numerical Generation of Body-Fitted Curvilinear Coordinate Systems for Fields Containing Any Number of Arbitrary Two-Dimensional Bodies. J. Comput. Phys. 15, 299-317.

Thompson, J.F., F.C. Thames, S.P. Shanks, R.N. Reddy, and C.W. Mastin, 1976. Solutions of the Navier-Stokes Equations in VArious Flow Regimes on Field Containing any Number of Arbitrary Bodies Using Boundary Fitted Coordinate Systems. Proc. Fifth Int. Conf. on Numerical Methods in Fluid Dynamics, Enschede, The Netherlands, Lecture Notes on Physics, Vol. 59, Springer-Verlag, 421-427.

Thompson, J.F., F.C. Thames, and C.W. Mastin, 1977a. TOMCAT-A Code for Numerical Generation of Boundary-Fitted Curvilinear Coordinate Systems on Fields Containing Any Number of Arbitrary Two-Dimensional Bodies, J. Comput. PHys. 24, 274-302.

Thompson, J.F., F.C. Thames, and C.W. Mastin, 1977b. Boundary-Fitted Curvilinear Coordinate System for Solution of Partial Differential Equations of Fields Containing Any Number of Arbitrary Two-Dimensional Bodies. NASA CR-2729.

Turner, A.C., 1984. Tidal and Subtidal Circulation in the Providence River, M.S. Thesis, Department of Ocean Engineering, University of Rhode Island, Kingston, Rhode Island.

Wang, D. and J. Connor, 1975. Mathematical Modeling of Near Coastal Circulation, Report No. MITSG 75-13, MIT, Cambridge, Massachusetts.

Wang, H.P. and F.M. White, 1976. Multi-Level Finite Element Hydrodynamic Model of Block Island Sound, Proceedings Intl. Symposium on Numerical Methods in Water Resources, Princeton University, May.

Weisberg, R.H., 1974. The Non-Tidal Flow in the Providence River of Narragansett Bay: A Stochastic Approach to Estuarine Circulation, J. Phys. Oceanog., 6, pp. 721-734.